LA-10819-T
Thesis

UC-20g and UC-34B
Issued: September 1986

LA--10819-T

DE87 002229

Field Reversing Magnetotail Current Sheets: Earth, Venus, and Comet Giacobini-Zinner

David John McComas

Los Alamos National Laboratory
Los Alamos, New Mexico 87545

Dedicated to my parents,

Harrold James and Hazelyn McComas,

for their unwavering support and encouragement.

TABLE OF CONTENTS

LIST OF FIGURES

LIST OF FIGURES (continued)

VITA

May 22, 1958	Born, Milwaukee, Wisconsin
1980	B.S., Massachusetts Institute of Technology
1980-present	Staff Member, Los Alamos National Laboratory
1983-1984	Fellowship, Institute for Geophysics and Planetary Physics, Los Alamos Branch
1984-1985	Advanced Study Program Award, Los Alamos National Laboratory
1985	M.S., University of California, Los Angeles

PUBLICATIONS

1) Radially Uniform Electron Source; D. McComas and S.J. Bame; Review of Scientific Instruments, 53, 1490, 1982.

2) Electron Heating Within the Earth's Bowshock; W.C. Feldman, S.J. Bame, S.P. Gary, J.T. Gosling, D. McComas, M.F. Thomsen, G. Paschmann, N. Sckopke, M.M. Hoppe, C.T. Russell; Physical Review Letters, 49, 199, 1982.

3) Electron Velocity Distributions Near the Earth's Bowshock; W.C. Feldman, R.C. Anderson, S.J. Bame, S.P. Gary, J.T. Gosling, D.J. McComas, M.F. Thomsen, G. Paschmann, M.M. Hoppe; Journal of Geophysical Research, 88, 96, 1983.

4) ISPM Solar Wind Plasma Experiment; S.J. Bame, J.P. Glore, D.J. McComas, K.R. Moore, J.C. Chavez, T.J. Ellis, G.R. Peterson, J.H. Temple, F.J. Wymer; ESA Special Publication SP-1050, 47, 1983.

5) Plasma Regimes in the Deep Geomagnetic Tail: ISEE-3; S.J. Bame, R.C. Anderson, J.R. Asbridge, D.N. Baker, W.C. Feldman, J.T. Gosling, E.W. Hones, Jr., D.J. McComas, R.D. Zwickl; Geophysical Research Letters, 10, 912, 1983.

6) Channel Multiplier Compatible Materials and Lifetime Tests; D.J. McComas and S.J. Bame; Review of Scientific Instruments, 55, 463, 1984.

7) Structure of the Magnetotail at 220R_E and Its Response to Geomagnetic Activity; E.W. Hones, Jr., D.N. Baker, S.J. Bame, W.C. Feldman, J.T. Gosling, D.J. McComas, R.D. Zwickl, J.A. Slavin, E.J. Smith, B.T. Tsurutani; Geophysical Research Letters, 11, 5, 1984.

8) Correlated Dynamical Changes in the Near Earth and Distant Magnetotail Regions: ISEE-3; D.N. Baker, S.J. Bame, W.C. Feldman, J.T. Gosling, P.R. Higbie, E.W. Hones, Jr., D.J. McComas, R.D. Zwickl; Journal of Geophysical Research, 89, 3855, 1984.

9) Evolution of the Earth's Distant Magnetotail: ISEE-3 Electron Plasma Results; R.D. Zwickl, D.N. Baker, S.J. Bame, W.C. Feldman, J.T. Gosling, E.W. Hones, Jr., D.J. McComas, B.T. Tsurutani, J.A. Slavin; Journal of Geophysical Research, 89, 11007, 1984.

10) Evidence for Slow-Mode Shocks in the Deep Geomagnetic Tail; W.C. Feldman, S.J. Schwartz, S.J. Bame, D.N. Baker, J. Birn, J.T. Gosling, E.W. Hones, Jr., D.J. McComas, J.A. Slavin, E.J. Smith, R.D. Zwickl; Geophysical Research Letters, 11, 599, 1984.

11) Plasma Entry into the Distant Tail Lobes: ISEE-3; J.T. Gosling, D.N. Baker, S.J. Bame, E.W. Hones, Jr., D.J. McComas, R.D. Zwickl, J.A. Slavin, E.J. Smith, B.T. Tsurutani; Geophysical Research Letters, 11, 1078, 1984.

12) Detailed Examination of a Plasmoid in the Distant Magnetotail with ISEE-3; E.W. Hones, Jr., J. Birn, D.N. Baker, S.J. Bame, W.C. Feldman, D.J. McComas, R.D. Zwickl, J.A. Slavin, E.J. Smith, B.T. Tsurutani; Geophysical Research Letters, 11, 1046, 1984.

13) The Near Earth Current Sheet: ISEE-1 and -2 Studies; D.J. McComas and C.T. Russell; Achievements of the International Magnetospheric Study (IMS), ESA Scientific and Technical Publications, SP-217, 205, 1984.

14) Bistatic LIDAR Experiment Proposed for the Shuttle/Tethered Satellite System Missions; D.J. McComas, H.E. Spence, R.R. Karl, Jr., H.G. Horak, T.D. Wilkerson; Review of Scientific Instruments, 56, 670, 1985.

15) The Near Earth Cross Tail Current Sheet: Detailed ISEE-1 and -2 Case Studies; D.J. McComas, C.T. Russell, R.C. Elphic, S.J. Bame; Journal of Geophysical Research, 91, 4287, 1986.

16) The Average Magnetic Field Draping and Consistent Plasma Properties of the Venus Magnetotail; D.J. McComas, H.E. Spence, C.T. Russell, M.A. Saunders; Journal of Geophysical Research, 91, 7939, 1986.

17) Comet Giacobini-Zinner: A Plasma Description; S.J. Bame, R.C. Anderson, J.R. Asbridge, D.N. Baker, W.C. Feldman, S.A. Fuselier, J.T. Gosling, D.J. McComas, M.F. Thomsen, D.T. Young, R.D. Zwickl; Science, 233, 356, 1986.

18) The Warped Neutral Sheet and Plasma Sheet in the Near-Earth Geomagnetic Tail; J.T. Gosling, D.J. McComas, M.F. Thomsen, S.J. Bame, C.T. Russell; Journal of Geophysical Research, 91 7093, 1986.

19) Average Plasma and Magnetic Field Variations in the Distant Magnetotail Associated with Near-Earth Substorm Effects; D.N. Baker, R.C. Anderson, S.J. Bame, R.D. Bellian, P.R. Higbie, D.J. McComas, R.D. Zwickl, J.A. Slavin, E.J. Smith; Submitted to Journal of Geophysical Research, 1985.

20) Plasma and Magnetic Field Variations in the Distant Magnetotail Associated with Near-Earth Substorm Effects; D.N. Baker, S.J. Bame, D.J. McComas, R.D. Zwickl, J.A. Slavin, E.J. Smith; Accepted for publication in Chapman Conference on Magnetotail Physics Monograph, 1986.

21) The Average Configuration of the Induced Venus Magnetotail; D.J. McComas, H.E. Spence, C.T. Russell; Accepted for publication in Chapman Conference on Magnetotail Physics Monograph, 1986.

22) A Characterization of Large-Amplitude Plasma Fluctuations in the Transition and Sheath Regions of Comet Giacobini-Zinner; D.N. Baker, S.J. Bame, W.C. Feldman, S.P. Gary, D.J. McComas, J. Middleditch, R.D. Zwickl; Geophysical Research Letters, 13, 271, 1986.

23) Three Component Plasma Electron Distributions in the Intermediate Ionized Coma of Comet Giacobini-Zinner; R.D. Zwickl, D.N. Baker, S.J. Bame, W.C. Feldman, S.A. Fuselier, W.F. Huebner, D.J. McComas, D.T. Young; Geophysical Research Letters, 13, 401, 1986.

24) The Comet/Solar Wind Transition Region at Giacobini-Zinner; M.F. Thomsen, S.J. Bame, W.C. Feldman, J.T. Gosling, D.J. McComas, D.T. Young; Geophysical Research Letters, 13, 393, 1986.

25) Diagnostics of Space Plasmas; S.J. Bame, D.J. McComas, D.T. Young, R.D. Bellian; Accepted by Review of Scientific Instruments, 1986.

26) The Giacobini-Zinner Magnetotail: Tail Configuration and Current Sheet; D.J. McComas, J.T. Gosling, S.J. Bame, J.A. Slavin, E.J. Smith, J.-L. Steinberg; Submitted to Journal of Geophysical Research, 1986.

FIELD REVERSING MAGNETOTAIL CURRENT SHEETS:
EARTH, VENUS, AND COMET GIACOBINI-ZINNER

by

David John McComas

ABSTRACT

This dissertation examines the field reversing magnetotail current sheets at the earth, Venus, and Comet Giacobini-Zinner. In the near earth study a new analysis technique is developed to calculate the detailed current density distributions within the cross tail current sheet for the first time. This technique removes the effects of a variable sheet velocity by inverting intersatellite timings between the co-orbiting satellites ISEE-1 and -2. Case studies of three relatively geomagnetically quiet crossings are made; sheet thicknesses and peak current densities are ~1-5x10^4 km and ~5-50 nA/m^2. Current density distributions reveal a high density central region, lower density shoulders, and considerable fine structure throughout. In the Venus study another new analysis technique is developed to reconstruct the average tail configuration from a correlation between field magnitude and draping angle in a large statistical data set. The variability of the Venus tail data is explained in terms of

flapping of the current sheet as the tail tries to maintain a pressure balance condition under variations in the upstream IMF angle and, therefore, magnetic fluxes in the two lobes. The average magnetic field configuration and consistent plasma properties are derived; the flow velocity varies from ~-250 km/sec ($-8R_V$) to ~-470 km/sec ($-12R_V$), the average sheet and lobe densities are ~0.9 and ~0.07 amu/cm^3, the average O^+ temperature is ~9×10^7 K, and the integrated tailward mass flux is ~1×10^{26}amu/sec. In the comet study, high resolution magnetic field and plasma electron data from the ICE traversal of Giacobini-Zinner are combined for the first time to determine the tail/current sheet geometry and calculate certain important but unmeasured local ion and upstream properties. Pressure balance across the tail gives ion temperatures and betas of ~1.2×10^5 K and ~40 in the center of the current sheet to ~1×10^6 K and ~3 in the outer lobes. Axial stress balance shows that the velocity shear upstream near the nucleus is >6 (~1 at ICE), and that a region of strongly enhanced mass loading (ion source rate ~24 times that upstream from lobes) exists upstream from the current sheet. The integrated downtail mass flux is ~2.6×10^{26} H_2O^+/sec, which is only ~1% of the independently determined total cometary efflux.

CHAPTER 1

Introduction

1.0 Magnetotails and Their Field Reversing Current Sheets

Magnetotails arise out of the solar wind's interaction with magnetic and mass loading planetary and cometary bodies throughout the solar system. While the details of magnetotail structures vary from one planetary body to the next, certain attributes are inherent to magnetotails in general. These include the juxtaposition of two lobes of nearly oppositely directed magnetic fields and a field reversing current sheet which acts to separate them. Through these current sheets the field rotates from one lobe's orientation to the other, everywhere self-consistently satisfying Ampere's Law.

This dissertation examines three such magnetotails in general and their field reversing current sheets in particular. The three magnetotails are associated with very different sorts of inner solar system bodies. These bodies are: 1) the earth, 2) Venus, and 3) Comet Giacobini-Zinner (G-Z). These three were chosen not just because of their considerable scientific interest, but also because each represented a different type of interaction with the solar wind. By examining the different manifestations of magnetotails and field reversing current sheets, this dissertation attempts to convey some of the richness of variety which these structures display.

Time dependent effects are often extremely important in

determining the instantaneous structure and properties of magnetotails and their current sheets. Examples of such effects include variations of the solar wind and Interplanetary Magnetic Field (IMF) properties upstream from all three bodies, near earth reconnection and consequent substorm activity at earth, variations in the near nightside magnetic structure at Venus, and spatial and temporal fluctuations in the neutral outgassing rate of Comet G-Z. While these effects are all extremely interesting in their own rights, the fundamental, average magnetotail/current sheet properties are time independent. In order, therefore, to examine the fundamental current sheet properties within the three magnetotails, this dissertation concentrates on the time independent aspects.

The fundamental planetary/cometary property which dominates a body's interaction with the solar wind and, therefore, the nature of the magnetotail which forms antisunward from it, is the magneto-hydrodynamic (MHD) obstacle which it presents to the flowing solar wind/IMF. At bodies with substantial intrinsic magnetic fields, such as the earth, Mercury, Jupiter, Saturn, and Uranus, the solar wind flow is essentially diverted entirely by the region dominated by this intrinsic field. At bodies which lack substantial intrinsic magnetic fields but possess appreciable gaseous atmospheres, such as comets, Venus, and some of the outer solar system planetary satellites, mass loading of the flow and the formation of a conductive ionosphere serve to divert the solar wind flow. For these atmospheric obstacles, the presence (Venus) or absence (Comet

G-Z) of a substantial gravitational field determines whether a compact or extended mass loading region is formed.

The flowing solar wind/IMF can be diverted about a body by either an intrinsic planetary magnetic field or by mass loading of the flow and the formation of a conductive ionosphere. Of course some bodies in the solar system have neither an intrinsic magnetic field nor a sufficient atmosphere to mass load the solar wind or produce a conductive ionosphere. The moon and, probably, asteroids also, are examples of such bodies. The region antisunward of such an obstacle, however, is *not* a magnetotail, but rather a wake. These wakes are essentially devoid of plasma since the solar wind is not deflected about the obstacle, but is absorbed as it collides with the body's surface. Since magnetotails and magnetotail current sheets are not formed at such obstacles, they will not be considered further in this dissertation.

1.1 Intrinsic Magnetotail: Earth

Of the three magnetotails studied in this dissertation, only the earth's contains magnetic fields which are connected to the planetary obstacle. When a planetary body possesses a substantial intrinsic magnetic field, as does the earth, the flowing solar wind acts to deform the intrinsic magnetic cavity surrounding the planet. This has the effect of compressing the cavity on the dayside and stretching it out on the nightside into a tail-like configuration. Tailward elongation of the magnetosphere occurs both because of tangential stresses or drag at the magnetopause boundary and because

of magnetic reconnection between the planet's intrinsic magnetic field and the IMF.

Magnetic reconnection between the shocked IMF (magnetosheath field) and the intrinsic planetary field occurs preferentially near the nose of the magnetopause at times when the two fields are oppositely directed (i.e., when the IMF has a negative B_Z-component). Interconnection between the magnetosheath and lobe fields travels tailward along the magnetopause, and the magnetosheath flow thereby acts to drape back the magnetic field in the tail into nearly oppositely directed lobes. In contrast to the lobes, where the magnetic field at least partially interconnects the planetary ionosphere and the IMF, the near earth cross tail current sheet consists of field lines which are connected to the ionosphere at both ends. In the steady state picture, the near earth current sheet plasma and magnetic field are slowly convected earthward from a region where the two lobes are undergoing steady state reconnecting, somewhere deep in the tail.

In light of the already very substantial knowledge of the general characteristics of the terrestrial magnetotail and its field reversing current sheet, this dissertation avoids a reexamination of these general properties. Rather, it extends the frontier of knowledge by determining detailed current density distributions in the near earth cross tail current sheet for the first time. This study is carried out in Chapter 2 through the development and use of a new multisatellite data analysis technique.

High resolution magnetic field and plasma data from the

co-orbiting satellites ISEE-1 and -2 are combined in order to resolve the current sheet geometry and orientation at the time of spacecraft crossings. The magnetic field data is then used to make careful intersatellite timings of the motion of the current sheet and derive the detailed cross tail current density distributions through the sheet. These distributions will be shown to exhibit substantial fine structure, and the implications of this structure will be discussed.

The orientation of the orbits of the ISEE-1 and -2 spacecraft remain essentially fixed throughout the year so that they are in an advantageous position to sound the near magnetotail for only approximately four months each year (mid-February to mid-June). During the years since the 1977 launch, the orbits have slowly evolved so that the spacecraft spend progressively more time in the southern lobe and make fewer current sheet crossings. Consequently, the special criteria required to resolve the current sheet geometry with only two spacecraft, as described in detail in Chapter 2, are far less likely to occur later in the mission.

In any case, the magnetic field data for the four month intervals have been carefully examined from the start of mission through 1983. From the few analyzable crossings found in the data, three which were almost certainly not associated with substorm activity were chosen for detailed analysis. In this way, the average or steady state structure of the current sheet is most nearly examined. In the future, the European Space Agency CLUSTER Mission, which is designed to combine four co-orbiting satellites,

should be able to make substantial use of the new technique developed in this section.

1.2 Induced Magnetotails

At planetary and cometary bodies which possess substantial atmospheres but no intrinsic magnetic fields, magnetotails can still form from the solar wind interaction. Unlike the case of intrinsic magnetotails such as the earth's, however, the magnetic fields comprising induced magnetotails are of purely solar origin. The plasma in induced magnetotails, on the other hand, is largely of planetary or cometary origin and has been added to the flow through photoionization, charge exchange, or other similar mass loading processes.

The general solar wind/IMF interaction with such bodies consists of draping of the magnetic field due to mass addition and slowing of the flow, and is described in more detail in the introductory sections of Chapters 3 and 4. Briefly, the magnetic field immediately adjacent to the tail continues to be carried along by the relatively unimpeded flow while the flow passing near to the obstacle is mass loaded and slowed. In addition, formation of a conductive ionosphere serves to exclude the upstream flow, further slowing and diverting it. Since the field links the regions of greater and lesser flow speeds, the field configuration becomes highly draped and a magnetotail configuration forms, complete with oppositely directed tail lobes and a self-consistent, field reversing current sheet.

1.2.1 Venus

Venus represents an example of an induced magnetotail forming body which has an essentially gravitationally bound neutral atmosphere. As such, the amount of neutral gas above the Venus ionosphere is limited and drops off very quickly with distance from the planet. The plasma flow directly upstream from the planet is therefore slowed over a relatively short distance, and the field directly upstream piles up above the dayside ionopause. The magnetotail which forms in this interaction is demarked by relatively sharp and well-defined tail boundaries.

Even though the Pioneer Venus Orbiter, PVO, has been in orbit around Venus since 1978, the detailed average properties of the Venus magnetotail have not been determined prior to the work described in Chapter 3 of this dissertation. This was due to the extremely large amount of variability of the tail's magnetic configuration and location, due to fluctuations in the upstream IMF orientation and solar wind properties, which occurs on a few-minute time scale. Exacerbating this problem is the general lack of plasma observations attainable within the tail with any of the plasma analyzers carried onboard PVO. Therefore, unlike the earth study in Chapter 2, the Venus magnetotail study described in Chapter 3 centers on the more general, average properties of the Venus magnetotail and its field reversing current sheet.

In order to carry out such a study, which would provide much more information about the average configuration and properties than previous case studies of the tail, a new method for analyzing the

highly variable tail field data was needed. In the Venus chapter of this dissertation just such a technique is developed. This technique allows the data to be organized by distance from the field reversing current sheet rather than by location in inertial space. Nearly 10,000 one-minute averaged magnetic field data samples are statistically examined in these new coordinates, and the average magnetic configuration of the Venus magnetotail is determined. From this derived average field configuration, and using an MHD analysis, the self-consistent, average plasma properties of the tail are derived for the first time.

1.2.2 Comet Giacobini-Zinner

While many aspects of cometary interactions with the solar wind are similar to those at Venus, the extremely small gravitational attraction of a comet combined with its continual gas efflux causes the cometary obstacle to be much more extended. Inside the extended region of mass loading, a cometary ionopause is expected to form near to the nucleus where the ion density is so large that at least partial exclusion of the upstream field occurs. Ion tails observed visually from earth and initial G-Z magnetotail results indicate that cometary magnetotails apparently also have well-defined boundaries, even though the global cometary interactions are so extended.

The magnetotail traversal of Comet Giacobini-Zinner by the International Cometary Explorer (ICE) on 11 September 1985 represents the first, and only, scheduled, in situ observations of a

cometary magnetotail. Unlike the Venus tail studied in Chapter 3, the G-Z magnetotail data set consists of only a single tail crossing. Therefore, no statistical derivation of the average tail properties is possible, and the observed properties of the tail must simply be assumed to be typical. Also unlike the Venus case, however, the plasma electron properties of the crossing were measured along with the magnetic field properties, allowing for a much better analysis of the single crossing data sets.

In Chapter 4 of this dissertation the high resolution magnetic field and plasma data sets for the ICE tail traversal are combined for the first time. Together they allow for the determination of the magnetotail configuration at the time of the spacecraft crossing. From an MHD analysis of these combined data, the upstream conditions at the average pick-up locations near to the comet nucleus are also derived, and with them the detailed tail formation process is examined.

CHAPTER 2

The Near Earth Cross Tail Current Sheet: Detailed ISEE-1 and -2 Case Studies

2.0 Chapter Overview

Three near geomagnetic tail current sheet crossings of the ISEE-1 and -2 satellites on 5 April 1979 are examined in detail. All are associated with the passage of an interplanetary shock and the region of variable solar wind pressure behind it. The general geometry of field reversing current sheets is discussed, and this geometry is examined for the cases studied, by using the ISEE-1 and -2 co-orbiting satellite data sets. A new technique is employed which removes the effects of a variable sheet normal velocity for the first time. This allows us to calculate firm upper bounds on the current sheet thicknesses, and by utilizing certain physically motivated assumptions, determine the most probable actual sheet thicknesses, and inclinations of the field lines within these sheets. Current density profiles derived with this technique show the main cross tail current sheet to be a structure that is many thermal ion-gyroradii thick and which is sometimes embedded in a region that is three or more times thicker and contains much smaller current densities. These profiles also exhibit a considerable amount of fine structure in the sheet which appears as narrow peaks in the current density distributions. Possible explanations for

these structures, and for the overall sheet structure itself, are examined.

2.1 Introduction

Current sheets are ubiquitous in space plasmas. These sheets carry current distributions through regions of spatially varying magnetic fields such that the current density and magnetic field configurations everywhere self-consistently satisfy Ampere's Law. One interesting class of current sheets, field reversing sheets, forms when two nearly antiparallel portions of a magnetic field abut each other. Interplanetary sector boundaries and lobe separating magnetotail current sheets are examples of field reversing sheets. Since this study will examine the near earth, cross tail current sheet which serves to separate the oppositely directed magnetic fields in the geomagnetic tail lobes, a brief discussion of such sheets in intrinsic magnetotails is appropriate.

Intrinsic magnetotail current sheets form in the central portions of magnetotails antisunward of planets with intrinsic magnetic fields, such as the earth, Jupiter, Saturn, and Mercury. The solar wind deforms the intrinsic planetary field, stretching out field lines behind the planet. In addition, dayside merging causes magnetic flux to be added to the tail lobes. A magnetotail configuration is therefore formed, with adjacent lobes of roughly antiparallel fields separated by a central cross tail current sheet.

In the theoretical limit of the so-called Harris neutral sheet [Harris, 1962], a one-dimensional equilibrium current sheet solution

is found for a current sheet separating antiparallel fields. In actual planetary magnetotails, reconnection and three-dimensional effects can alter this geometry and create regions of very different magnetic topologies. Planetward of an X-type neutral line, field lines connect to the ionosphere. Stresses in the magnetotail are communicated to the ionosphere, and the ionospheric responses are in turn communicated to the tail. Tailward of an X-line on reconnected interplanetary magnetic field (IMF) lines, the boundary conditions are vastly different. Current sheets in these disconnected portions of the tail have magnetic topologies similar to induced magnetotail current sheets such as are observed at Venus [Russell et al., 1981] and postulated to exist antisunward of comets. Such a field geometry is highly kinked and mass loaded throughout the sheet. The magnetic field tension acts to accelerate the plasma and reduce the total sheet current by restraightening the field to the local IMF configuration. Another type of magnetic field topology can form when reconnection initiates on closed (i.e., connected to the earth at both ends) field lines, namely an O-type neutral line [Russell, 1974] or plasmoid [Hones, 1979]. The fully three-dimensional magnetic configurations of these structures and their associated current systems are quite complicated, and are an area of considerable current research [Hones et al., 1982, 1984]. This study is concerned with the simple, field reversing, near earth current sheet, and will not examine disconnected or plasmoid-embedded sheets.

Prior to the launch of the co-orbiting satellites, ISEE-1 and

-2, studies of current and plasma sheet topologies and dynamics had necessarily relied on data taken from single or widely separated spacecraft. The use of single spacecraft data sets is useful for the purpose of making large statistical studies of average current sheet properties (e.g., Fairfield [1979], [1980]), but it is impossible to separate spatial and temporal effects with data taken from only one location. Even with two-spacecraft observations a fully three-dimensional geometry which may vary as a function of time cannot be uniquely resolved. Magnetic field topologies in current sheets may, in general, be quite complicated (see, for example, Lui [1983]), and the sheet may even have closed magnetic structures embedded in it. For the purposes of this study, however, only current sheet crossings which exhibit planar, monotonic field variations have been chosen. This greatly simplifies the problem of resolving the sheet geometry with two-spacecraft observations. In addition to these constraints, the intersatellite separation vector must lie well out of the plane of the current sheet in order to make a reliable determination with our technique. Out of all of the ISEE-1 and -2 current sheet crossings from the 1978 and 1979 tail orbital seasons, six crossings were identified which exhibited fast and relatively smooth, monotonic field variations in the data sets of both of the spacecraft, and for which the intersatellite separation vectors are a suitably large angle from the planes of the current sheets.

It is the purpose of this paper to discuss the geomagnetic cross tail current sheet in the near earth region through the

detailed examination of three case studies. Very fast sheet crossings were chosen in order to minimize the effect of temporal variations of the sheet structure itself. Since the geomagnetic tail, in general, and the plasma sheet, in particular, are subject to large and rapid variations as a function of substorm phase, [McPherron et al., 1973; Hones, 1979, and references therein] current sheet crossings were specifically chosen to avoid times of large substorm activity. Specifically, all three were chosen from a day when the variable pressure region behind an interplanetary shock caused large scale motions of the magnetotail and repeated encounters between the current sheet and the ISEE-1 and -2 satellites. Bulk reorientations of the magnetotail, due to variations in the solar wind flow, caused substantially enhanced geomagnetic activity on this day. Therefore, the crossings studied here cannot be considered to be representative of "quiet" current sheet crossings. They do, however, probably represent crossings caused by bulk motions of the tail, and not internal substorm related reconfigurations, as will be discussed in greater detail in following sections.

2.2 Current Sheet Geometry

The natural coordinate system for examining simple sheet crossings is a local, current sheet normal coordinate system. In this system, the current sheet is assumed to have surface boundaries which are planar and parallel on the size scale of the satellite separation vector. Magnetic field lines rotate through the current

sheet so that the fields on opposite sides of the sheet are roughly antiparallel. Since only simple sheet crossings are examined here, the field rotation through the sheet is assumed to be symmetric about the current sheet midplane. This quite reasonable assumption greatly reduces the ambiguity in the field geometry since the axis of symmetry is easily resolved from single satellite magnetometer data alone. This axis is defined to be the direction in which the field undergoes its maximum variance for the crossing, and is labeled as the L-axis throughout this study. The ratio of the maximum to the intermediate eigen values from the minimum variance analysis indicates how well this axis is defined.

Figure 2.1 shows the field geometry of a simple current sheet in the boundary normal coordinate system. The N-axis defines the current sheet normal, while the M-axis lies in the plane of the sheet and completes the right-handed set. In the nominally expected magnetotail configuration, the L,M,N axes would correspond roughly to the GSM X,Y,Z coordinates, respectively. The L,M,N coordinates, however, describe a local coordinate system which may be quite different from the nominal configuration if the sheet surface is wavy, as has been suggested of the plasma sheet boundary by Lui et al. [1978], or if the tail becomes torqued around by the IMF B_Y-component, as is suggested to occur in the deep geomagnetic tail [Sibeck et al., 1985].

For the current sheet crossings examined in this study the magnetic field rotations are essentially confined to a plane, which is defined to be the L, n plane for the purposes of this study. In

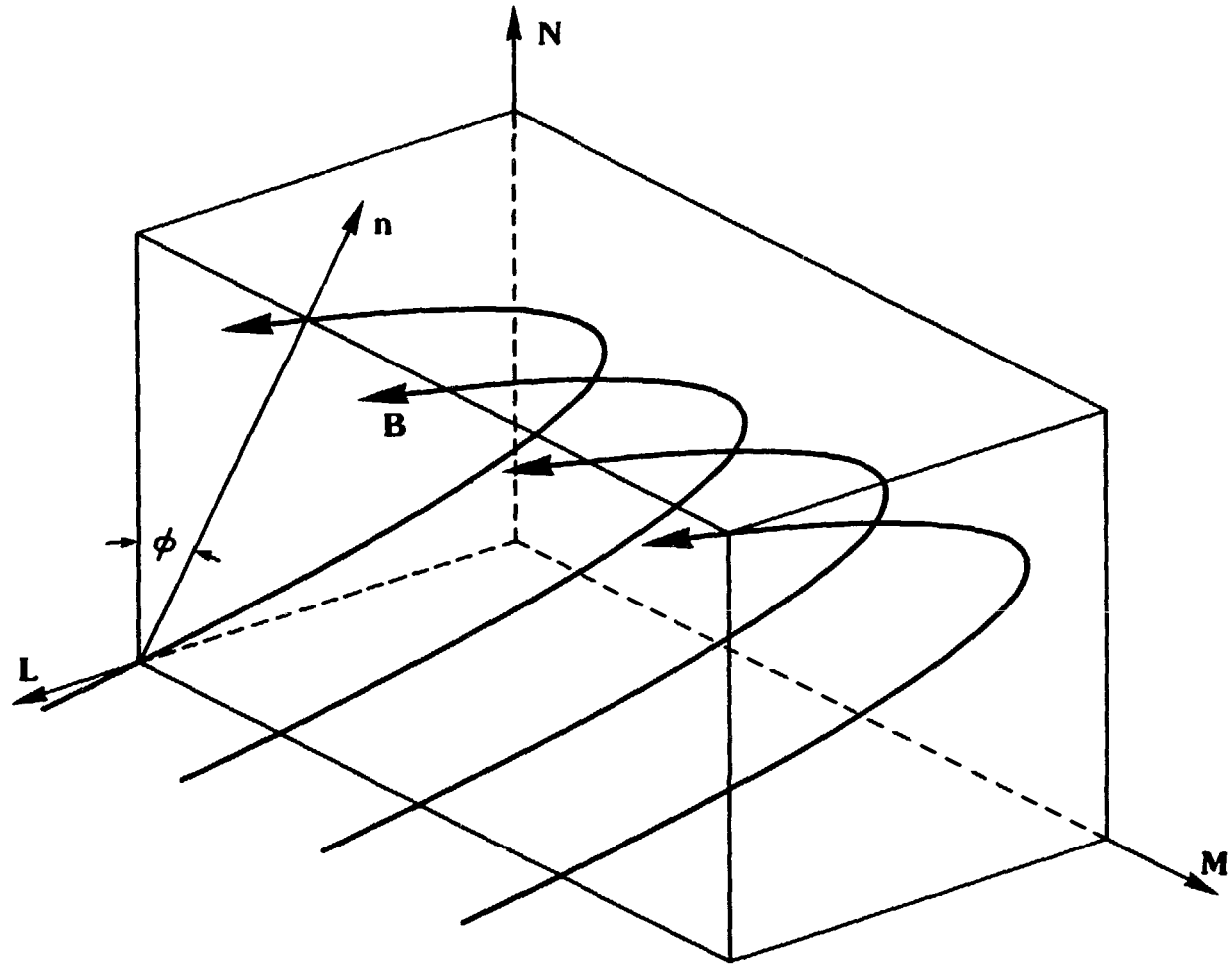

Fig. 2.1. Magnetic field line rotations in the cross tail current sheet. The planes of the field lines are inclined with respect to the sheet normal by the angle ϕ. The L axis bisects the field rotation while current flows self-consistently in the M direction.

practice, the m- and n-axes are chosen so that the magnitude of B_m and B_n are essentially zero and constant respectively, through the crossing. Of course it is possible that the magnetic field rotation through the sheet is not well confined to a plane, making it impossible to find an axis such as m for which the field component remains essentially zero through the crossing. If the sheet crossing does not have the simple symmetric and planar properties delineated above, then the structure of the current sheet at that time and location must be more complicated than the simple model, and the case is rejected. In general, however, this criterion has been satisfied by the simple crossings which were chosen from overview data plots. The plane defined by the magnetic field rotation, as shown in Figure 2.1, may in general be inclined by the arbitrary angle, ϕ, with respect to the current sheet normal, N.

Once the geometry has been fully determined, spatial and temporal effects can be separated in the dual satellite data by careful intersatellite timing. For a current sheet with planar, parallel surfaces, as assumed here, only the component of the sheet motion perpendicular to the surface (in the N-direction) is observable with intersatellite timing. Unfortunately, the current sheet geometry is not fully determined as is demonstrated in Figure 2.2. In this figure, the geometry has been reduced to the plane, P, of the four coplanar vectors; M, N, m, and n. This is possible because the L-axis is uniquely known, and motions of the sheet parallel to the L-axis are unobservable with intersatellite timing, since the sheet is assumed to be uniform in the L-direction.

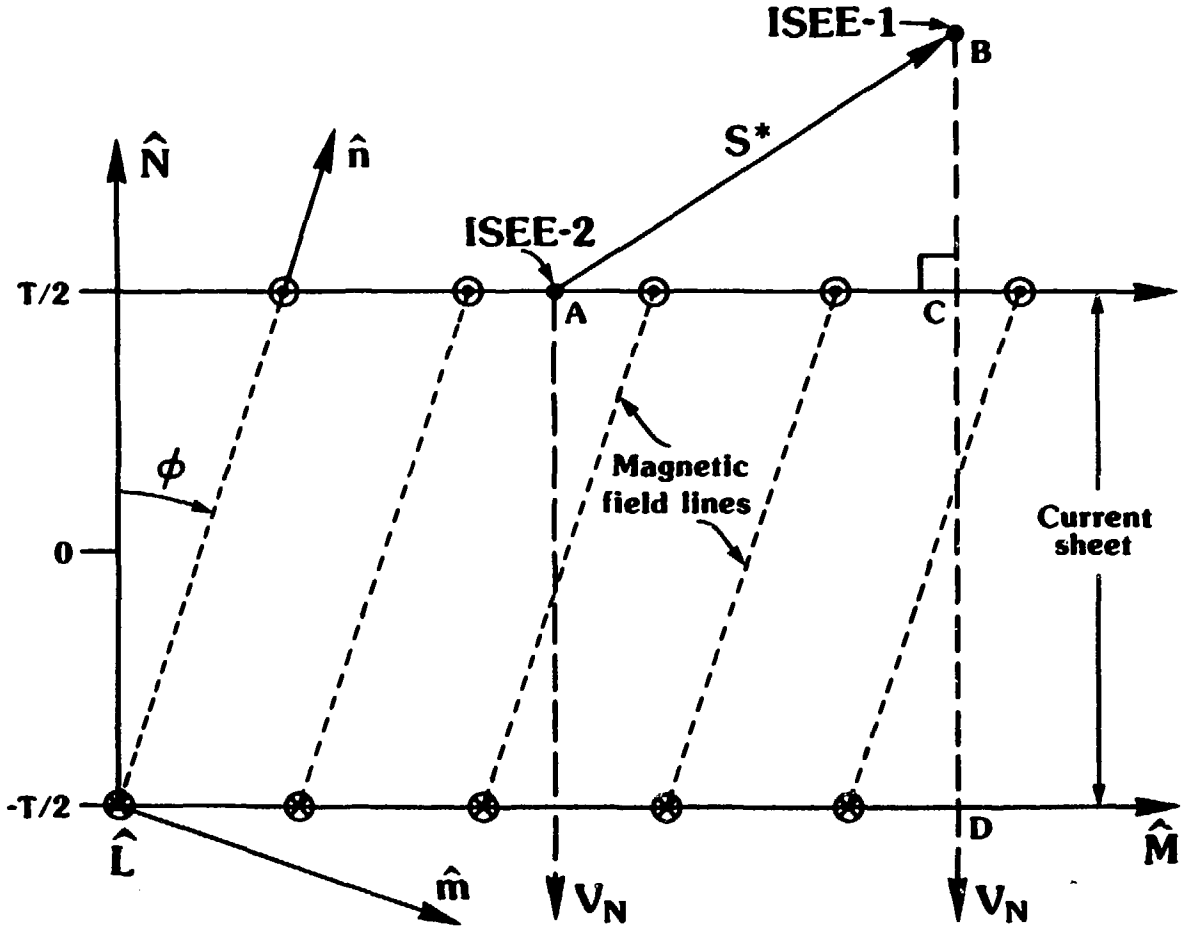

Fig. 2.2. Cross sectional cut through the current sheet in the plane perpendicular to the L axis. $\underline{S}^*$ is the projection of the satellite separation vector into this plane. The field line axes, m and n, are well defined as is $\underline{S}^*$, but the angle to the actual sheet normal ϕ, is not known.

The m- and n-axes are also well known, as described previously, but the arbitrary rotation angle, ϕ, is completely unknown. This ambiguity in the geometry is a central theme for this study. By making physically motivated assumptions about the geometry, the structure of the sheet is examined and this ambiguity is partially resolved.

Since the normal to plane P, namely L, is well specified, it is possible to obtain the component of any known vector, $\underset{\sim}{A}$, in the plane. The general formula for the component of $\underset{\sim}{A}$ in the plane, $\underset{\sim}{A}^*$, is $\underset{\sim}{A}^* = \hat{L} \times (\underset{\sim}{A} \times \hat{L})$. This method is used, for example, to determine the component of the Z_{GSM}-axis in this plane. The unit vector in this direction in the plane is called $\hat{N}_{NOM}$ as it represents the expected nominal direction for the sheet normal given that the X_{GSM} axis has been rotated to the L-direction. In particular, $\hat{N}_{NOM} \propto \hat{L} \times (\hat{Z}_{GSM} \times \hat{L})$, and is a well specified vector since both the L-and Z_{GSM}-directions are well specified and usually nearly orthogonal. This definition of the nominal normal will be used in the ensuing sections to provide a baseline current sheet geometry consistent with the observed field rotations.

The component of the ISEE 1-2 separation vector which lies in the plane P, is labeled $\underset{\sim}{S}^*$ in Figure 2.2. $\underset{\sim}{S}^*$ is similarly defined by $\underset{\sim}{S}^* = \hat{L} \times (\underset{\sim}{S} \times \hat{L})$, where the separation vector, $\underset{\sim}{S}$, and the maximum variance axis, L, are both well specified. Just as for the L-direction, the component of $\underset{\sim}{S}^*$ parallel to the M-axis is also unobservable with the intersatellite timing since the sheet is assumed uniform in the M-direction. Only the component of the

separation vector parallel to the N-axis, $S_N = \underset{\sim}{S} \cdot \hat{N}$ is used in determining the sheet normal velocity.

If a constant normal velocity, v_N, is assumed, then this velocity can be determined by dividing S_N by the time lag, $\Delta\tau_{BC}$, between the initial encounters with the sheet seen at the two spacecraft (points B and C in Figure 2.2). The thickness of the sheet, T, is then simply the product of the normal velocity, v_N, and the duration of the crossing, $\Delta\tau_{CD}$. This type of analysis has been discussed in greater detail by McComas and Russell [1984]. Figure 2.2 is drawn with the satellites moving in the N-direction which is geometrically equivalent to the actual case of the sheet moving in the minus N-direction on the short time scale of the crossing. It will be shown in the next section that a variable velocity profile can also be approximately calculated from a series of similar timings and, therefore, the effect of this variation can be essentially removed from the data.

It is possible to calculate a maximum current sheet thickness for any crossing by finding the sheet thickness parallel to the arbitrarily oriented vector $\underset{\sim}{S}^*$. This is accomplished by letting $S_N = |\underset{\sim}{S}^*|$, since $S_N = \underset{\sim}{S} \cdot \hat{N} < |\underset{\sim}{S}^*|$. This limiting thickness, T_{MAX}, would be highly variable, even if all current sheets were the same thickness, since the angles between $\underset{\sim}{S}^*$ and $\hat{N}$ are arbitrary. These thicknesses in all cases, however, set firm upper bounds on the actual sheet thicknesses.

2.3 Current Sheet Motions

It is critically important to determine the current sheet normal velocity in order to measure the basic sheet properties such as thickness and current density distribution. While an average crossing velocity is sufficient to determine the sheet thickness and total integrated current, a detailed knowledge of the instantaneous velocity as a function of time, through the crossing, is required to calculate the exact current density distribution. This is because the current density is calculated from the curl of the magnetic field by Ampere's Law, $\nabla \times \underset{\sim}{B} = \mu_o \underset{\sim}{J}$. For the typical field geometry found in the near magnetotail B_L is not a strong function of M, and both B_M and B_N have roughly constant, non-zero values. Since they are comparatively weak functions of the spatial coordinates, they do not contribute substantially to the curl of $\underset{\sim}{B}$, and currents are driven essentially parallel to the M-axis. The curl of the field in the L,M,N coordinate system is therefore simply $\mu_o J_M = \partial B_L / \partial N$, where ∂B_L and ∂N are replaced in practice by ΔB_L and $\Delta N = V_N \Delta t$, respectively. If v_N is an unknown function of time, the current density distribution is indeterminate. This essential ambiguity has made it impossible to calculate reliable current density distributions in current sheets until now.

We have developed a program to calculate the sheet normal velocity as a function of time. The only assumption required for this analysis is that all locations within the sheet and in the region of the crossing which have equal B_L magnitudes occur at the same distance from the sheet midplane. This assumption, however, is

not new since it is equivalent to assuming that the sheet is constant in L and M on the size scale of the satellite separation vector, and does not change much on the intersatellite timing timescales. Since the separation vector is typically only a few thousand kilometers, and since the crossings are selected specifically to be of short duration, typically a few minutes, this assumption is reasonably valid at all but active substorm times.

Another effect which will tend to complicate our analysis is the possibility of compressional waves in the plasma sheet. Standing compressional waves, however, should produce quasi-periodic variations of the field which are not observed in the crossings studied here. The effect of impulsive (non-periodic) compressional waves is to reduce the accuracy of our technique by superimposing "noise" on the larger variations of the current sheet crossings. These waves, however, will tend to cause B_L to vary non-monotonically across the sheet and, since we only analyze crossings with monotonic B_L variations in this study, such waves cannot be of primary importance for cases studied here.

The magnetic signature of a typical quick current sheet crossing, which occurred between 15:42 and 15:56 UT on 5 April 1979, is shown in the upper panel of Figure 2.3. The data are shown in the L,m,n coordinate system, and a small data gap has been filled in the B_L-component by interpolation, just after 15:53. The magnitudes of B_{L2} at t_i and B_{L1} at t_j are equal by construction, as are the magnitudes of B_{L2} at t_j and B_{L1} at t_k. The time lags between the two points, t_{lag}, are simply $t_j - t_i$, and $t_k - t_j$, for the two

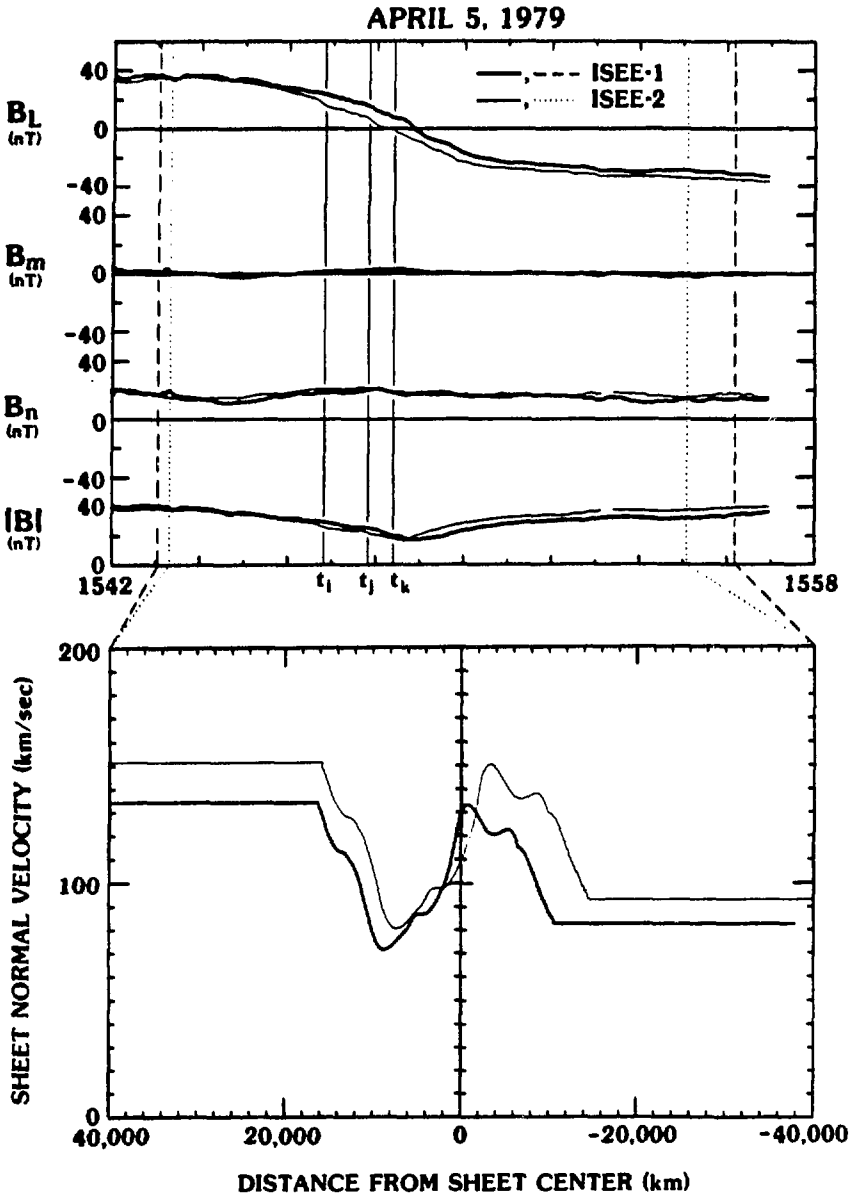

Fig. 2.3. Magnetic field data in the L,m,n coordinate system for the crossing which occurred at ~15:50 UT at -17.6,-3.2,0.2 R_EGSM (top panel). Intersatellite timing is derived for each distance from the current sheet center, and these timings are inverted to yield the sheet normal velocity as a function of location (see text for details). Note that $B_m \approx 0$ while $B_n \approx$ constant value, as expected for a field line rotating in the L,n plane. The bottom panel displays the calculated velocities as a function of location in the sheet. The horizontal portions on the ends are simply extrapolations of the last reliably determined velocities.

periods, respectively. By similarly calculating t_{lag} at all times through the crossing, an approximately normal crossing velocity as a function of time can be deduced.

The sheet normal velocity calculated for any particular t_{lag}, bounded by the times when the first satellite reaches a particular B_L value and when the second satellite reaches the same B_L value, is an average velocity over all instantaneous velocities between these two times. Still referring to the upper panel of Figure 2.3, the actual instantaneous velocity at time t_j is averaged into all velocities calculated from the time lags which begin or end at any time between t_i and t_k. For a velocity profile which is relatively constant on the timescale of t_{lag}, the approximate velocity at time t_j is just the average of the velocities calculated using the time lag method between times t_i and t_k. With this method an approximate normal velocity crossing profile is derived for the entire central portion of the sheet crossing. This method breaks down only on the sides of the crossing since the two curves converge there and intersatellite timing becomes impossible. The fact that the two do not completely converge on the right-hand side of the crossing shown indicates that the assumption of a planar, parallel geometry is not strictly true, or that the satellites did not sound completely through on this side of the sheet crossing.

The lower panel of Figure 2.3 shows the normal velocity profiles for the ISEE-1 and -2 spacecraft for the crossing. Prior to calculating this velocity profile, the field data in the upper panel was filtered with a Kaiser low pass filter with a cutoff

frequency of .025 Hz. This value was chosen since it corresponds to a timescale of 40 seconds, which is a typical value for the time lags between the two spacecraft, determined as described previously for this crossing. Filtering the field data with a cutoff value of t_{lag} insures that a reliable velocity profile is derived, and this procedure is carried out for all cases in this study. The constant velocity sections at the two ends are simply extensions of the last reliable velocity calculated.

The procedure described here, and the program which has been developed to implement it, provides a number of important advantages over simply assuming a constant normal velocity, as has been done previously. The technique, however, does not derive the actual instantaneous velocity profile, but rather a smoothed version of this profile where high frequency variations ($\tau < t_{lag}$) have been filtered out. This technique therefore provides the best results when t_{lag} is typically much smaller than the total time of the crossing. Higher time resolution velocity profiles are undetermined from the two-satellite data available. The averaging technique described herein provides the best solution for the sheet normal velocity with the only caveat that those structures seen which correspond to timescales less than t_{lag}, are not reliably determined.

2.4. Case Studies: 5 April 1979

Just prior to 2:00 UT on 5 April 1979, an interplanetary shock arrived at IMP-8 which was located in the solar wind in near earth

orbit at approximately (-2,22,27) R_E in GSM coordinates. The IMF magnitude at this location rose from a value of 13 nT upstream of the shock to ~60 nT just downstream, and persisted until ~15:00 UT when it began to drop back to the pre-shock value which it reached at about 21:00 UT. The top two panels of Figure 2.4 show the entire day of magnetometer data taken 220 R_E upstream at ISEE-3, and taken near the magnetosphere at IMP-8, respectively. The traces are quite similar, although shifted in time approximately forty minutes, which is consistent with the solar wind transit time for 200 R_E. These observations suggest that the shock and related structures have spatial scale sizes sufficiently large to affect the magnetosphere as a whole. The downstream region is marked by numerous field rotations and variations in the total field strength. ISEE-3 plasma data (not shown) indicate that the number density and flow velocity are highly variable throughout the post-shock region. The plasma pressure jumps across the shock by about a factor of seven, and is also highly variable (P_{max}/P_{min} ~30) throughout the day. These variations in flow direction and solar wind pressure cause substantial variations in the compression and orientation of the geomagnetic tail. On this day the co-orbiting satellites, ISEE-1 and -2, were traversing near the midplane of the geotail and, therefore, were in an ideal position to cross the tail current sheet. The magnetometer data from ISEE-2 for this entire day is shown in the bottom panel of Figure 2.4. Reversals of the X-component of the field show that the current sheet was repeatedly encountered and crossed. From this set of partial and complete

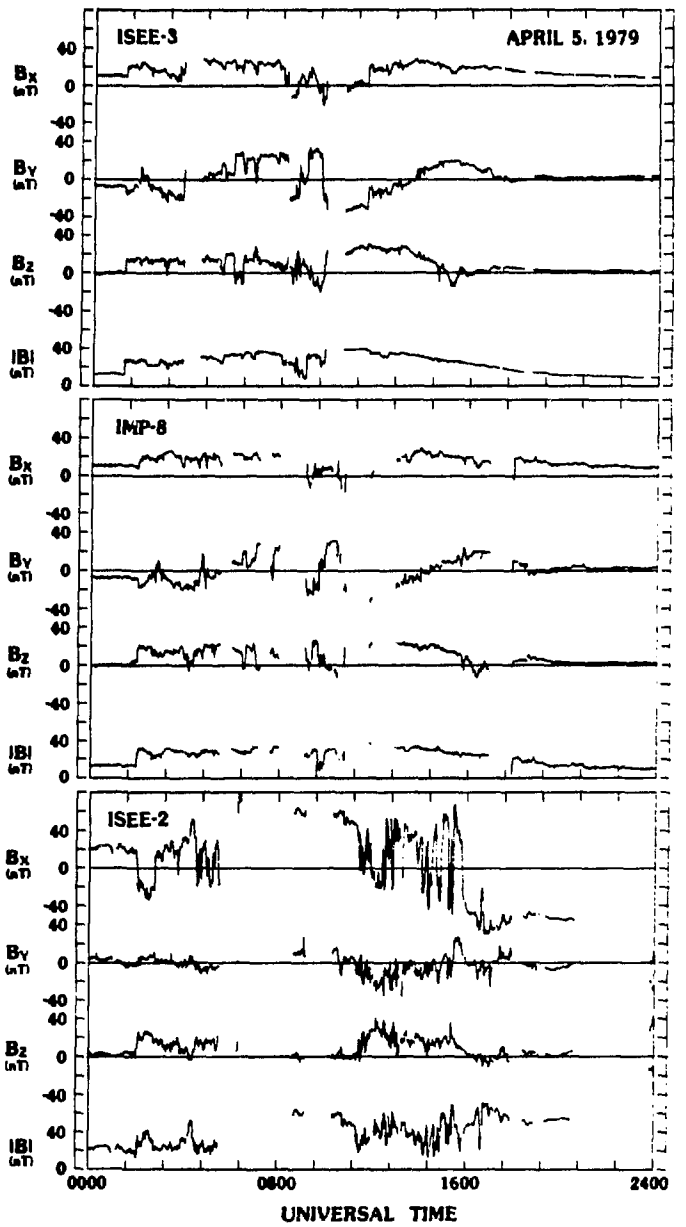

Fig. 2.4. From top to bottom the magnetic field data from ISEE-3, 220 R_E upstream in the solar wind, IMP-8, in the near-earth solar wind, and ISEE-2, near the midplane of the magnetotail current sheet, ~18 R_E behind the earth. The arrival of the interplanetary shock is easily observable at ISEE-3 at ~0120 UT, and ~40 minutes later near the earth. The ISEE-2 satellite B_X reversals indicate that the satellite made frequent current sheet traversals throughout the day.

crossings, three particularly simple and interesting crossings have been chosen for analysis.

Ion density, thermal energy temperature, and pressure data from the ISEE-2 Los Alamos/MPE Fast Plasma Experiment are shown in Figure 2.5, from 12:00-18:00 UT, on this day. Regions identified by the cross hatching in the figure are based on the plasma parameters and greyscale spectrogram (where count rate as functions of angle and energy are indicated by plot intensity) representations of the data, and were arrived at independently from the magnetometer data. Plasma sheet intervals are easily discernible in the greyscale spectrograms, and are indicated in the moments by periods of enhanced plasma pressure. The magnetic field data (Fig. 2.4) shows regions of roughly constant field strength on either side of the current sheet crossings, while the plasma data indicates that the ISEE-2 satellite continued to be enveloped within the plasma sheet throughout much of the interval. This comparison between the two data sets indicates that the plasma sheet traditionally defined observationally from the plasma data [Bame et al., 1966, 1967] as the region of enhanced particle populations, and the cross tail current sheet defined as the region of substantially enhanced current density, are not equivalent. This difference will be examined in greater detail in Section 2.5.

Rapid and smooth crossings of the geotail current sheet are relatively uncommon in the ISEE data sets, and are most often associated with geomagnetic storm and substorm activity. The crossings studied here, however, were specifically chosen to be

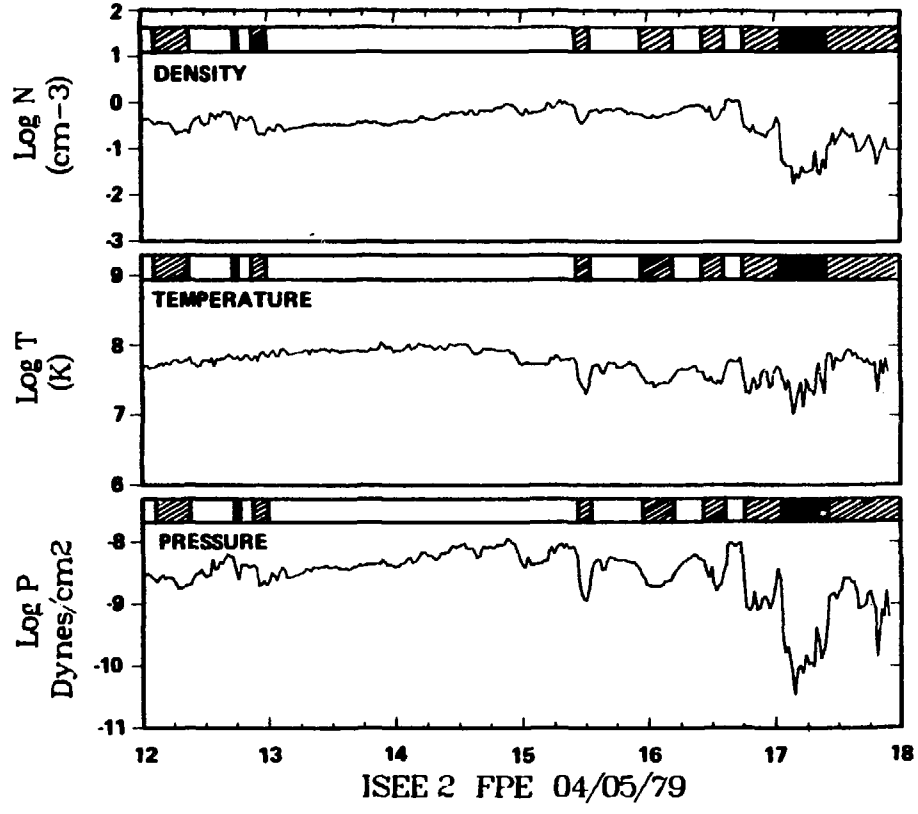

Fig. 2.5. Plasma moments at the ISEE-2 satellite for the interval from 1200 to 1800 UT. Regions identified in the panels are based on examinations of plasma greyscale and moments, and were arrived at independently from the magnetic field data. White indicator bars demark periods of plasma sheet, crosshatched bars indicate plasma sheet boundary layer and regions of uncertain plasma sheet determination, and the black region indicates the tail lobe. The satellite was clearly within the plasma sheet throughout much of the interval, even during periods when the magnetic field was relatively constant and not reversing.

associated with bulk tail motions and not internal, substorm related tail reconfigurations. The Z-component of the IMF was approximately zero for fourteen hours prior to the shock arrival and the AE index was small, indicating that the crossing at approximately 2:00 UT was not due to a substorm. For the crossings at about 15:15 and 15:50 UT, the IMF had been substantially northward, indicating that substantial magnetic flux was not being added to the magnetotail, for at least two and one half hours prior to each of these encounters. Such a timescale is sufficiently larger than the internal timescales of substorms (e.g., Foster et al. [1971]; Baker et al. [1981]; Bargatze et al. [1985] that these crossings are probably not substorm related. The AE index for this later interval is best described as disturbed (100-500 nT), but is apparently associated with the bulk reorientations of the tail as a whole, and not internal reconfigurations, as evidenced by a lack of classic substorm signatures in the AE index from 00:00-06:00 and 12:00-16:00 UT.

2.4.1 15:50 UT 5 April 1979

The simple sheet geometry described in the previous sections is appropriate to the crossing at ~15:50 UT. This crossing has already been used to demonstrate the techniques for removing a variable sheet normal velocity, as shown in Figure 2.3. The top panel of Figure 2.3 shows the two satellite crossing signatures in their respective field line normal coordinate systems. In this case the independently derived normals agree to within 8^{o} which indicates

that the assumption of a simple, locally planar sheet geometry is fairly good. During the period from 14:20 to 15:40 UT the IMF configuration had both positive B_X- and B_Y-components, which is in the sense opposite to the normal Parker spiral. This configuration, however, is in the appropriate sense to give the observed B_Y-component in the tail for the mapping of the IMF Y-component into the magnetotail, as has been statistically demonstrated by Fairfield [1979] and Lui [1983].

At 15:50 UT the satellites were located near the center of the magnetotail at (-17.6,-3.2, 0.2) R_E GSM (ISEE-1) with a separation vector $\underset{\sim}{S}$ = (-6826, 1241, 2732) km, GSM. The L-axes derived from minimum variance analysis are $\hat{L}_1$ = (.991, -.008, .134) and $\hat{L}_2$ = (.975, .092, .202) for ISEE-1 and 2, respectively, in GSM coordinates. The small Y-component of the L-axes is common for field lines near the center of the tail. The X- and Z-components indicate that the sheet is tilted upward toward the earth by 8^o and 12^o at the two satellites. The nominal sheet normals, N_{NOM}, for these L-axes, calculated as described previously, are $\hat{N}_{NOM1}$ = (-.134, .001, .991) and $\hat{N}_{NOM2}$ = (-.201, -.019, .979).

The current density profiles shown in Figure 2.6 have been calculated assuming these nominal sheet normals. While the absolute magnitudes of the current densities and thicknesses of the current peaks are a function of the choice of the sheet normal, the relative distribution of the features is not. The effect of choosing a different current sheet normal is to inversely vary the calculated sheet thickness and current density magnitude. Since the total

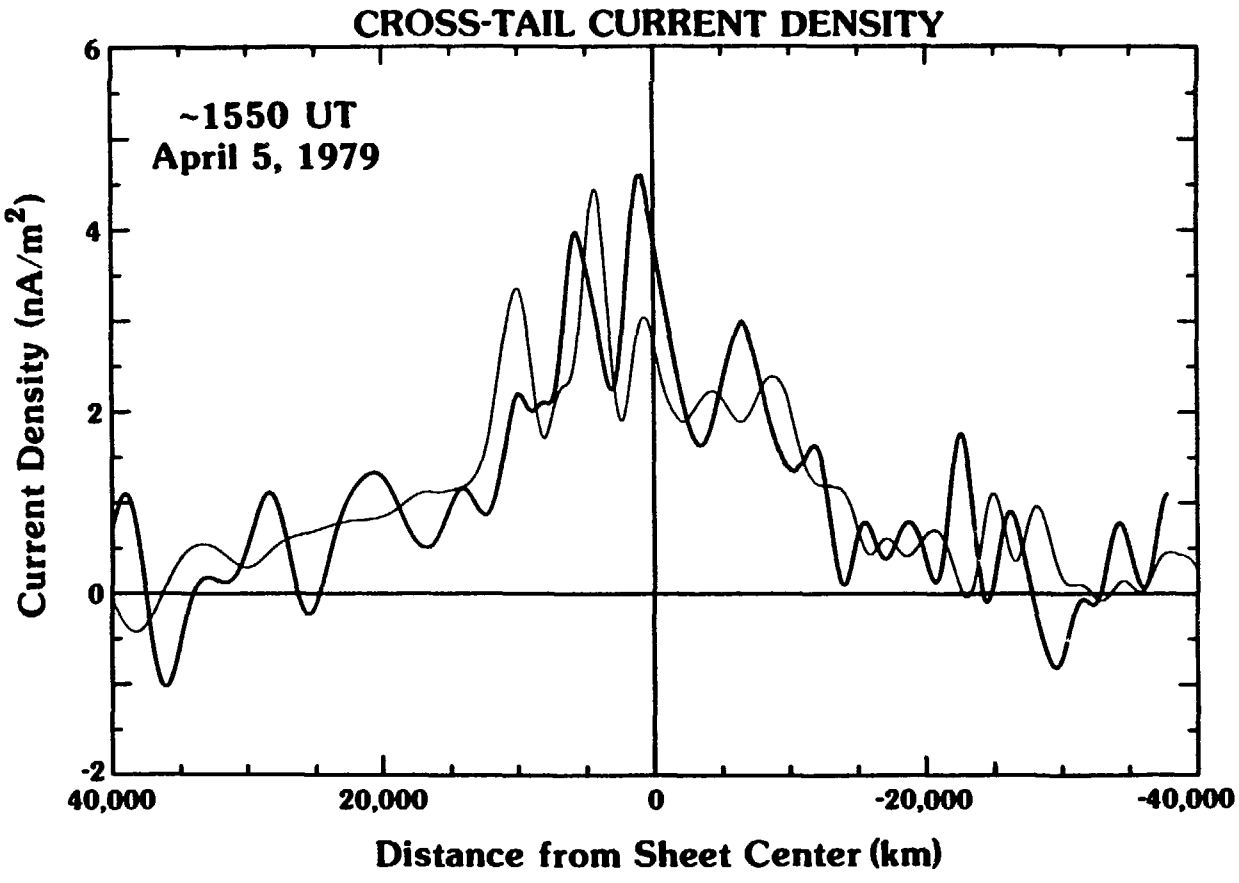

Fig. 2.6. Cross tail current density distributions for ISEE-1 and -2 displayed as a function of distance from the current sheet midplane for the crossing at ~1550 UT at -17.6,-3.2,0.2 R_EGSM. The distributions show the sheet to consist of a central current density enhancement surrounded on either side by lower density "shoulders." Further, the sheet is highly structured, the narrow density peaks being a fraction of an R_E thick, and variable.

sheet current is fixed, a thicker sheet requires proportionally smaller current densities throughout the sheet.

For this particular crossing the geometry of the two satellites is fortuitous in that the separation vector between the satellites in plane P, namely $\underset{\sim}{S}^*$, is only 22 degrees from the nominal normal. The maximum possible thickness, T_{MAX}, is therefore only 8% greater than the nominal thickness, T_{NOM}. This difference is of the order of other uncertainties in the calculation. Further, the field line normal, n, makes an angle of only 15 degrees with respect to N_{NOM}, and is toward $\underset{\sim}{S}^*$. This angle yields a thickness only 3% different from T_{NOM}, and is therefore even more negligible. Due to the unusually fortunate satellite/current sheet/field line geometry for this crossing, the calculated thickness and current density magnitudes are very likely to be correct. Of course it is possible that the sheet is thinner than derived here, but there is no physical motivation to assume that the sheet should be excessively rotated from its nominal configuration, particularly given the field line orientations.

The current density distribution shown in Figure 2.6 is comprised of two rather distinct regions. The majority of the sheet current is carried in a central structure which is approximately 25,000 km thick, and which is embedded in a larger region of somewhat smaller and more uniform current density. This broader region is approximately 70,000 km thick although the actual edges are not particularly well-defined. These thicknesses can also be described in terms of thermal ion-gyroradii. Using the asymptotic

plasma parameters yields thicknesses of ~145 and ~407 R_{ig}, and using central sheet plasma parameters yields ~60 and ~169 R_{ig} for the thin central, and broader regions, respectively. While it may be tempting to call this broad current region the plasma sheet, it must be noted that the plasma data both preceding and following this crossing indicate that at least ISEE-2 was located within the plasma sheet continuously. Not only does Figure 2.6 demonstrate that the bulk of the sheet current is carried in a central layer that is thin compared to the overall width of the plasma sheet, but it further shows a tremendous amount of small scale structure.

Fluctuations in current density are found throughout the entire current sheet, at least at the time of this crossing. Typically, the variations occur on size scales of about 5000 km (29 asymptotic or 12 central R_{ig}) for this crossing, which is consistent with, or somewhat larger than, the minimum resolvable size scale from the intersatellite timing. Since the magnetic field data were filtered to remove variations with frequencies higher than the inverse of the intersatellite timing, structures observed in these distributions cannot be accounted for by simple motions of a planar, parallel current sheet. The fact that small scale variations observed at ISEE-1 and -2 do not agree further demonstrates that the sheet cannot possess a parallel and planar structure on the size scale of the satellite separation vector. This important observation will be examined in greater detail in the Discussion section of this chapter.

Plasma data from the Los Alamos/MPE Fast Plasma Experiment

onboard ISEE-2 are shown in Figure 2.7 for the interval from 15:00-16:00 UT. During the first half of the crossing from approximately 15:43:45 to 15:48:30 (indicated by the first pair of vertical lines) the proton temperature is slightly below its presheet value while the number density is slightly above its presheet value. During the second portion of the crossing from approximately 15:48:30 to 15:53:30 these two parameters switch, with the density dropping below and the temperature rising above their original values. The total ion plasma pressure throughout this crossing is surprisingly flat, and shows only a small decline during the course of the crossing. The electron pressure (not shown), which is typically ~10% of the ion pressure, similarly shows little variation across the sheet. For an observed plasma pressure of $\sim 5 \times 10^{-9}$ Dynes/cm^2, the beta of the plasma varies from ~1 at the edges of the sheet to ~4 at the center. The variation required in the plasma pressure to achieve a condition of hydrostatic equilibrium should be resolvable in the plasma data. This condition has been examined for this crossing, and JxB and ∇p are found to be in agreement only to an order of magnitude. It therefore seems unlikely that the current sheet could be in a true state of hydrostatic equilibrium at the time of this crossing.

Also of interest is the determination of the three-dimensional plasma flow velocity vector. Figure 2.8 shows the plasma flow velocity vector components and magnitude in the GSM coordinate system. Points which show total velocities of less than about 40 km/sec are not reliably determined and should not be considered to

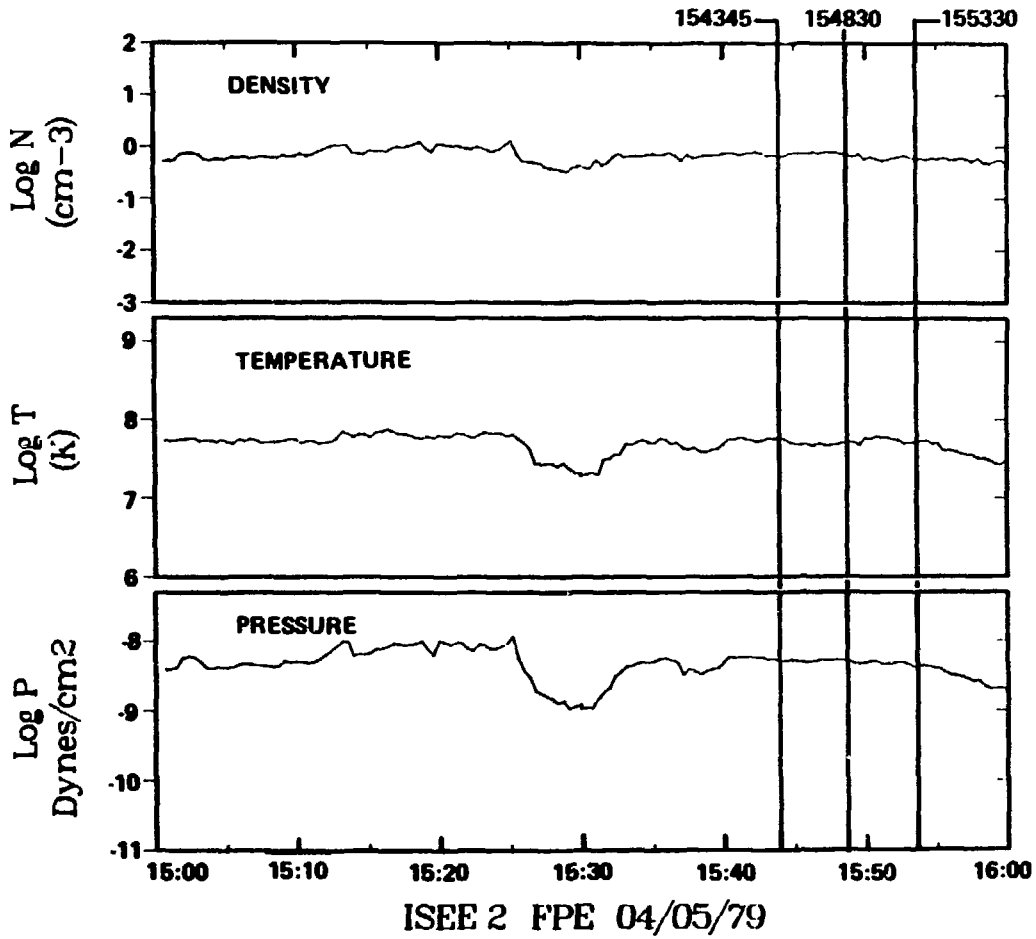

Fig. 2.7. Proton density, temperature, and pressure for the interval from 1500 to 1600 UT, at ISEE-2. The three vertical lines indicate the center of the sheet crossing and ± 40,000 km.

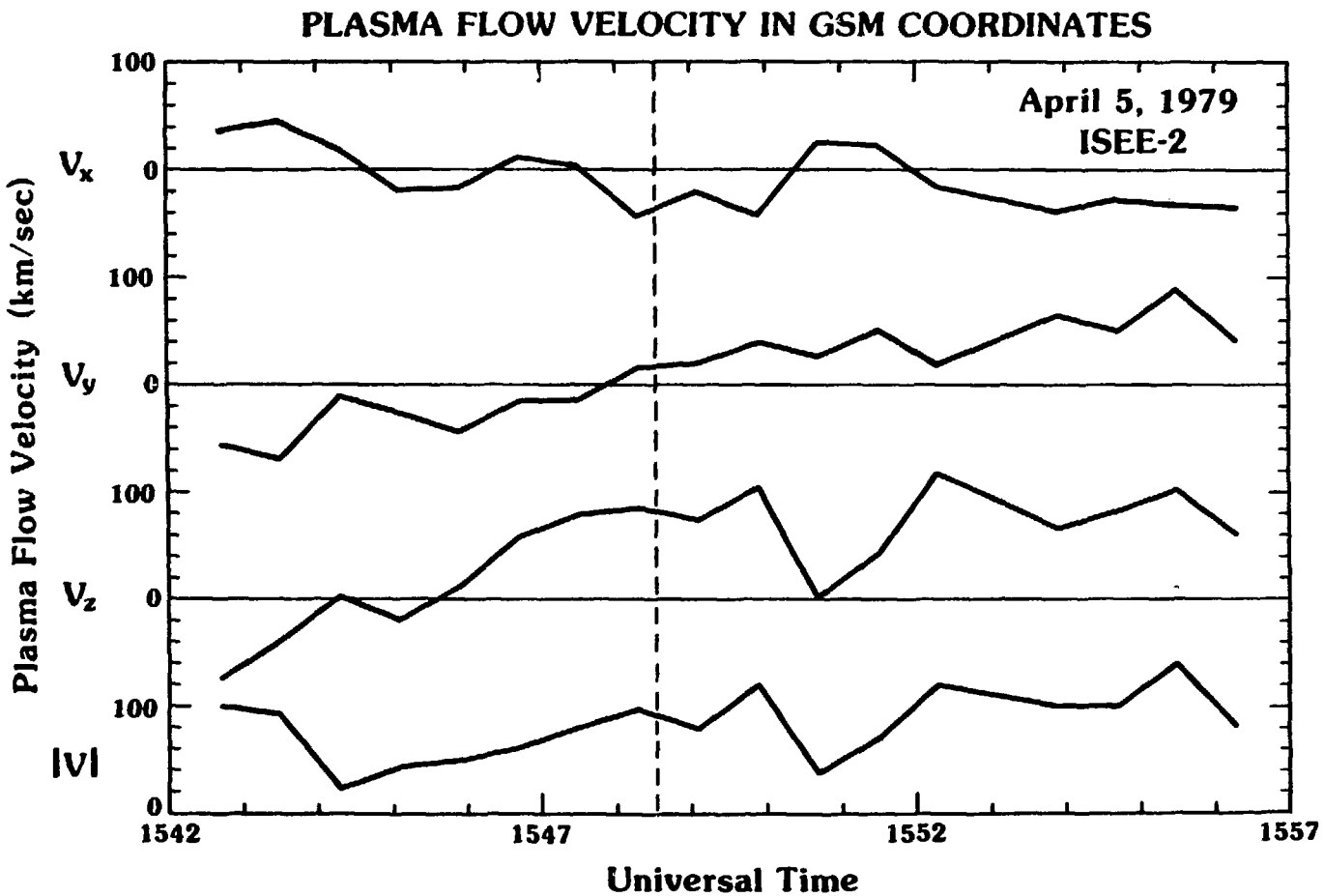

Fig. 2.8. Three dimensional plasma velocity components in GSM coordinates. Velocities at times when the magnitude is less than about 40 km/sec are not reliably determined. The predominantly upward velocity of the plasma is consistent with the derived sheet motion.

be significant. The vertical dashed line indicates the center of this sheet crossing. The Z-component of the plasma velocity is positive and relatively large throughout most of the crossing. This direction is consistent with the upward motion of the current sheet required to account for a crossing from the north (earthward field) to the south (tailward field) side of the sheet. Further, the approximate magnitude of the upward plasma motion, while not in perfect agreement with the intersatellite timing derived velocity, is also not inconsistent with it. The X- and Y-components of the plasma velocity remain generally quite small throughout the sheet crossing. While the X-component crosses back and forth between small positive and negative values, the Y-directed velocity shows a marked asymmetry between the two sides of the sheet.

Flows on the north side of the sheet appear to be predominantly from dusk to dawn while flows on the south side are entirely from dawn to dusk. The expected direction of proton motion based on ion gyromotion back and forth across the field reversed sheet is from dawn to dusk for both sides since the magnetic field X-component changes sign across the sheet midplane. Observed asymmetries in this flow are at present not well understood and could simply be due to small errors in the choice of coordinate systems. In any case, such asymmetries are not of primary interest for the purposes of this study. Plasma flow vectors are shown here principally to corroborate the intersatellite timing derived motion of the sheet.

Electric field data (supplied by C. Cattell from the ISEE-2 electric field detector) for this crossing have been examined to

determine if they are also consistent with the observed sheet motions. Since the Z-component of the electric field is not available throughout most of the crossing, due to experimental limitations, a rotation of the data from the satellite to the GSM coordinate system is not possible. The two systems, however, only differ by a rotation about their common X-axis by 20 degrees. It is therefore possible to look for at least a qualitative agreement between -vxB and the actual measured electric fields. The Y-component of the electric field is predominantly negative through the first half of the crossing, and positive through the second half, with a brief positive excursion at the start of the crossing. Since B_X is positive in the first half of the crossing, and negative in the second half, a plasma flow which starts first negative and then goes positive at about 15:45 is entirely consistent with the observed electric field Y-component, further substantiating the observed plasma and sheet velocities.

2.4.2 02:00 UT 5 April 1979

The interplanetary shock which arrived at the earth just prior to 2:00 UT on 5 April 1979 and the region of enhanced plasma pressure which followed it have already been discussed. The initial tail current sheet crossing at about 2:00 is almost surely a direct consequence of the initial impact of the interplanetary shock as it occurs at ISEE-1, about 22 R_E back in the tail, less than 10 minutes after the passage of the shock at IMP-8 (-2,22,27) R_E GSM. The approximate shock normal derived from the magnetic coplanarity

theorem is (-.69, .42, .59) and the velocity increases across the shock by >100 km/s at ISEE-3. This yields an expected initial upward motion of the magnetotail. The crossing at the ISEE satellites is from the north to the south side of the sheet as would be expected for an upward tail motion. This case represents a geomagnetically moderate sheet crossing since the IMF B_Z-component was approximately zero for fourteen hours prior to the shock, and the AE index was less than 300 nT and relatively smooth during the twelve preceding hours.

Figure 2.9 displays the magnetic field data, calculated normal velocity, and current density distribution for this crossing which occurred at -22.0, -1.4, 4.0 R_E GSM (ISEE-1). The calculations used to obtain the values shown in the lower two panels assume the nominal normal as was done previously. In this case these normals are $\hat{N}_{NOM1}$ = (.217, .052, .975) and $\hat{N}_{NOM2}$ = (.197, .061, .979) and agree to within 4.4°, indicating the appropriateness of the assumption of a flat current sheet on the intersatellite separation size scale. The top panel shows the original magnetic field data in the GSM coordinate system. The dashed vertical lines show which portions of the data correspond to the central region of enhanced current density in the bottom panel. This mapping is indicated for both ISEE-1 and ISEE-2 with the set of four lines, and further emphasizes that locations in the sheet correspond to very different times at the two satellites.

It is interesting to note the marked asymmetry in the magnetic field profiles. While the variation of the X-component of the field

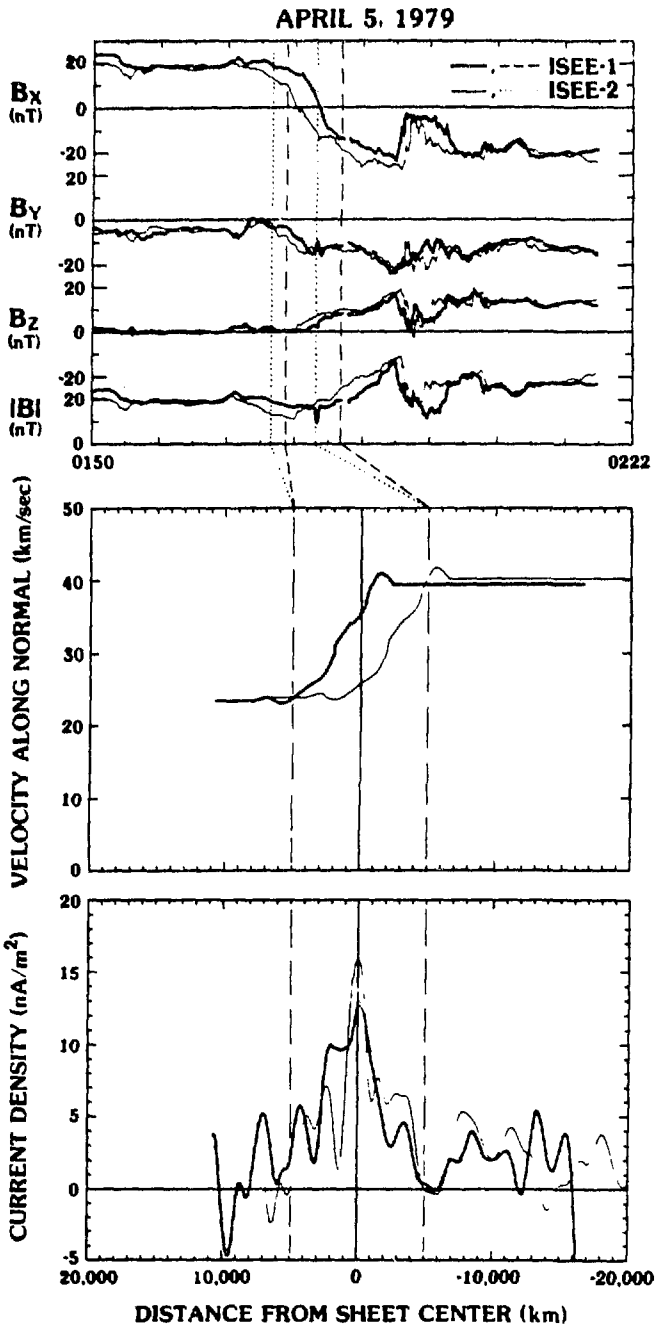

Fig. 2.9. Magnetic field, sheet normal velocities, and current density distributions for the sheet crossing, at -22.0,-1.4,4.0 R_EGSM, associated with the initial arrival of the interplanetary shock at ~ 0200 UT. The central current density enhancement is indicated by the dashed vertical lines in the bottom two panels, and mapped up to the appropriate portions of the magnetic signatures for the two satellites independently.

is reasonably symmetric, the Y-component decreases and the Z-component increases, both rather uniformly through the crossing. In the coordinate systems used in this study, all these variations end up in the B_L-component, and the current is driven parallel to the M-axis. The net effect is that the total field strength decreases very little through the first half of the crossing, and increases very rapidly through the second half. These profiles indicate that the magnetic pressure in the tail is increasing during the period of crossing as would be expected if the tail is being compressed by the arrival of the shock. While this variation technically contradicts the stated assumption of a sheet which is not varying on the timescale of the crossing, it is still possible to analyze this crossing by assuming that the sheet does not vary much on the intersatellite timing timescale, and that the principal effect of the pressure increase is simply to compress the sheet isotropically.

The middle panel of Figure 2.9 shows the normal velocity for this case and was derived from filtered, rotated data, just as in the previous example. The sheet normal was again chosen to be the nominal normal given the derived L-axis orientation; however, the normal velocity values derived are appreciably slower than before. In the lower panel, the calculated current density is displayed. The thickness of the central enhanced region is about 10,000 km (35 asymptotic or 15 central R_{ig}), and the peak current density is in excess of 15 nA/m^2 at ISEE-2. Both the satellite signatures show a narrow central current density peak surrounded on either side by somewhat smaller current density "shoulders" in the distribution.

The regions outside of about ±5,000 km show a net positive current density with an appreciably smaller average value than the central structure. While it is not possible to identify these regions unambiguously with the broad, low current density regions observed in the first case study, the obvious similarities at least make such an identification plausible.

An interesting major difference between this case and the previous one is that the field lines in this current sheet have a large cross tail component. The planes which contain the field line rotations are in fact inclined by 74° and 71° from the ISEE-1 and -2 most nominal normals respectively. Magnetic field lines in this sheet crossing are therefore strongly directed in the cross tail sense. The IMF direction prior to the arrival of the shock is in the normal spiral direction for an in-pointing sector, and the strong cross tail component of the field in the sheet is from dusk to dawn, as would be expected if a portion of the Y-component IMF was mapped into the tail. Geometries for the current sheet structures which are consistent with the observation of such a large field line inclination include a relatively nominal sheet orientation with highly inclined field lines in it, a sheet which is locally very wavy with reasonably perpendicular field line orientations inside, or some intermediate configuration between these. It is extremely unlikely that the entire current sheet could be rotated by some 70° this close to the earth; however, it is possible that the sheet could be very wavy or lumpy and therefore could have sections which have locally inclined normals of 70° or

more. If the field lines are actually normal to the sheet surface, as in the wavy current sheet picture suggested here, then the current density distribution and sheet normal velocity shown in Figure 2.9 would have to be rescaled. The central current sheet structure thickness would drop from about 10,000 km to 4,000 km and the peak ISEE-2 current density would rise to over 35 nA/m^2. Such a current density is not unreasonable, and the questions of the actual sheet orientation and maximum current densities will be examined in greater detail in Section 2.5.

The satellite separation vector for this crossing is (-573, 1503, 2389) km in GSM coordinates. The component of this vector in the plane normal to the L-axis, $\underset{\sim}{S}^* = (76, 1656, 2220)$ km. The scaling factor for the sheet maximum thickness and minimum current density is therefore only 1.2. This means that the greatest thickness that the nominally 10,000 km thick central structure could be is about 12,000 km (42 asymptotic or 18 central R_{ig}), and the peak ISEE-2 current density must exceed 12 nA/m^2. As before, this case represents a somewhat fortunate satellite orientation in that the firm upper bound on the sheet thickness is quite close to the nominally derived value.

Three-dimensional plasma data for this interval indicates that the proton temperature, and to a lesser extent the number density, rises during the first half of the crossing and falls during the second half. This yields a plasma pressure profile in good qualitative agreement with the field diamagnetic reduction and a hydrostatic equilibrium condition. The plasma pressure on the south

(exit) side of the sheet is ~2.5 × 10^{-9} NT/m^2, which is about a factor of two higher than on the north (entry) side. This variation is consistent with an increase in the pressure inside the tail during the course of the crossing as was indicated in the previous discussion of the top panel. The plasma flow direction observed through the crossing is predominantly earthward and the bulk speed is quite high, ranging up to about 360 km/sec during the second half of the crossing. Throughout much of the crossing the plasma flow vector points downward, in the opposite sense to achieve the observed north to south traversal. The magnitude of v_Z, however, is smaller than v_X typically by a factor of about four. Since the current sheet is inclined with the normal having a negative X-component, earthward motion of the sheet would be expected to carry the satellites from the north to the south. Further, errors in the three-dimensional velocities on the order of 30% are not unreasonable. The plasma flow data, therefore, cannot be considered to be inconsistent with the other observations of the crossing. Such large plasma flow velocities are not expected in the cross tail current sheet at geomagnetically quiet times, and argue that this crossing occurs during a more active interval.

2.4.3 15:15 UT 5 April 1979

The last 5 April 1979 crossing studied here occurred at about 15:15 UT at -17.9, -3.1, 0.4 R_E GSM (ISEE-1). The crossing carried the satellites from the northern to the southern side of the sheet as shown in the top panel of Figure 2.10. It is clear from the

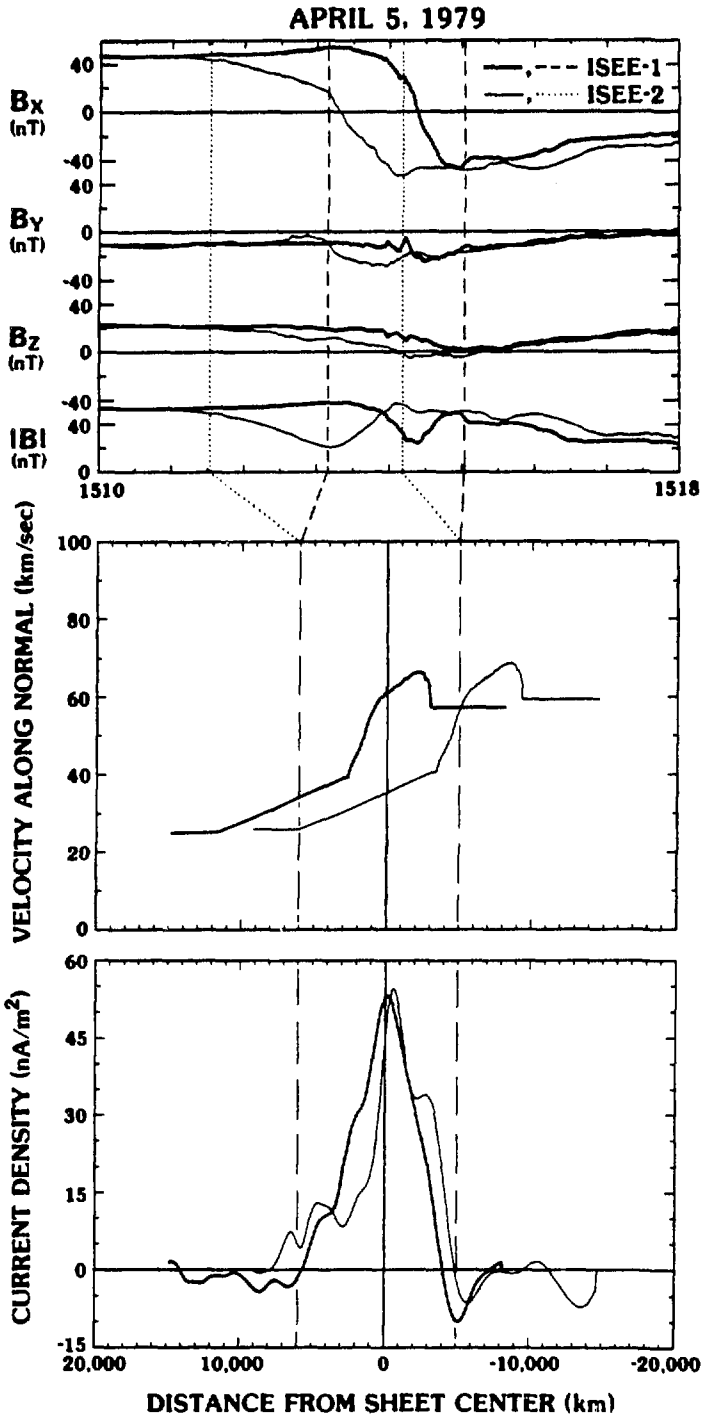

Fig. 2.10. Data for another crossing at 1515 UT and at -17.9,-3.1, 0.4 R_EGSM, in the same format as in the previous Figure. Note that the observed current densities are much greater than for the previous cases (see text).

field data that the sheet normal velocity increases with time across the sheet, since the duration of the sheet entry is much greater than the duration of the sheet exit. This observation is borne out quantitatively in the middle panel of Figure 2.10 which shows the actual sheet normal velocity. Both of the bottom two panels are based on the nominal normal sheet coordinates, as were the previous cases. Sheet normals derived independently for the two satellite data sets agree to within 5.2^{o}, again indicating a locally flat sheet topology.

The bottom panel of this figure displays the calculated current sheet current densities as a function of location in the sheet, under the assumption of the nominal normal, as for the previous examples. Again, a relatively narrow current density peak is observed in the center of the sheet. The thickness of this structure is approximately 10,000 km (78 asymptotic or 27 central R_{ig}), and the peak current density is over 50 nA/m^2. This value is appreciably larger than those measured for the previous two examples, but the full sheet thickness is also narrower than previously observed. For this case, unlike the previous examples, no regions of somewhat smaller current density are observed at the edges of the strong central structure.

Field line derived axes yield normals, which are rotated from the nominal normals, (-.152, -.018, .988) and (-.178, -.038, .983), to directions of (.019, -.845, .535) and (.079, -.877, .471), or through angles of 57^{o} and 61^{o} for ISEE-1 and -2, respectively. The B_Y-component of the field is small, but in a sense inconsistent with

the expected sense of the IMF at the time of this crossing. This might be accounted for, however, by the fact that the IMF B_Y had changed direction just one hour prior to this crossing and the timescales for reversing the sense of ionospheric rotation and tail B_Y could be of this order. Calculations based on the assumption that the field rotates in a plane normal to the sheet surface give the unbelievable results of a sheet thickness of only 440 km, and maximum current density of 1200 nA/m^2. It therefore seems likely that the planes containing the magnetic field line rotations in the sheet are substantially inclined with respect to the sheet normal itself. Calculation of the maximum sheet thickness based on the orientation of the separation vector in the sheet, S^*, yields a thickness which is only 20% larger than that derived for the nominal normal. The firm upper bound on the current sheet thickness for this case is therefore only 12,000 km (94 asymptotic or 32 central R_{ig}).

Plasma data for this crossing, also shown in Figure 2.7, indicate the qualitatively expected increase in plasma pressure for hydrostatic equilibrium. It is not possible to examine this equilibrium in detail since the entire crossing took only about 2-3 minutes, which gives only a few plasma spectra. Plasma flow vectors, while also inconclusive due to the very short crossing duration, show that the flow in the sheet is principally dawn to dusk with only small possible earthward and upward components. Such a flow is consistent with the slow crossing speeds displayed in

Figure 2.10 and with the north to south nature of the crossing, since the errors in measuring very slow flows are large.

2.5. Discussion and Summary

Three current sheet crossings associated with the region of varying solar wind pressure behind an interplanetary shock on 5 April 1979 have been studied in detail. One of the three is apparently associated with the initial shock arrival, while the other two occur much later in the day. The effect of the initial shock and associated region of varying solar wind pressure behind it is to compress and deflect the magnetotail. As a consequence, the ISEE-1 and -2 satellites, which were orbiting near the midplane of the magnetotail, repeatedly encountered the cross tail current sheet. The crossings studied here, while not representative of the configuration of the quiescent current sheet, do correspond to relatively quick and analyzable crossings that are probably not principally due to substorms and the major internal magnetotail reconfigurations associated with them. The current sheet crossings studied here, while best described as occurring during a disturbed period, are probably as close to the quiet tail configuration as are any crossings which are feasible to analyze, even with our technique.

Throughout most of the 19 hour post-interplanetary shock period, the ISEE-2 satellite was engulfed in the magnetotail plasma sheet as evidenced by plasma sheet greyscale and plasma parameters. During this period the ISEE satellites made repeated encounters with

the current sheet. These encounters, however, were separated by relatively long periods when the satellites were apparently not in regions of substantially enhanced current density, since $\underline{B}$ was relatively constant. This observation is consistent with the usual theory of the near earth magnetotail which defines the plasma sheet as the region of enhanced plasma density associated with the particle populations trapped on closed field lines. The current sheet, however, is defined by the major rotation of the magnetic field between roughly sunward and antisunward, and the associated cross tail currents. The current sheet topologically must lie inside the plasma sheet since the current sheet in the near tail is associated with the curl of closed field lines, but the region of substantial current density need not fill the plasma sheet region, and may be simply embedded in it. This possible difference between an intrinsic magnetotail's current and plasma sheets is in contrast to the structures of intrinsic magnetotails downstream from an X-line, and induced magnetotails, neither of which have regions of closed field lines to trap particle populations.

While a clear difference between current and plasma sheet definitions has been delineated in the near magnetotail region, it should not be concluded that no cross tail current is present in the plasma sheet region outside the central current sheet. It seems likely that the entire plasma sheet region carries some current, while the central current sheet is simply the enhanced region which carries the bulk of the current.

The general current sheet geometry has been examined and the

inherent difficulties of resolving a three-dimensional structure with data from only two satellites have been discussed. Magnetic field rotations through the sheet were seen to occur in planes which were inclined with respect to the nominal sheet configurations. The simplifications possible because of the well-defined nature of this maximum variance axis and assumption of planarity, greatly reduce the ambiguity of the geometry so that the sheet geometry is fully resolved to within one missing piece of information. This missing information is an angle between the projections of any of the known vectors into the plane perpendicular to the L-axis, and the actual sheet normal vector. Without knowledge of this angle it is only possible to set upper bounds on the sheet thicknesses based on the chance orientation of the satellite separation vector, and speculate as to the actual sheet orientation.

In this study, data has been displayed in the nominal normal coordinate system in each case. This normal is along Z_{GSM} if the L-axis coincides with GSM X. Small deviations of L from GSM X are due to small deflections in the tail position and the internal flaring of field lines away from the dipole field. The fact that local nominal normals independently derived at the two satellite agree to within 8^{o}, 5^{o}, and 6^{o}, respectively for the three cases, indicates that the current sheet topologies are quite flat, at least in X, on the separation size scale of a few thousands of kilometers. It is unlikely that current sheet waviness could account for local inclinations in the sheet of 70^{o} or 60^{o} as indicated by assuming the field lines are perpendicular to the sheet surface in the second and

third cases. The radius of curvature of such structures, given that the sheet is flat to within about 5^{o} over a couple thousand kilometers in both cases, would have to be 3 to 4 R_E. Such large scale waviness of the plasma sheet surface at substorm times has been reported previously by Forbes et al. [1982]; however, the observed waves were all of small amplitude (600-1400) km over wavelengths of 1-5 R_E. Observed tilts at the reported crossing locations were less than 20^{o}, and the very large tilts required to explain the observations in this study seem very unlikely. Furthermore, the cases studied here do not occur at strongly geomagnetically active times when such large amplitude perturbations are probably somewhat more likely. A far more likely situation is that the sheet is approximately in its more nominal configuration and the field lines within it are simply highly inclined. Two of the three cases studied here exhibit large ($\gtrsim 60^{o}$) field line inclination angles from the most nominal sheet normals. While this is certainly not a statistically significant number of cases, we can at least speculate that such large angles may not be uncommon in the cross tail current sheet.

One possible explanation for these large inclinations has been described by Moses et al. [1985]. They suggest that oppositely rotating convection patterns of the open field lines in the two polar caps can cause motions of the closed (plasma sheet) field lines which are in the sense to shear the sheet, and create large cross tail magnetic field components in the plasma sheet. For the first two cases described here, the IMF B_Y-component was in the

appropriate sense for this effect to have caused the observed Y-component of the field in the plasma sheet. The third crossing occurred just 45 minutes after the IMF had completed a 5.5 hour excursion with a peak B_Y field >30 nT, in the appropriate sense for the observed Y field in the plasma sheet. None of the crossings studied here are inconsistent with the Moses et al. model if the timescale for changes of the Y field component in the plasma sheet is $\gtrsim$ 1 hour. In any case, the derived upper bounds of 27,000 km and 12,000 km for the central structures in the first two cases, and 12,000 km total for the last, firmly fix the maximum sheet thickness for these cases. While the set of three crossings studied here in no way constitutes a statistically significant set, it is interesting to note that the two thinner, higher current density crossings are associated with the sheets which have large field line inclinations.

Magnetometer and plasma analyzer data have been used together throughout this study to aid in the examination of the current sheet structure, and a number of points of contact have been made between these data. Three dimensional plasma flow velocities indicate that plasma motions observed in the sheet are consistent with sheet velocities derived from intersatellite timing under the nominal normal assumption. This observation indicates that actual sheet normals are probably similar to the nominal ones derived here. Inverse variations were found to exist between the magnetic and plasma pressures across the diamagnetically reduced current sheet in two of the three cases. Further, in the ~02:00 UT case, the

pressure in the tail as a whole increased during the crossing, and the expected pressure variation was observed within the sheet as well as without, indicating that, at least in this case, a rough state of pressure balance existed throughout the current sheet just as was shown for the plasma sheet by Fairfield et al. [1981]. Variations from hydrostatic equilibrium cannot represent the stable, steady state configuration of the sheet. Rather, they probably correspond to times when the tail orientation is adjusting to variations in the external solar wind pressure.

Two of the three crossings examined here showed similar structure: a large current density feature in the center of the sheet and smaller "shoulders" in the current density distribution on one or both sides. In the third case, the data does not extend sufficiently far out to the sides to be sure whether shoulders exist or not. Since the calculation and removal of the variable velocity effect is only possible in the central portions of the sheets, and is simply extrapolated out from there, a lack of observed shoulders may simply indicate that current densities in the outer current sheet are not reliably determined. If the large central current structure is always surrounded by lower density shoulders, then this would be indicative of a current distribution which is described by a single function with a rather sharp cutoff. Such a sheet distribution would be consistent with a model which describes the field line rotation by a function which drops to low, but nonzero values away from the central current sheet. One such function for B_L is the hyperbolic sine, while the planes of the field lines are

inclined in the sheet so that both of the nonreversing field components have constant, nonzero values. In this case the cross tail current would be positive and slightly decreasing all the way out from the near shoulder regions to the edges of the plasma sheet.

An important result of this study is that, while the gross structure of the current density distribution is shown to consist of two relatively distinct regions, a substantial amount of fine structure is also shown to be present in the current density distributions. These structures are typically 2-6 $\times$ 10^3 km thick, which corresponds to tens of ion gyroradii, and are resolved in the data since it has been filtered to remove all variations on timescales shorter than the intersatellite timing timescale. The observed structures could represent compressional waves in the plasma sheet, real current filaments, or breakdowns in the assumption of a plane parallel geometry which would again indicate spatial current structures. Structures observed in one satellite's current distribution are usually mirrored in the other's distribution although shifted in magnitude, and sometimes slightly in location. Such a correlation is consistent with a model in which the current sheet is comprised of numerous elements of enhanced current density, or possibly current driven instabilities. Although larger than would normally be expected, filamentary structures might be due to kinetic ion effects and single particle type motions.

2.6 Chapter Acknowledgments

The authors gratefully acknowledge valuable discussions with J. Birn, J. T. Gosling, G. L. Siscoe, H. E. Spence, and G.-H. Voigt, and sincerely thank Phillip Lee for helping in the development of the variable velocity computer program which made this study possible. Much appreciated electric field data examined for one of the crossings was supplied by C. Cattell and the UCB instrument team. Magnetic field data from ISEE-3 and IMP-8 were obtained from the NSSDC through J. King. We thank the instrument teams at JPL and GSFC for providing these data. This work was principally carried out under the auspices of the Institute of Geophysics and Planetary Physics, UCLA and supported under NASA contract NAS-5-28448. The principal author was supported by Los Alamos National Laboratory under the auspices of the United States Department of Energy as a part of the Advanced Study Program, while research done at Los Alamos was supported under NASA contract S-04039. Finally, the authors wish to thank the referees, who supplied valuable suggestions for improving this chapter.

CHAPTER 3

The Average Magnetic Field Draping and Consistent Plasma Properties of the Venus Magnetotail

3.0 Chapter Overview

A new technique has been developed to determine the average structure of the Venus magnetotail (in the range from -8 R_V to -12 R_V) from the Pioneer Venus magnetometer observations. The spacecraft position with respect to the cross tail current sheet is determined from an observed relationship between the field draping angle and the magnitude of the field referenced to its value in the nearby magnetosheath. This allows us to statistically remove the effects of tail flapping and variability of draping for the first time, and thus to map the average field configuration in the Venus tail. From this average configuration we calculate the cross tail current density distribution and $\underset{\sim}{J}\times\underset{\sim}{B}$ forces. Continuity of the tangential electric field is utilized to determine the average variations of the X-directed velocity which is shown to vary from -250 km/sec at -8 R_V to -470 km/sec at -12 R_V. From the calculated $\underset{\sim}{J}\times\underset{\sim}{B}$ forces, plasma velocity, and MHD momentum equation the approximate plasma acceleration, density, and temperature in the Venus tail are determined. The derived ion density is approximately $\sim.07$ p^+/cm^3 ($.005$ O^+/cm^3) in the lobes and $\sim.9$ p^+/cm^3 ($.06$ O^+/cm^3) in the current sheet, while the derived approximate average plasma

temperature for the tail is $\sim 6 \times 10^6$K for a Hydrogen plasma or $\sim 9 \times 10^7$K for an Oxygen plasma. Finally, the calculated plasma flow speed and density are combined to yield an upper bound on the flux of planetary ions down the Venus magnetotail, and give a value of $\sim 1 \times 10^{26}$ amu/s ($\sim 6 \times 10^{24}$ O^+/s).

3.1 Introduction

Extensive in situ observations of the magnetic field and plasma populations in the Venus environs have a shown that 1) Venus does not have a significant intrinsic magnetic field [Russell et al., 1980a] and 2) a magnetotail is a regular feature of the region antisunward of the planet (Russell [1976]; Dolginov et al. [1978]; Russell et al. [1981], [1985]; Intriligator and Scarf [1984]; Slavin et al. [1984]; Saunders and Russell [1986]). The Venus magnetotail is generally believed to form by magnetic field draping about the Venus ionosphere in a manner first suggested to explain comet tails by Alfvén [1957].

A steady state configuration of this interaction is shown schematically in Figure 3.1. The solar wind, with the embedded interplanetary magnetic field (IMF), flows radially outward from the rotating sun, causing the well-known Parker spiral pattern of the IMF. The solar wind carries the IMF flux through Venus' bow shock and mass loading, extended, neutral exosphere, and then past the generally unmagnetized but conducting ionosphere. Little, if any, of the upstream plasma flow enters Venus ionosphere. Rather, the flow is slowed, compressed, and deflected above the dayside

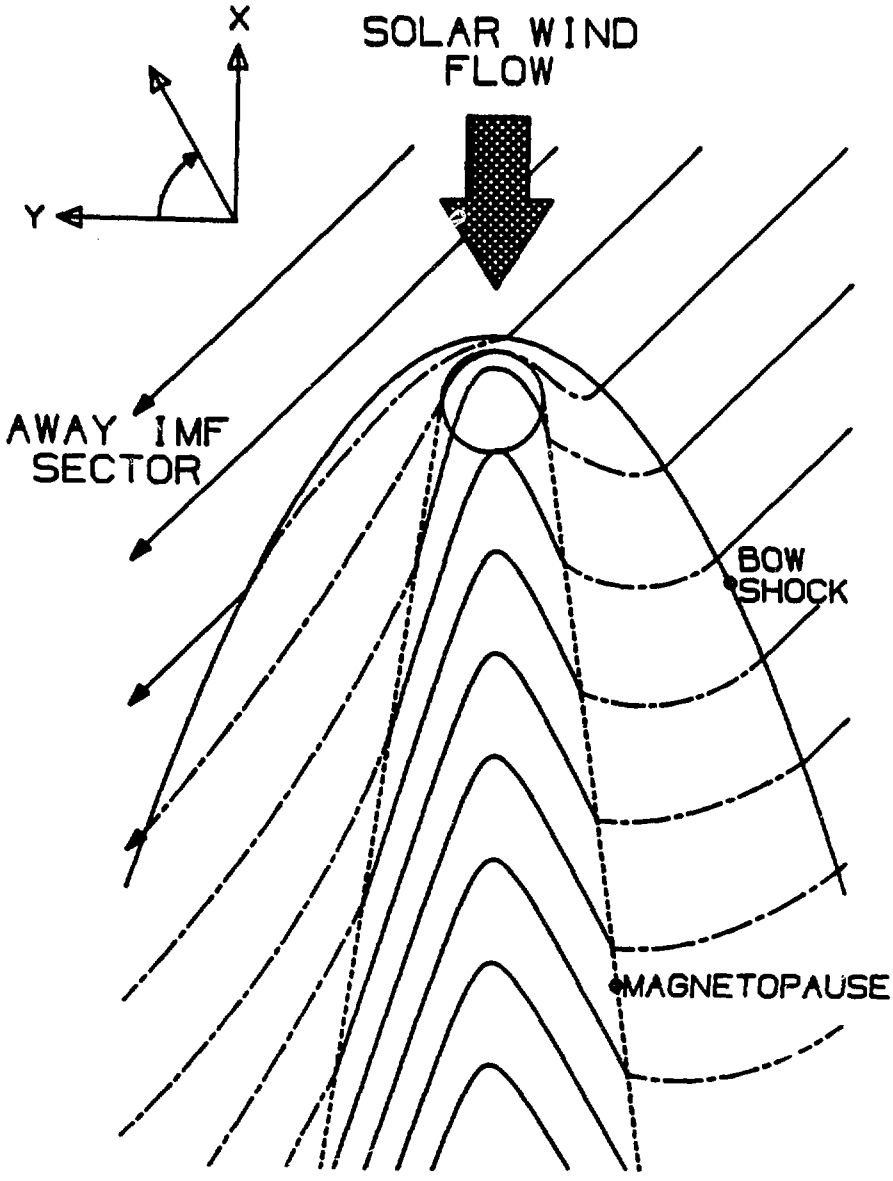

Fig. 3.1. Schematic diagram of the postulated solar wind interaction with Venus in the plane containing the upstream IMF. The upstream solar wind carries the IMF through the bow shock and magnetosheath. At the obstacle the magnetic field must flow perpendicular to this plane, and around the conductive ionosphere. This diversion of the flow, enhanced by mass loading of the flow near to the obstacle, causes the field lines to drape and form a magnetotail. Note also that the spiral orientation of the upstream magnetic field causes the magnetic flux in the left lobe to be greater than in the right at every distance down tail. This has important dynamical implications for the actual tail configuration (see text).

ionopause, and eventually slips around the planet. The plasma in the magnetosheath to the sides of the Venus obstacle and magnetotail regions travels at the larger velocity of the magnetosheath flow, which is a function of position behind the shock. Since the magnetic field lines link the magnetosheath and near Venus regions, the lines become bent. This has the effect of draping the field lines such that they are "hung up" on Venus and stretched out generally sunward and antisunward to the sides of the Venus magnetotail.

In addition to deflection of the flow by the conductive ionosphere viscous slowing of the flow by the ionosphere, and mass loading of the magnetosheath plasma with material from the extended Venus atmosphere and ionosphere also contribute to Venus magnetotail formation. The mass loaded plasma flow slows in order to conserve momentum, which significantly enhances the draping of field lines around the conducting ionosphere and substantially helps to produce the Venus magnetotail. Eventually, somewhere very far downstream, we expect that the field lines should once again assume their interplanetary configuration due to the Maxwell stresses in the draped magnetic field configuration. These stresses should cause the kinked portions of the field lines to accelerate back up to, and beyond, the solar wind speed while mass loaded material tends to diffuse along the field lines due to its parallel plasma temperature.

There is now much direct and indirect evidence for mass loading of the Venus magnetosheath by the pick-up of newly created ions and

other processes such as charge exchange. Oxygen ions have been seen in the near terminator region of the Venus magnetosheath [Mihalov and Barnes, 1981] and occasionally in the distant magnetosheath and magnetotail region [Mihalov and Barnes, 1982]. An enhancement of the magnetosheath magnetic field strength has been found in the hemisphere where most ion mass pick-up is expected, presumably due to a decrease of the magnetosheath flow speed and the consequent pile-up of the plasma density and magnetic field [Luhmann et al., 1985]. Other indirect evidence is that the position of the bow shock at the Venus terminator has been found to depend on solar activity. When the solar EUV flux is high it appears that more mass is being added to the shocked solar wind, forcing the bow shock to recede from the planet [Alexander and Russell, 1985].

An interesting asymmetry between the two draped lobes is observed in Figure 3.1. If this schematic is correct, the X-component of the IMF has an important impact on the internal magnetic configuration of the Venus magnetotail. As a consequence of the larger magnetic flux content of the tailward pointing lobe at all distances down the tail, the current sheet should be displaced to the right in an equilibrium configuration. As the IMF spiral angle (in the X-Y plane) rotates, the current sheet should tend to flap from side to side within the tail in order to try to maintain an equilibrium condition. In this study we choose a coordinate system which preserves any asymmetries between the lobes, and examine the importance of this effect in the morphology of the Venus magnetotail.

The purpose of this paper is to examine the detailed average draping pattern of the magnetic field in the deep (-8 to -12 R_V) Venus magnetotail. A detailed mapping of the average configuration of this region is made possible for the first time by a new technique. This technique removes the ambiguity of the spacecraft location with respect to the tail structures by utilizing an observed relationship between the magnetic field angle and the field magnitude referenced to the immediately adjacent magnetosheath value, or diamagnetic reduction. A statistical study of the field variations with respect to the internal tail structure is thereby made possible, and the average plasma properties consistent with these variations are derived.

We will describe this study in sections. Section 3.2, "The Average Venus Tail in Magnetic Coordinates," examines the variability of the data ordered by spatial location and lays the groundwork for developing a coordinate system which measures locations with respect to the tail structures themselves. "The Average Tail Configuration with the Effects of Flapping Removed," 3.3, shows how we reconstruct the structure of the tail in the presence of flapping and examines the average variations in the field components, culminating in the average field vectors, cross tail current density distribution, and $\underset{\sim}{J}\times\underset{\sim}{B}$ forces as functions of location across the tail. In Section 3.4, "Inferred Plasma Properties," we derive the average downtail velocity as a function of distance and define a simple model based on the field variations from which the average plasma acceleration as a function of

distance, density, and temperature are obtained. Finally, Section 3.5 reviews most salient steps and results of our analysis.

3.2 The Average Venus Tail in Magnetic Coordinates

The data set used in this study is a large subset of the data set chosen by Saunders and Russell [1986]. It consists of magnetic field data from the Pioneer Venus Orbiter (PVO) magnetometer [Russell et al., 1980b], and contains the magnetotail portions of 38 orbits which were selected from the first ten seasons of data (6/79-5/84). In all, 9423 one-minute averaged magnetic field measurements are used. The criteria used to identify magnetotail portions of the data are variations in field strength and orientation, and changes in the spectrum of field variations; they are described in greater detail, with examples, by Saunders and Russell [1986]. While the identification of these regions is not perfect, it is correct for the vast majority of the data, and the mixing in of small portions of magnetosheath data will not substantially affect the statistical results described here.

The coordinate system used in this section of our study will be called the B-v coordinate system. The term B-v is used to indicate that the orientation of the coordinate system is determined by the average upstream magnetic field and solar wind flow directions. In the B-v coordinate system the solar wind flows parallel to the -X-direction, and the magnetic field component perpendicular to the solar wind flow lies along the +Y-direction. The B-v coordinate system is derived from the aberrated VSO coordinate system,

described by Saunders and Russell [1986]. The VSO coordinate system is similar to the GSE coordinate system, except that it is centered on Venus and its pole is parallel to the Venus orbital pole. The VSO X- and Y-axes are then rotated by 5^{o} about the Z-axis to remove the average aberration of the solar wind flow due to Venus' orbital motion.

In order to convert from an aberrated VSO coordinate system to a magnetic field ordered system we have two choices. The standard choice would be to rotate about the solar wind direction so that the magnetic field projected on the Y-Z plane always pointed in the same direction, e.g., +Y (Bieber and Stone [1979]; Saunders and Russell [1986]). There is a difficulty with this method, however, for if there is an asymmetry between the two lobes in the tail, as discussed previously, this method would average out the difference by combining instances of each type of lobe on both the ± Y sides of the tail. The alternative choice is to assume that the sector polarity of the magnetic field is inconsequential to the draping of the field, and change the sense of each field line so that it corresponds to a magnetic field line pointing away from the sun. This gives a coordinate system where the field is always rotated by less than $\pm 90^{o}$ to project along the +Y-direction. This choice permits the separation of "east-west" asymmetries in which the two lobes, parallel and antiparallel to the IMF, are different. However, it does not allow the detection of north-south differences as might occur, for example, if mass loading is asymmetric as predicted by Cloutier et al. [1974], [1976], and as is suggested by

the findings of Saunders and Russell [1986] and Slavin et al. [1985]. There is no choice of coordinate system that will allow us to determine simultaneously both "east-west" and "north-south" asymmetries while combining data obtained in different solar wind sectors, since the interaction is inherently three-dimensional. However, in order to increase our statistical accuracy we wish to combine such data. As will become evident in this study, the east-west asymmetry will be very important and, therefore, we choose to convert the IMF polarities prior to rotating about the solar wind flow.

The IMF is highly variable and when the Pioneer Venus spacecraft is probing the Venus tail it spends little time in the solar wind. When available, any solar wind observations are far removed in time from the periods of the tail observations. Ideally, it would be desirable to have a measure of the IMF direction when Pioneer Venus is within the tail. Saunders and Russell [1986] have established that the cross tail or Y-component is everywhere, on average, parallel to the component of the upstream IMF that is perpendicular to the flow. This is what is expected if there is little reconnection of the field between the two tail lobes. Given these results we can use the direction of the cross tail component measured on each crossing through the tail to rotate into the desired B-v coordinate system. During each tail crossing, the component of the field in the plane perpendicular to X is measured, and its average direction is used to rotate the coordinate system

for the entire crossing so that the average field projection lies along the B-v +Y-direction.

Figure 3.2 shows the orbital coverage of our data set projected on to the Y-Z plane of the the B-v coordinate system. All data have been accepted in the full width of observation in the cross-flow, Y, direction; however, the data set has been truncated in the Z-direction at ± 1.6 Venus radii (R_V). This truncation ensures that the draping, which is expected to occur somewhat differently as a function of Z in the tail, due to the variation in the tail width with Z, does not mix together the draping patterns from very different portions of the tail. By choosing only the central portion where the tail width is fairly constant, and over which draping can be expected to be fairly similar, and then by compressing this data set into the two-dimensional X-Y plane, we maximize the statistical accuracy of our derivation of the two-dimensional draping pattern in the tail. Further, our choice of coordinate system has mixed together "north-south" asymmetries so that our analysis has already suppressed the vertical gradients in the tail.

Small sections of orbits observed in this figure correspond to portions of the time when the orbit, although continuous in real space, is not continuous in the effective space of the B-v coordinate system. These correspond to times when the IMF variation is large enough that the field points in a reverse cross-flow sense, as will be described shortly. At these times it is necessary to reflect not only the field, but also the location in the tail in the

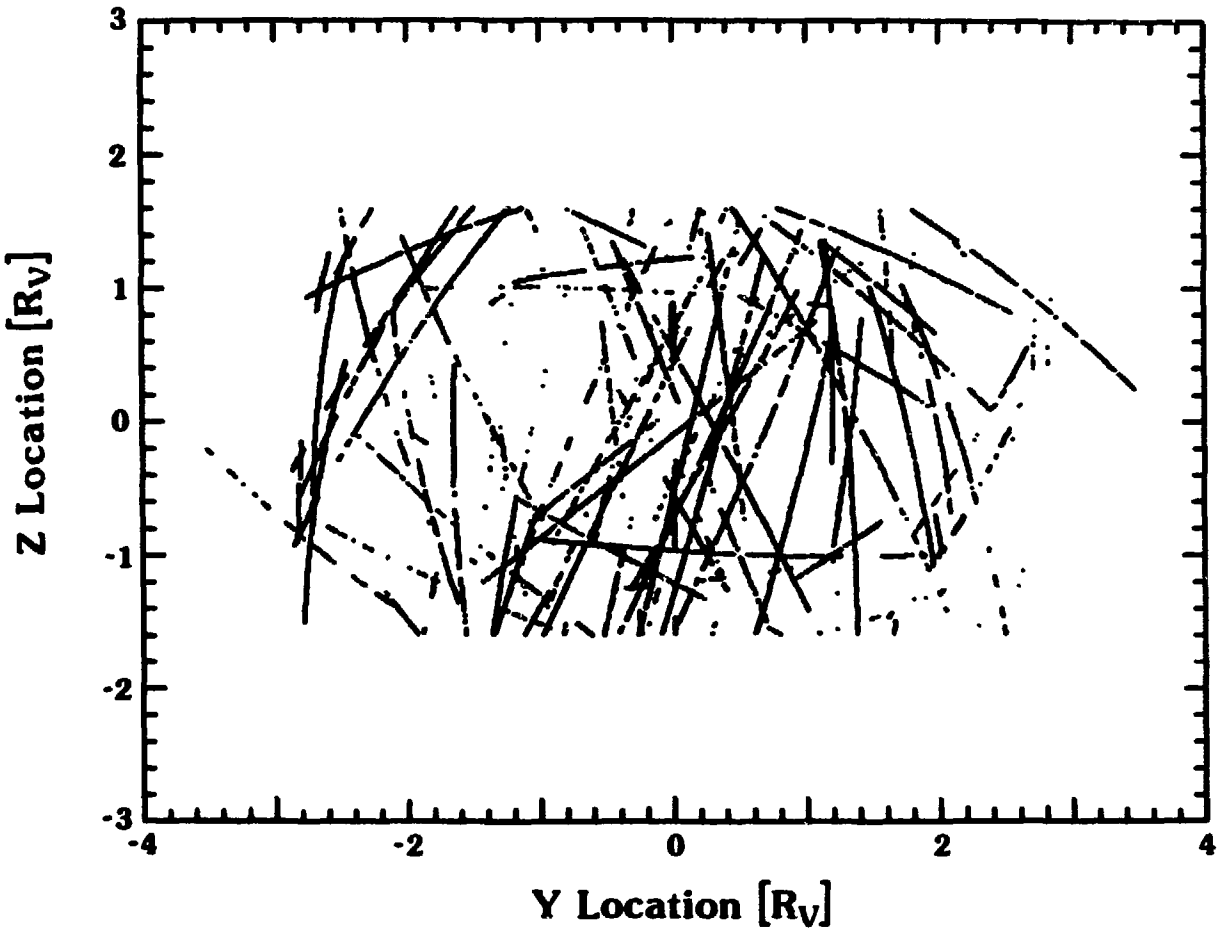

Fig. 3.2. The orbital coverage of our data set which includes 9423 one-minute averaged magnetic field data points. The data are shown in the Y-Z plane of the cross-flow (B-v) coordinate system in which the upstream magnetic field points along the +Y axis. The data set is truncated at Z = ±1.6 R_V in order to reduce the effects of a circular tail cross section when the data set is compressed in Z.

cross-flow coordinates so that toward and away sectors are, again, not mixed.

In both panels of Figure 3.3 the magnitude of the magnetic field in the tail divided by the average magnitude of the magnetic field in the magnetosheath, immediately adjacent to the tail where the PVO pierces the magnetopause, on an orbit-by-orbit basis is plotted versus the angle of the field from the cross-flow Y-Z direction toward the positive aberrated X-axis. Of course, the magnitude of the magnetic field within the sheath is a function of location as well as the upstream conditions. Along the flanks of the tail from -8 to -12 R_V, however, the fractional magnetic field strength (compared to upstream) is probably not a strong function of the exact location of the PVO's magnetopause crossings and only serves to introduce scatter into the effect observed in Figure 3.3. Still, this figure clearly reveals a strong correlation between fields which are close to $\pm 90^{o}$ and the larger relative field strengths. We identify these regions where the field is comparatively strong and points basically tailward or Venusward as being the induced lobes of the Venus magnetotail. The term "induced lobes" is used to distinguish these regions from the tail lobes in the terrestrial magnetosphere where the earth's intrinsic dipole field plays a fundamental role. At Venus the draped lobe regions are comprised purely of "hung up" interplanetary magnetic field lines.

In contrast to the induced lobes, the magnetic field in the Venus tail current sheet is observed to occur at small angles and at

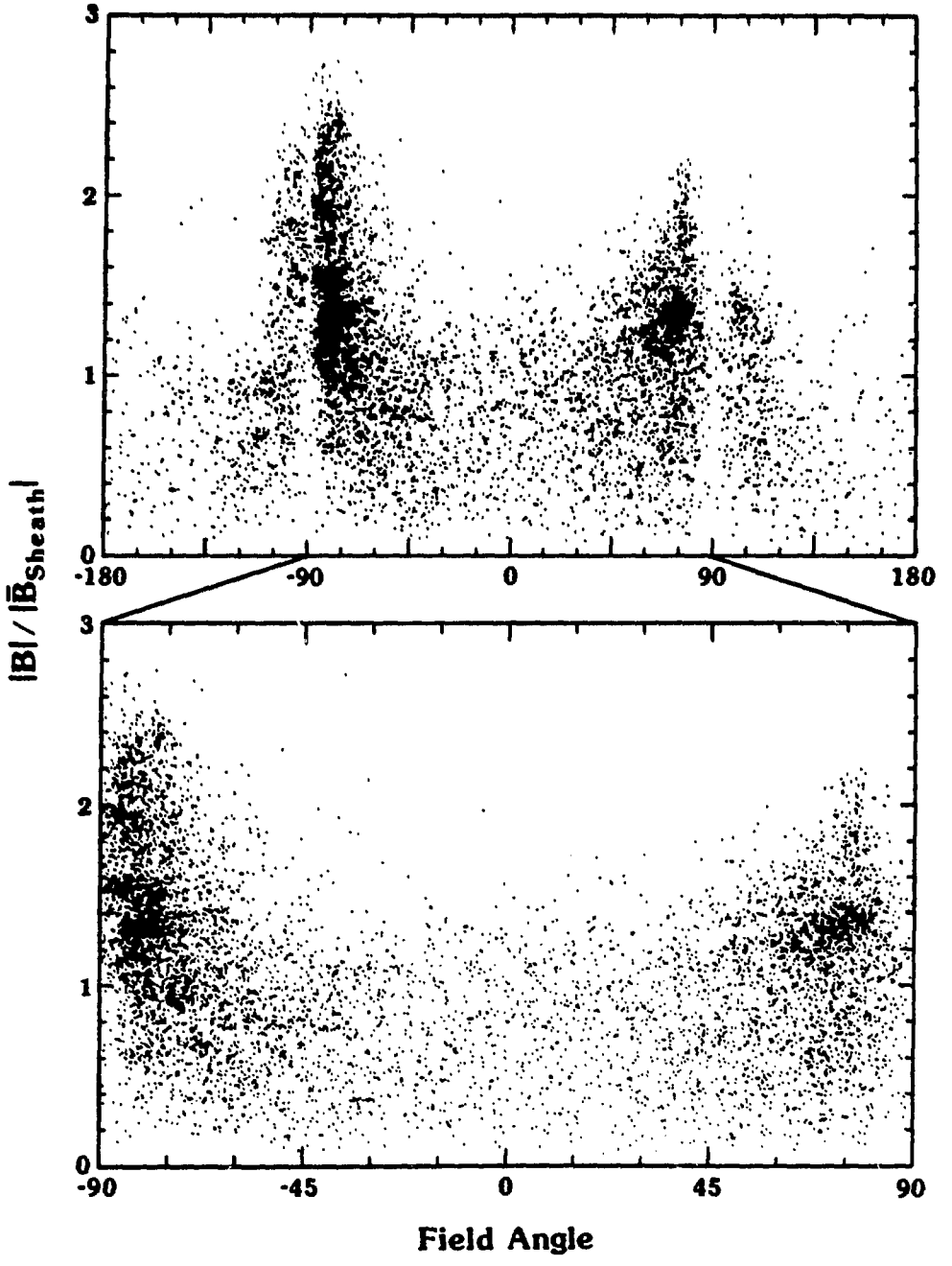

Fig. 3.3. The magnitude of the magnetic field divided by its average value in the immediately adjacent portion of the magnetosheath, plotted versus the magnetic field angle as measured from the cross-flow Y-Z direction toward the aberrated X axis. The top panel shows a correlation between large relative field strengths and angles near ±90°, and indicates that 79% of the data lie within these angles. The bottom panel shows the same data set where the remaining 21% of the data have been folded into the central portion (see text).

small field strengths. The decrease in the relative field strength may be due to a diamagnetic reduction in the center of the tail consistent with an increase in the plasma density, as is observed in the earth's magnetotail. Exclusions near $\pm 90^{o}$ may be due to the purely geometric effect of reduced solid angles near $\pm 90^{o}$, or may indicate that the angles in the lobes never truly achieve $\pm 90^{o}$ and that the variations in aberration of the tail are smaller than or comparable to the spread in the draping angle in these lobes.

Twenty-one percent of the data in the top panel of the figure are observed to lie outside of $\pm 90^{o}$. In order to determine whether this was a property of the tail, or caused by the variability of the upstream conditions, the same analysis which yielded this result was repeated on 2701 minutes of magnetosheath data taken just outside the Venus tail over the same orbits as in our tail data set. In the magnetosheath this reverse draping, which is indicated by angles outside of $\pm 90^{o}$, occurred 16% of the time. Therefore, approximately 16% out of 21% of the tail data which lies outside of $\pm 90^{o}$ is accounted for simply by the fluctuations in the upstream IMF direction causing reverse draping. The extra 5% which is still unaccounted for may be due to reconnection or other physical processes. In any case, for the first time, an upper bound has been set on the importance of magnetic reconnection in the Venus magnetotail. Only ~5% of the observed field in the Venus magnetotail points in a reverse draped sense, and therefore our analysis indicates that magnetic reconnection is probably not an important physical process in the central Venus magnetotail.

The same data set is shown in the bottom panel of Figure 3.3, with the measurements outside of ±90° "folded" across the ±90° lines. This folded data set will be used throughout the remainder of this study in order to obtain the most statistically significant results. Folding is reasonable since the observed variation between lobe and current sheet also occurs outside of ±90° where the 0° current sheet area is similar to the ±180° portion. Since 3/4 of the data outside of ±90° can be accounted for by variations in the IMF, truncation of these data would principally lower the statistics of the data set. It is therefore advantageous to fold these data back into the data set by reflecting the data points across ±90°.

A similar plot for orbit 1761 alone is shown in Figure 3.4. (The magnetometer data for this orbit are displayed in Fig. 2 of Saunders and Russell [1986].) The data points have been connected to show the time series in which the data were taken. In motions between the two lobes, the spacecraft always encounters the current sheet. That is, there are one or more data points obtained within the current sheet, which are characterized by small angles and small field strengths, in the transition from one lobe to another. The motion of the spacecraft back and forth in the tail is clearly not due to the spacecraft orbital motion (24 hours/orbit), since there are many of these comparatively quick (a few minutes) crossings in a single orbit. Rather, some sort of large variations in the tail configuration (perhaps due to the IMF X-component) and/or in its location occurs on the time scale of a few one-minute data samples. These variations cause the spacecraft to be alternately in one lobe

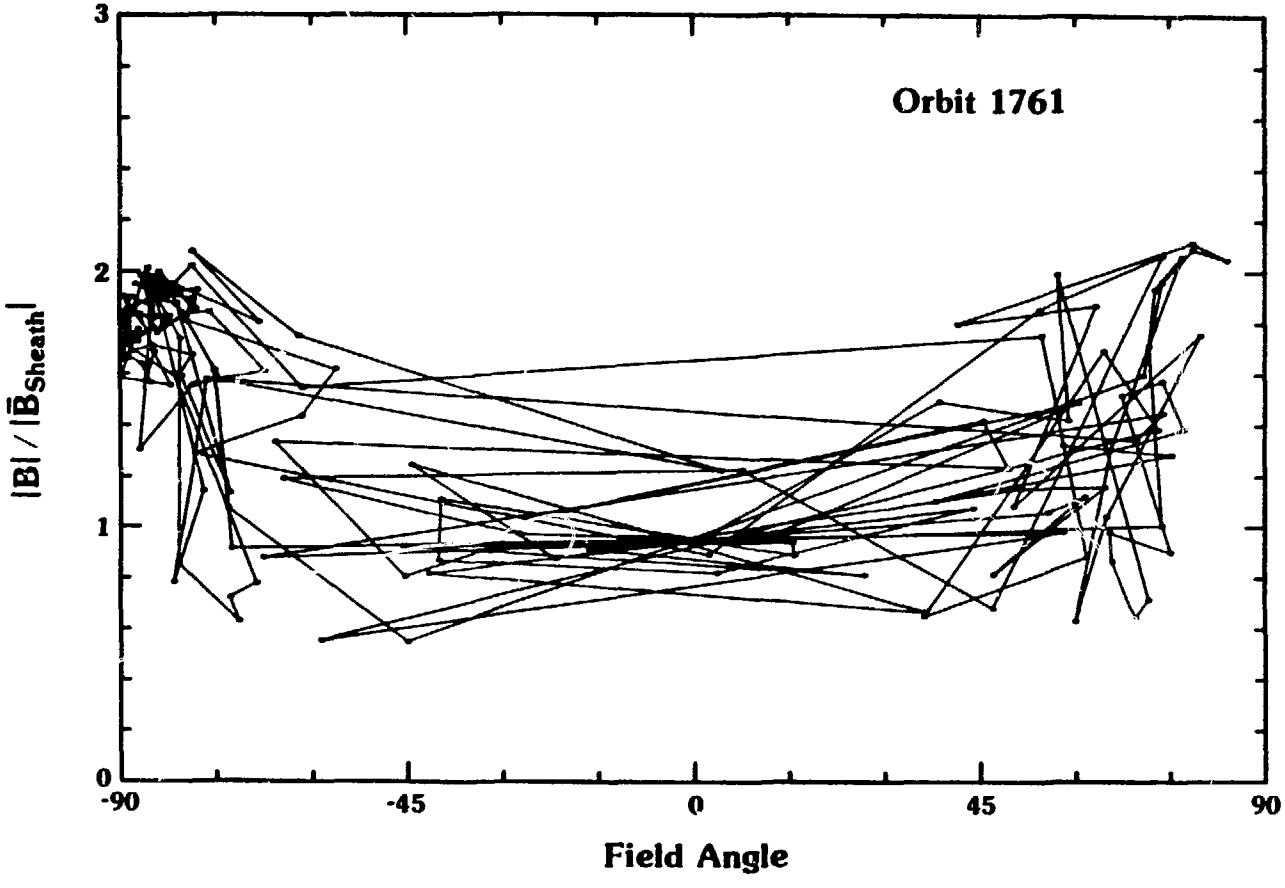

Fig. 3.4. Similar to Figure 3.3 except that only data from orbit 1761 are shown. The data points have been connected to show the time series in which the data were taken. The spacecraft traverses the tail many times in an individual orbit. Evidently the size scales of motions and/or reconfigurations of the tail are much larger than those due to the actual orbital motion. Therefore, the data will be much better ordered by a coordinate system which measures locations with respect to the internal tail structures rather than one which measures them in normal spacecraft coordinates.

and then the other, crossing back and forth across the current sheet many times. This temporal variation has previously made it impossible to do a thorough analysis of the average spatial structures of the Venus tail. These large variations, however, are used in a new way in the next section of this study to improve the statistics.

The field angle versus the B-v Y location is shown in Figure 3.5. Current sheet(s) and lobes are observed at all locations where the tail is encountered, which is consistent with the observations of large variations in most orbits, and as is exemplified by the plot of orbit 1761. In Figure 3.5 there is a clear preponderance of either tailward or Venusward pointing fields on each of the two sides of the tail. Magnetic fields near $+90^{o}$ occur preferentially on the -Y side of the tail, while fields oriented near -90^{o} occur predominantly on the +Y side. In Figure 3.6 this finding is quantified.

For the purposes of determining the number of induced tail lobes, we have, somewhat arbitrarily, defined them as consisting of all data points in which 1) the field strength divided by the directly adjacent sheath value (as described previously) is greater than one, and 2) the absolute value of the angle is greater than 60^{o} (upper left and right corners of Fig. 3.4 and the lower panel of Fig. 3.3). The fraction of the tailward pointing tail lobe is plotted versus the B-v Y location in Figure 3.6, and two draped lobes are clearly indicated. The number of draped lobes was not something that was assumed in our analysis, but rather it is a

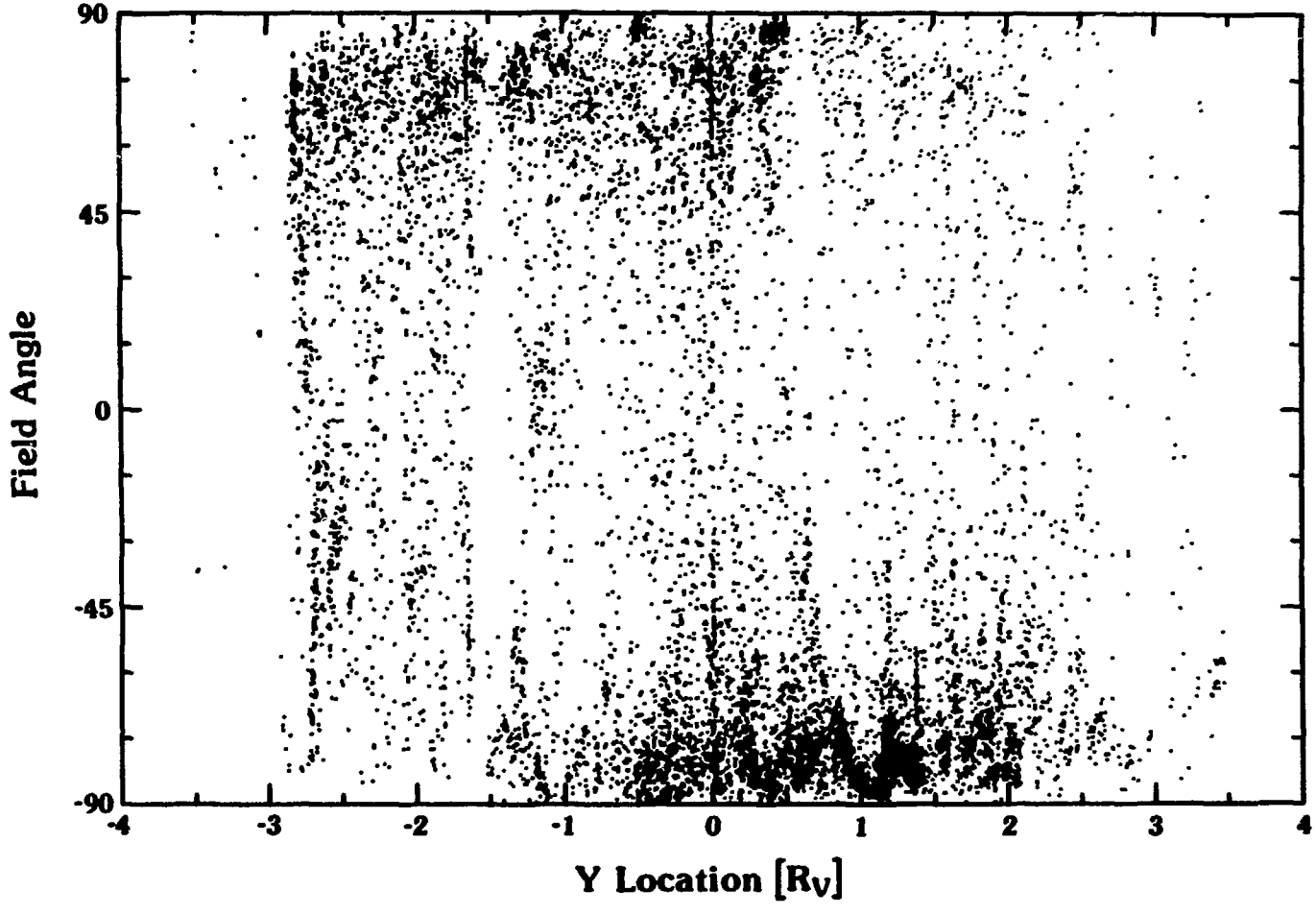

Fig. 3.5. The magnetic field draping angle versus the B-v Y location. Both direction lobes and current sheet(s) are observed at all locations antisunward of Venus. There is, however, more tailward pointing lobe data on one side of the plot and more Venusward pointing data on the other side.

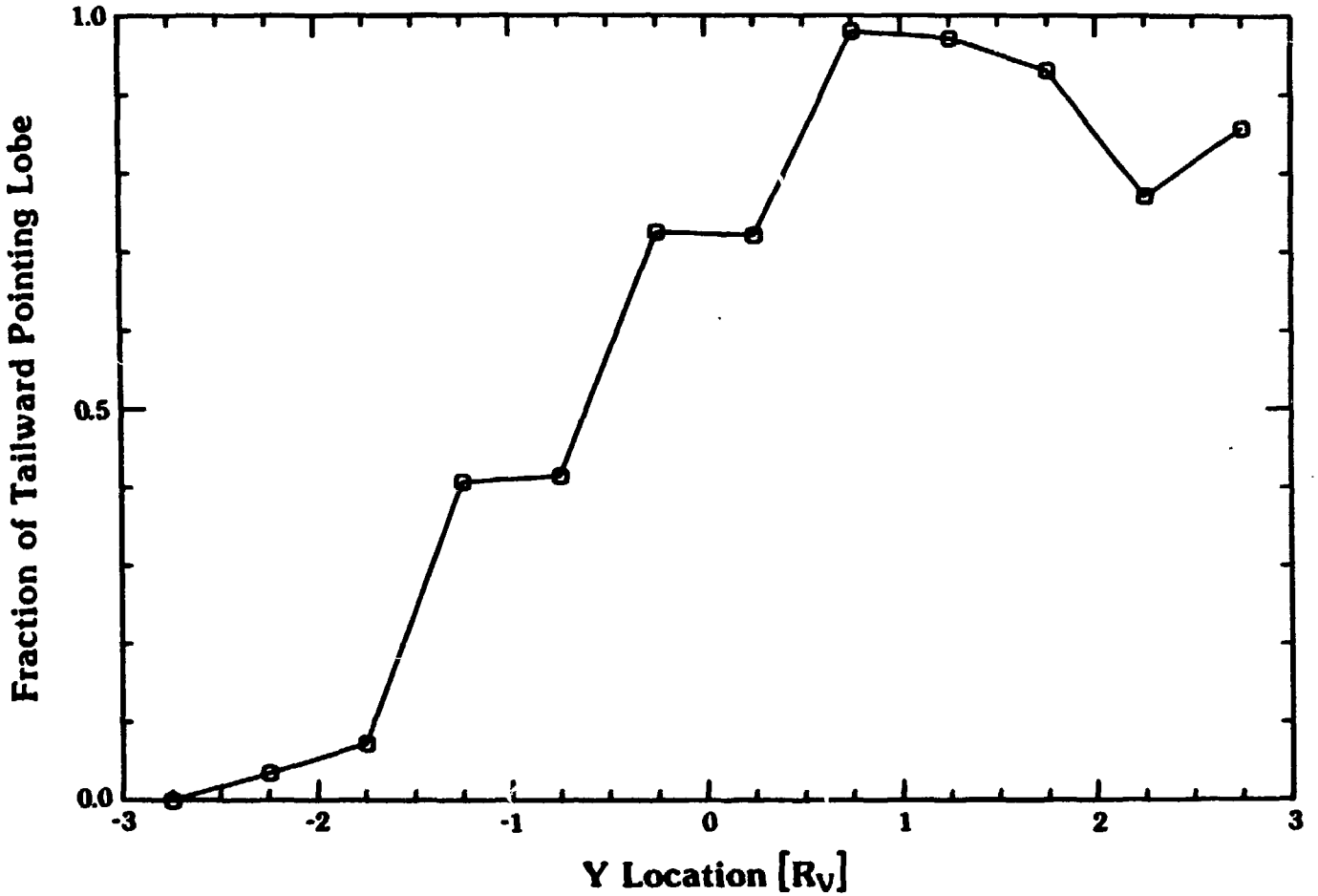

Fig. 3.6. The fraction of tailward pointing lobe as a function of the B-v Y location. The average tail configuration consists of only two draped lobes which are separated by a single field reversing current sheet.

result confirmed by our analysis, which merely assumed that magnetic field draping is the important phenomena in the tail. We have repeated this analysis using other lobe cutoff criteria, and all yield the same result.

Figure 3.4 demonstrated that draped lobes are separated by current sheets, while Figure 3.6 confirms that there are only two lobes in the Venus magnetotail. Therefore, the Venus magnetotail structure is shown to consist of two roughly opposite pointing draped lobes separated by a single current sheet just as we anticipated in Figure 3.1. The average location of the current sheet center is approximately -0.5 R_V. This is consistent with the IMF X-component mapping into the tail such that, for a normal Parker spiral pattern and an away-sector, the magnetic flux in the draped lobe which contains the tailward pointing field is larger than the flux in the draped lobe containing the Venusward pointing magnetic field. In a pressure balance situation, the current sheet between these two lobes will tend to move toward the side of the Venusward pointing lobe.

Since we are principally interested in determining the average configuration of the Venus magnetotail, the average field line draping angles in the lobes must be determined. Figure 3.7 shows the measured average lobe angles determined using the lobe criteria described above for Figure 3.6. Other, similar lobe criteria have also been tried and yield very similar average angles. These field angles in the two lobes will be used to set the average angle to which the field drapes in the lobes on the distant sides of the

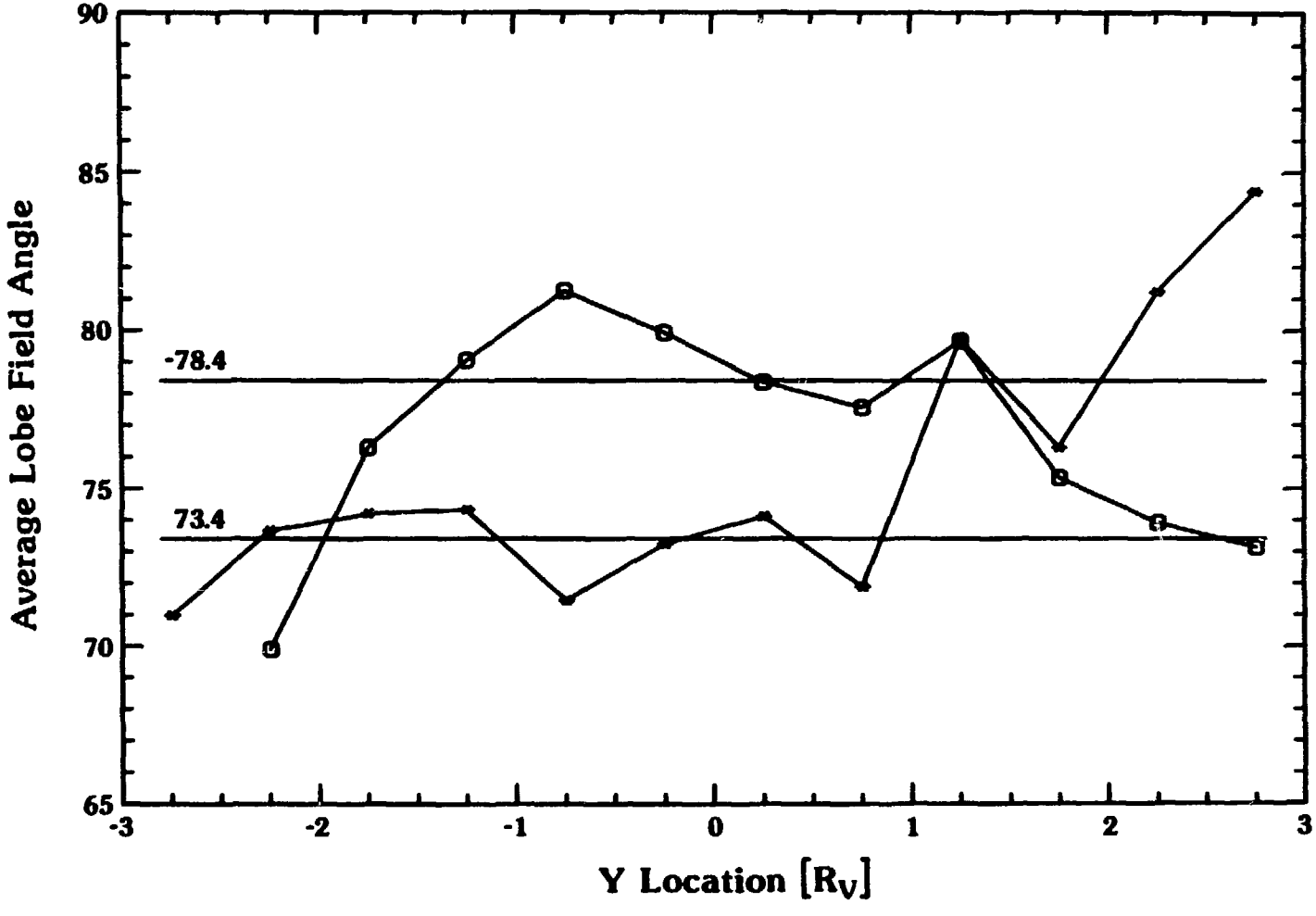

Fig. 3.7. The average angles of the field line draping in the outer portions of the two lobes. The tailward pointing lobe value is -78.4° while the Venusward pointing lobe is +73.4°.

tail. The tailward pointing lobe average angle is -78.4^{o}, while the Venusward average angle is $+73.4^{o}$. This asymmetry can also be accounted for quite simply by the mapping of the IMF X-component through the magnetosheath and into the tail as shown in Figure 3.1.

3.3 The Average Tail Configuration with the Effects of Flapping Removed

In all previous studies, and thus far in this study, the Venus magnetotail data have been ordered only by the spatial location of the PVO with respect to Venus. Our analysis, however, has indicated that motions and/or reconfigurations of the tail happen far more rapidly than the PVO orbital motion, causing the spacecraft to traverse the tail many times per orbit. In order to advance the understanding of the Venus magnetotail quantitatively, it is necessary to find a coordinate system which better orders these highly variable data by statistically organizing them with respect to the tail features themselves. Since a relation between the diamagnetic reduction and the field angle has already been demonstrated, it is reasonable to construct a coordinate system in which cross-flow locations do not correspond to locations in physical space, but rather correspond to locations with respect to the center of the moving or flapping current sheet.

For the data set used in this study, we have empirically determined the tail width to be 5.1 R_V. This was accomplished by determining the fraction of time that each spatial location behind Venus was engulfed within the tail. Since tail motions are large,

even the average center location of the tail was apparently within the actual tail only ~97% of the time, and locations to the sides were within the tail far less. Under these conditions it is not appropriate to simply find the locations which are within the tail 50% of the time, and determine the average width of the tail from these. Rather, the fractional tail coverage behind the planet must be integrated, and the effective tail width calculated from it such that this integrated value equals the tail width multiplied by 100% (of the time).

We have already shown that the magnetotail is comprised of two draped lobes separated by a cross tail current sheet and that fields on the +Y side of the tail point tailward, while the fields on the -Y side point Venusward for an away IMF sector draping. Further, since the diamagnetic reduction apparently gives a measure of the average distance from the center of the current sheet, we can now build a coordinate system which is centered on the current sheet and which measures distances from that center. Large variations in the tail configuration and location cause all regions to be sampled at any physical location in the tail. In a statistical data set, such as the one used for this study, the fraction of the total data points which lie within any given angular range gives a direct measure of the relative width of that portion of the tail. The sum of all of these relative widths must, of course, equal the total width of the Venus tail, 5.1 R_V. It is then possible to construct the average configuration of the tail by starting with the average

angles derived in each of the two lobes and calculating the thickness of each of the angular bins across the tail.

The basic principal involved in creating such a coordinate system is shown schematically in Figure 3.8. For simplicity the tail has been divided into only three portions, namely, the +X pointing lobe, the -X pointing lobe, and the current sheet. The lower portion of the figure is a schematic diagram of Figure 3.5. Since variations of the spacecraft position with respect to the internal structures of the tail are so large, all regions are sampled at every B-v Y location, and the fraction of field in each of the three angle bins gives a direct measure of the thickness of that portion of the tail. In this example the +X lobe, current sheet, and -X lobe are 32%, 28%, and 40% of the tail width respectively. Since the tail is 5.1 R_V across these would correspond to 1.6, 1.4, and 2.1 R_V for each portion, respectively. This technique is simply extended in our study to measure the thickness of each one degree angle bin across the tail, and thereby we reconstruct the average tail configuration. The resultant Y* coordinate axis constructed by this technique is parallel to, and shares a Venus centered origin with, the B-v Y-axis.

The angle of the magnetic field versus this cross tail location, Y*, is shown in Figure 3.9. The cross tail locations of various angles in the tail have been determined as described in the previous figure while the X-axis in these new coordinates is the same as the X-axis in the aberrated VSO coordinates. The procedure described above of dividing up and determining the relative amount

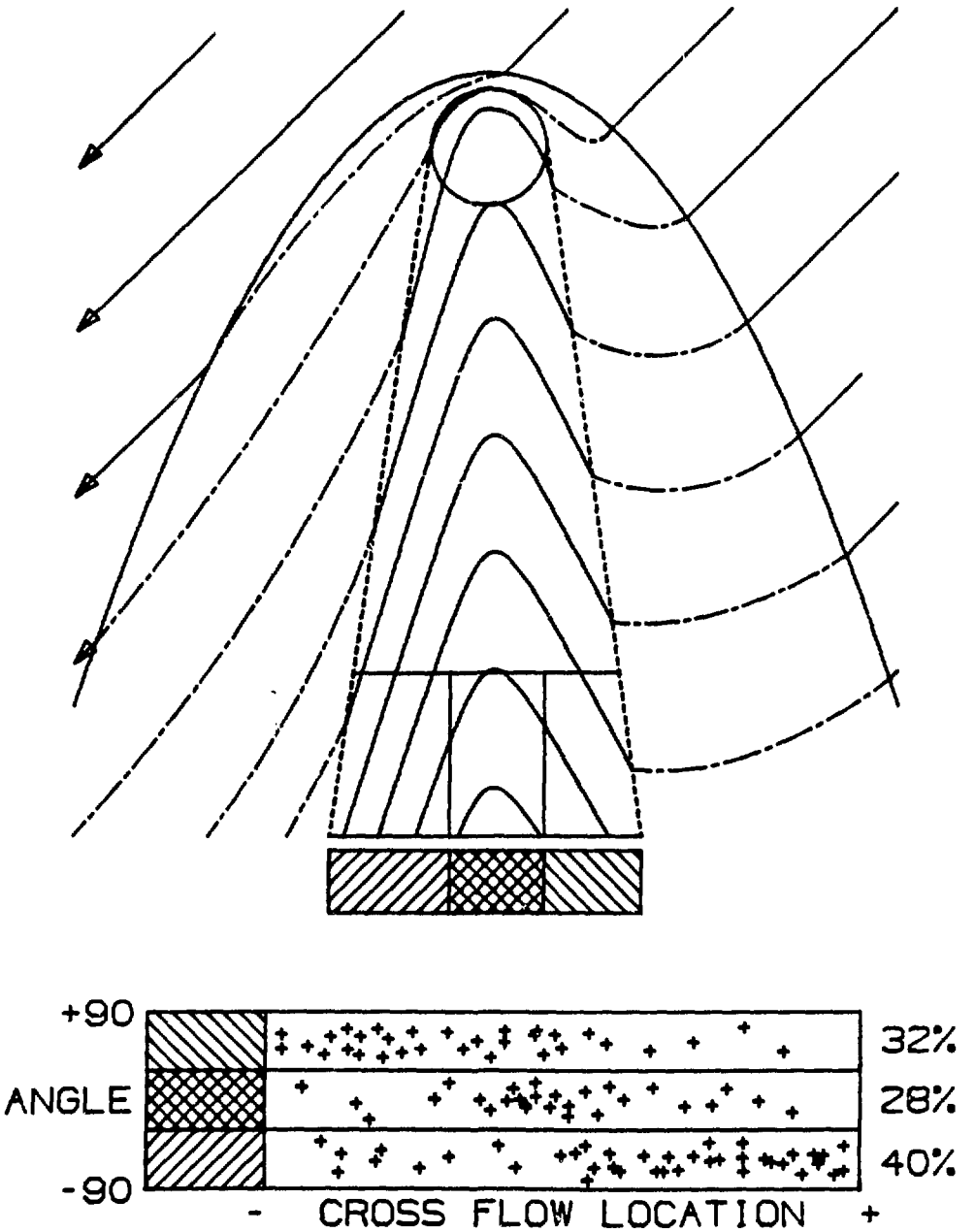

Fig. 3.8. Schematic diagram of the basic principle used in defining our constructed coordinate system which measures locations with respect to the internal tail structure. The fraction of data points within any range of angles gives the relative thickness of the portion of the tail which encompasses those angles. Combining this information with the total, physical width of the tail gives the spatial scale to the cross tail coordinate axis.

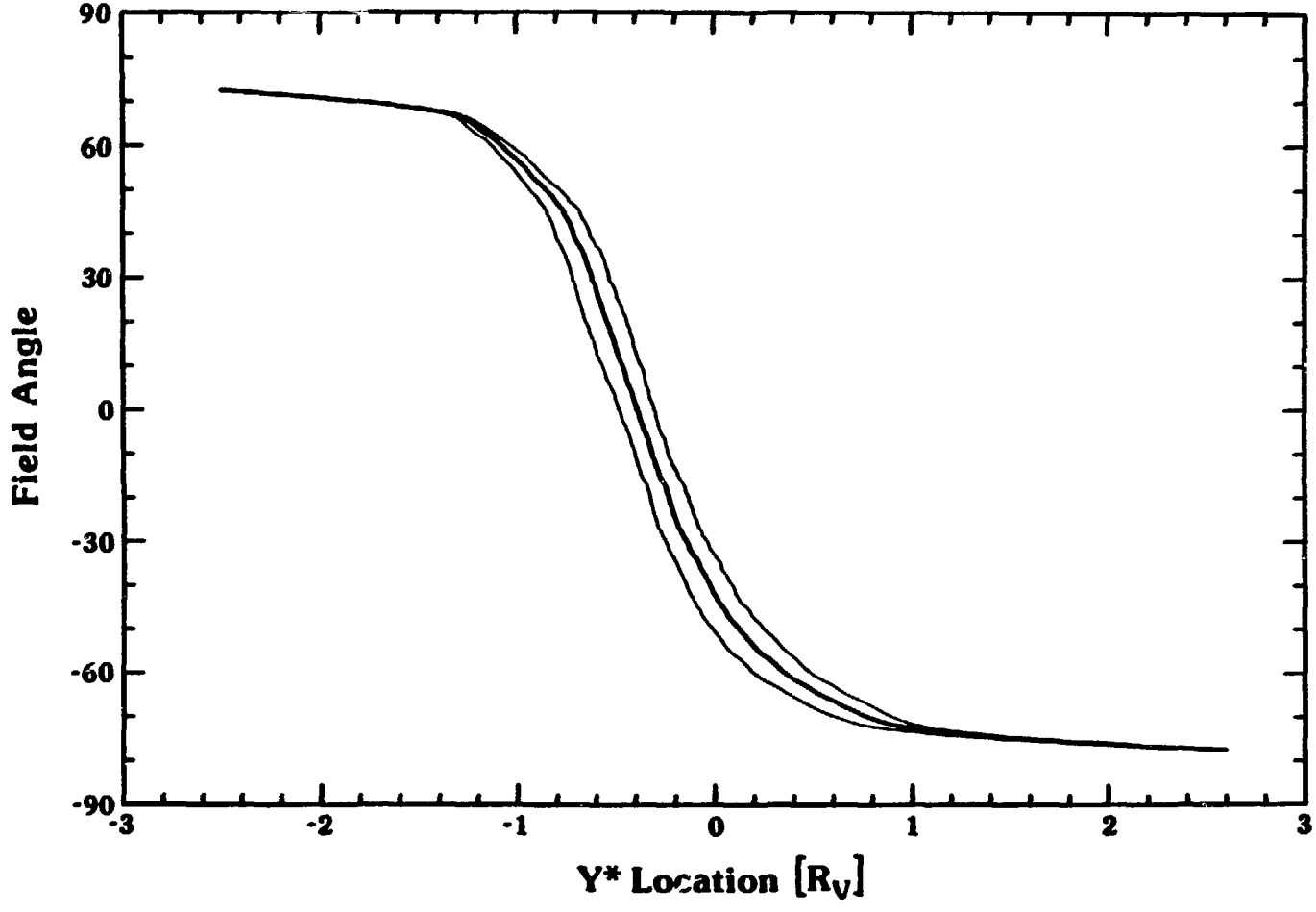

Fig. 3.9. The angle of the magnetic field plotted versus the Y* location. The two lighter lines are the upper and lower bounds found by carrying out our analysis over ±0.5, 1.0, 1.5, 2.0 R_V. The darker, center line is the average of these and is adopted for the remainder of this study.

The tailward/Venusward magnetic field, B_X, is plotted versus Y* in Figure 3.10. These are actual measurements over the 9423 data points binned up angle by angle and compared to their Y* locations, and are not calculated from the angles used to derive the (*) coordinates. This plot, therefore, gives a good independent check of the ability of the (*) coordinate system to order the data. The two draped lobes are easily discerned in this plot as is the smooth variation between the two through the current sheet. The zero point in B_X once again occurs slightly offset toward the negative side of the tail. The variation displayed has been calculated in an average sense over X; the entire data set has been compressed in X so that only variations in the cross tail direction are determined. Throughout this paper such averages will be indicated with <>, so that B_X as a function of Y*, and averaged over X is written $\langle B_X(Y^*)\rangle_X$. This average B_X as a function of Y* will be used shortly to calculate one of the terms of the current density distribution in the cross tail current sheet.

A similar plot for the cross-flow magnetic field, B_Y*, as a function of Y* is displayed in Figure 3.11. The distribution has been calculated in 11 bins in Y* to improve the statistics. The double humped variation exhibited in this plot is qualitatively similar to the variation observed in the Fedder simulation of cometary magnetotails (J. Phillips, private communication; Fedder et al. [1986]). By combining the results in Figures 3.10 and 3.11, the field draping in an average sense across the tail is determined. This average draping pattern is shown in Figure 3.12. It must be

of data in each one degree angle bin has been carried out over ±0.5, 1.0, 1.5, and 2.0 R_V in B-v Y from Figure 3.5. All four of these analyses were carried out independently, and the minimum and maximum angles of the four have been plotted at each Y* location to give the upper and lower bounds, displayed as the two light lines in Figure 3.9. The darker, center line is the average of these four analyses and is adopted for the purposes of this study hereafter. The very small variation between the center average line and the minimum and maximum lines indicates that it is relatively unimportant over how much of the central portion of the tail the analysis is done. Variations are sufficiently large in tail configuration and location that all portions of the tail are sampled with little orbital prejudice everywhere between ±0.5 and ±2.0 R_V. This, then, is the (*) coordinate system in which we can much better measure the average physical features of the Venus tail.

Angles beyond the average angles found in the lobes have been folded into the angles just below the average lobe angles. This is necessary because the analysis fails as the lobe draping angle approaches ±90°, and at angles of ±90°, the field lines would apparently not cross the tail at all. We expect that these infrequently measured large angles are not characteristic of the actual, averaged draping, and probably result from variations in the aberration angle of the tail. Since we are principally interested in the average magnetic field draping in the tail, it is desirable to have the fields come to their average lobe values at the edges of the lobes.

The tailward/Venusward magnetic field, B_X, is plotted versus Y* in Figure 3.10. These are actual measurements over the 9423 data points binned up angle by angle and compared to their Y* locations, and are not calculated from the angles used to derive the (*) coordinates. This plot, therefore, gives a good independent check of the ability of the (*) coordinate system to order the data. The two draped lobes are easily discerned in this plot as is the smooth variation between the two through the current sheet. The zero point in B_X once again occurs slightly offset toward the negative side of the tail. The variation displayed has been calculated in an average sense over X; the entire data set has been compressed in X so that only variations in the cross tail direction are determined. Throughout this paper such averages will be indicated with <>, so that B_X as a function of Y*, and averaged over X is written $\langle B_X(Y^*)\rangle_X$. This average B_X as a function of Y* will be used shortly to calculate one of the terms of the current density distribution in the cross tail current sheet.

A similar plot for the cross-flow magnetic field, B_Y*, as a function of Y* is displayed in Figure 3.11. The distribution has been calculated in 11 bins in Y* to improve the statistics. The double humped variation exhibited in this plot is qualitatively similar to the variation observed in the Fedder simulation of cometary magnetotails (J. Phillips, private communication; Fedder et al. [1986]). By combining the results in Figures 3.10 and 3.11, the field draping in an average sense across the tail is determined. This average draping pattern is shown in Figure 3.12. It must be

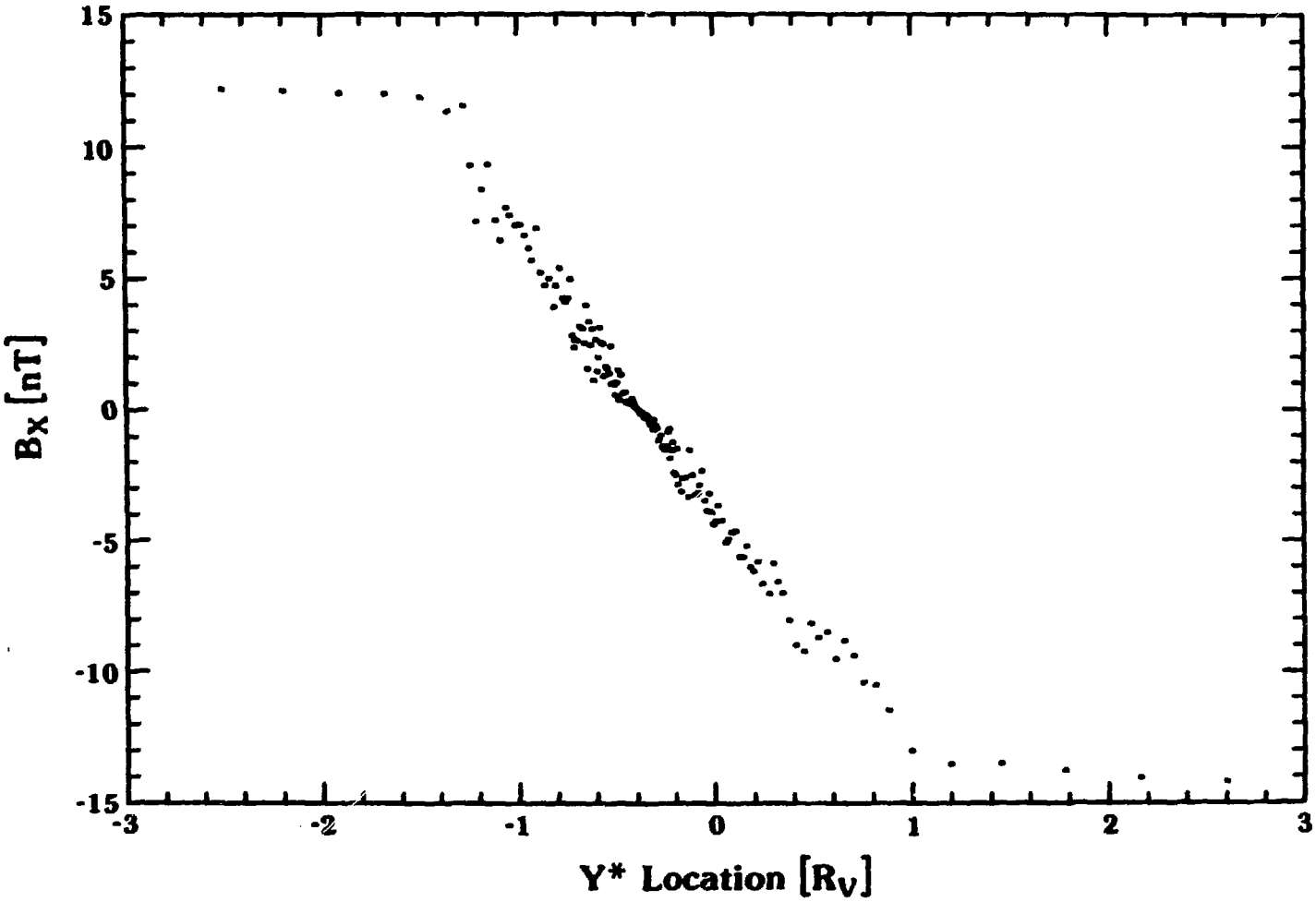

Fig. 3.10. The actual, measured B_x plotted versus Y* in each of the one degree angle bins. This plot gives a good independent check of the ability of the coordinate system to order the data set.

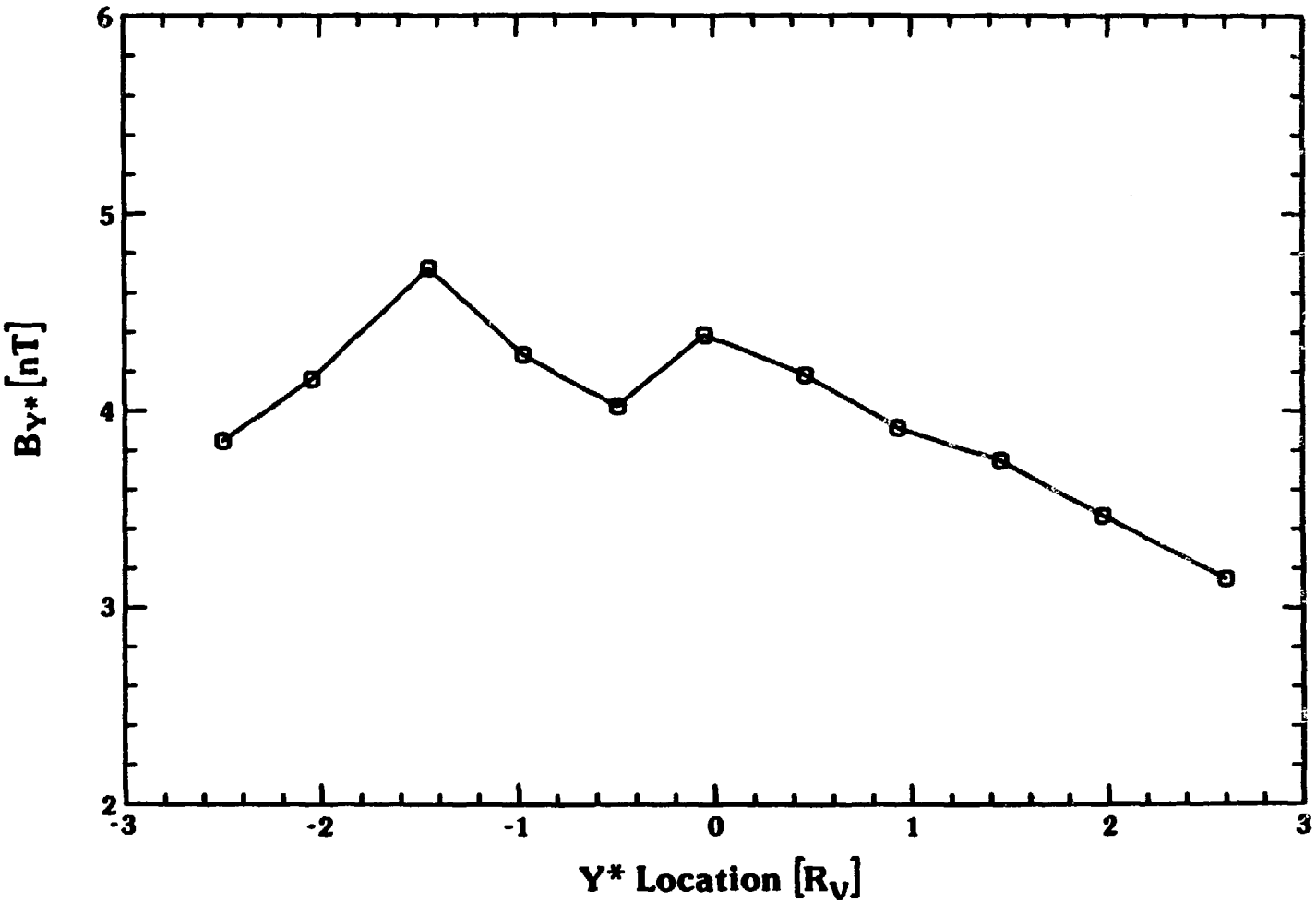

Fig. 3.11. The measured B_{Y^*} plotted versus Y*. The variation is calculated in eleven bins across the tail, which vastly improves the statistics.

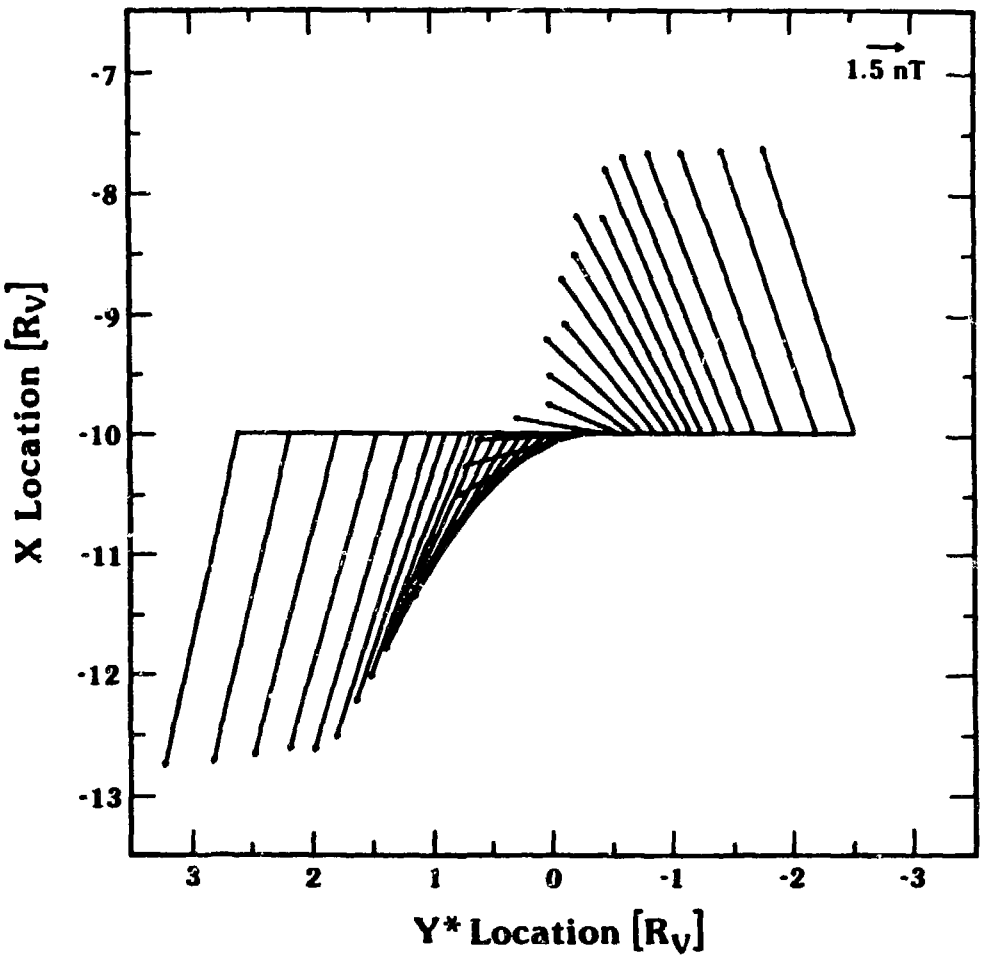

Fig. 3.12. The average magnetic field vectors determined with our technique as a function of the Y* location across the tail. The two draped lobes and the smooth rotation through the current sheet between them are all clearly shown.

emphasized that these are not magnetic field lines, but rather average field vectors in a crosscut through the tail along Y*. Data from -8 to -12 Venus radii have been compressed in X to give this draping pattern. Figure 3.12 clearly displays the two draped lobes and current sheet in which the field smoothly rotates from one lobe to the other. The tailward side is thicker due to larger flux content, as well as having a larger tailward field component due to the mapping in of the X-component of the IMF, just as we postulated in Figure 3.1.

Next, we extend the understanding of the field draping in the tail by examining variations of the field in the X-direction. Unfortunately, it is only possible to examine the B_{Y*} field variation with X since the B_X variation is such a critical function of sampling location in Y*. B_X varies from about ±13 nT in the lobes to zero in the center of the current sheet, and, therefore, any orbital bias can strongly affect the determination of the exact variation of the X-component. On the other hand, the B_{Y*}-component is relatively constant across the tail and is therefore not much affected by orbital bias. In the top panel of Figure 3.13 we show the orbital coverage in 0.5 R_V bins, where data from -6 to -12 R_V have been included in order to maximize the region covered. The distribution strongly favors data being taken past -10 R_V due to the fact that the PVO orbit apoapsis occurs near -12 R_V.

The lower panel of Figure 3.13 displays $B_{Y*}(X)$ along with the best linear fit to this variation. This best fit line equally weights all data points and does not, therefore, overly stress the

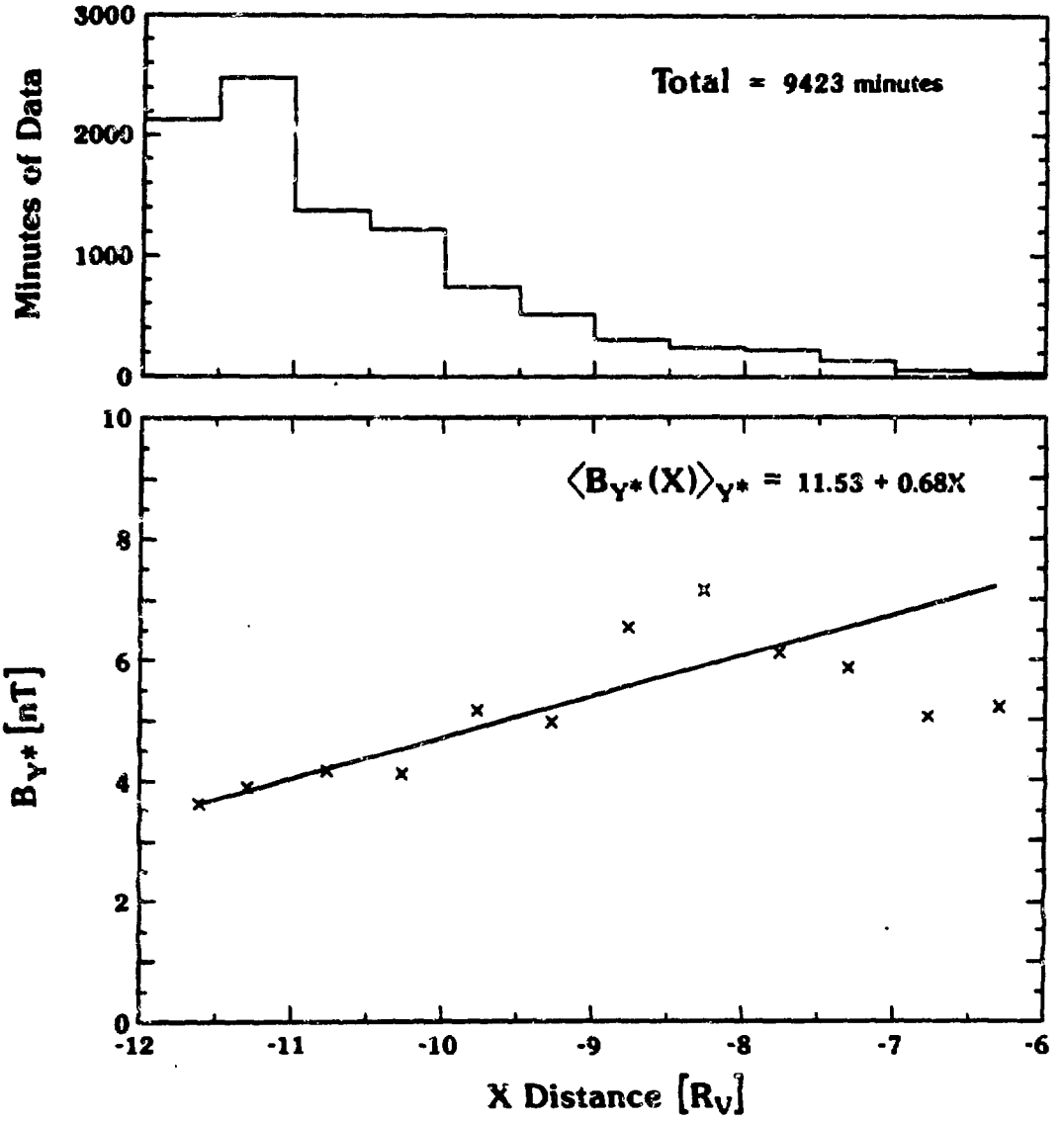

Fig. 3.13. The previous analysis is extended to examine the variation of the field with downtail, X, distance. The top panel shows the orbital coverage of our data set as a function of X, while the bottom panel shows the Y*-averaged variation of $B_{Y^*}(X)$. The best linear fit to this variation is also shown.

less significant data bins closer to the planet. The equation for this best fit line for B_{Y*} as a function of X, again averaged over Y*, is $\langle B_{Y*}(X)\rangle_{Y*} = 11.53 + .68(X)$ in nT, where X is in Venus radii. From this variation and from the variation which was shown in Figure 3.10, the cross tail current density can be calculated.

The cross tail current density is numerically evaluated from the curl of the magnetic field according to Ampere's Law. Using the average variation just described $d\langle B_{Y*}\rangle_{Y*}/dX = .61$ in the units of nT/R_V from the linear fit to the field variation. This gives a small offset most easily observed in Figure 3.14 at the two far sides of the tail, while the principal variation in current density through the center is due to the term $dB_X/dY*$ and is calculated from the variation shown in Figure 3.10. For Figure 3.14 we have derived the cross tail current density in 11 steps in Y* to smooth out variations which are observed in the derivatives. Clearly the cross tail current density is maximized near the center of the tail at $-.5\ R_V$ and drops to very small values which correspond primarily to the linear dB_{Y*}/dX term near the edges of the lobes.

From this calculated variation and from the field which was shown in Figure 3.12, the $\underline{J}\times\underline{B}$ forces can be calculated in an average sense across the tail. These forces are shown in Figure 3.15. All forces have a tailward component, and these -X-directed forces maximize in the center. Forces on both sides of the tail all point toward the center of the tail. Throughout the side portions of the tail these inward forces, F_Y, are greater than tailward F_X forces. Asymmetries in the side to side distribution of forces are due not

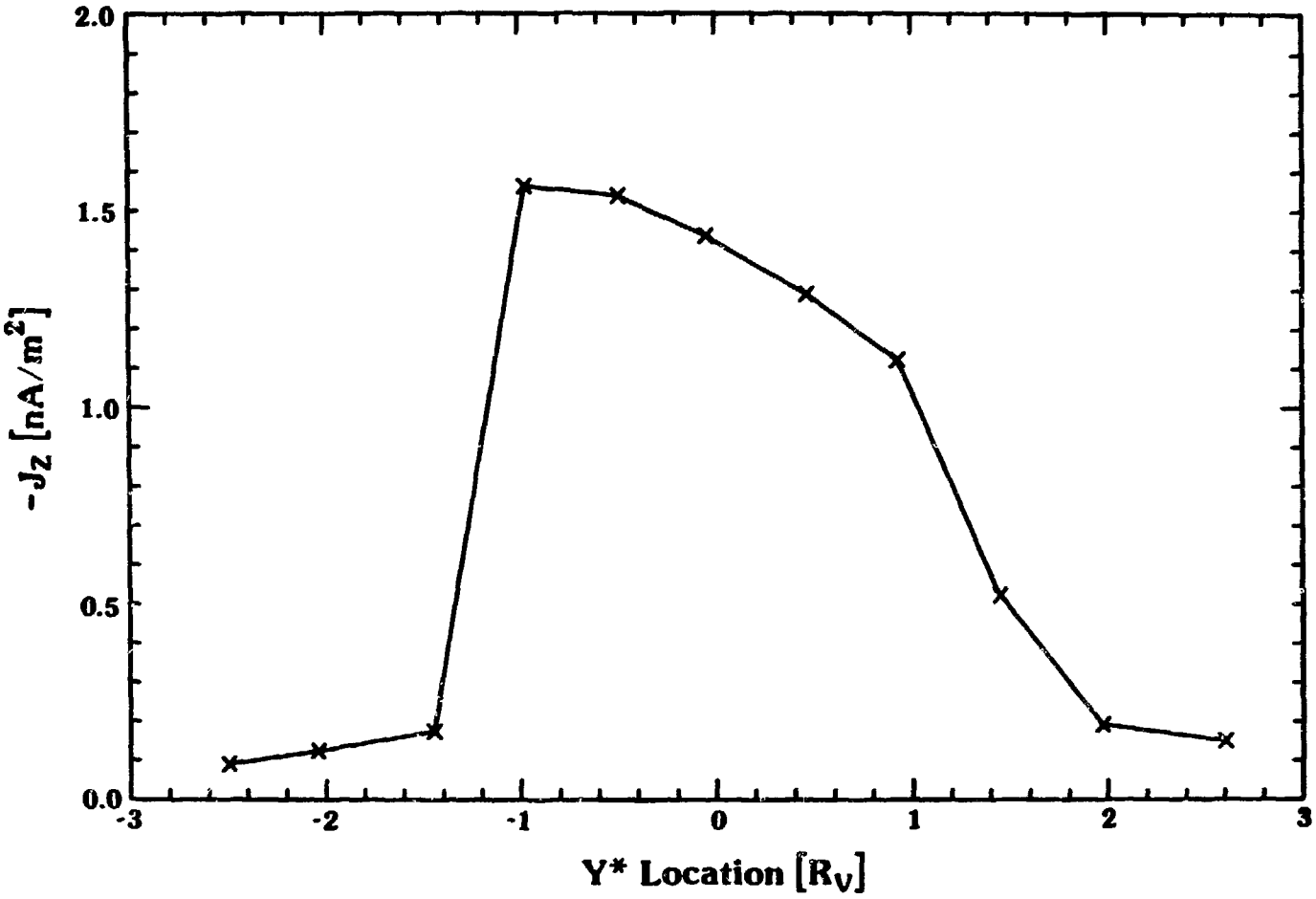

Fig. 3.14. The cross tail current density as a function of cross tail location. Both terms of the curl of the field are included in this calculation. $\partial B_{Y*}/\partial X$ gives a small constant offset which is most easily observed at the two edges of the tail, while the primary component through the center of the tail is from $\partial B_X/\partial Y*$.

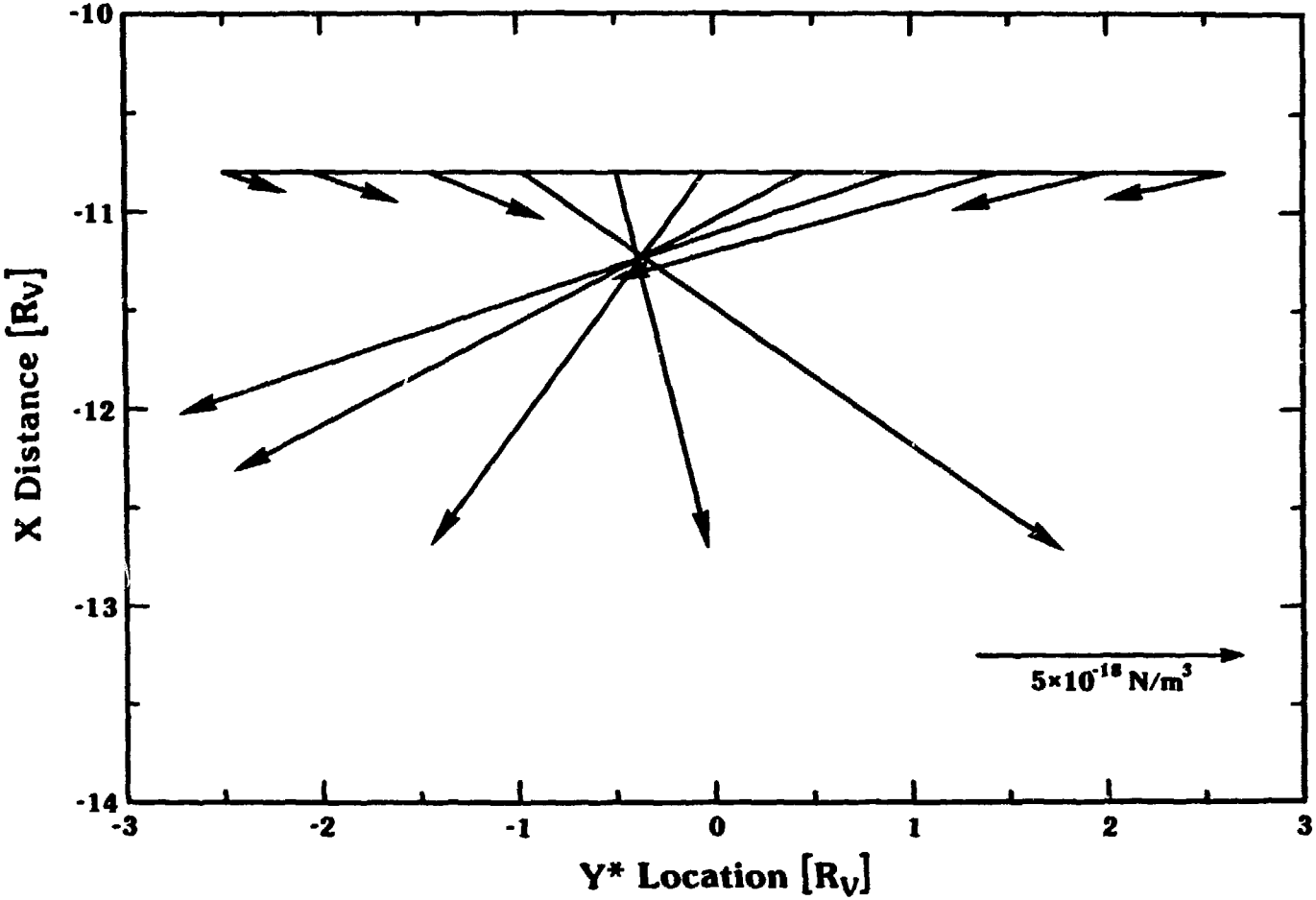

Fig. 3.15. The derived $\underline{J}$ X $\underline{B}$ forces as a function of Y* across the tail. The X directed forces all point tailward and maximize in the tail center, while the Y* directed forces point inward on both sides. These forces are the important electromagnetic term of the momentum equation with which we examine the consistent plasma properties of the Venus magnetotail.

only to actual asymmetries in the tail configuration, but also, to some extent, to the coarseness of our sampling in Y*.

3.4 The Inferred Plasma Properties

The average variations of the magnetic field draping in the Venus magnetotail are not just interesting in their own right, but also contain significant information about the average plasma properties throughout this region. In particular, the X variations of the downtail plasma velocity, $v_X(X)$, and acceleration, $a_X(X)$, can be directly obtained from the average field variations and the continuity of the tangential electric field. The average plasma density in the current sheet and lobes, and average ion plasma temperature in the tail, on the other hand, can be derived from the calculated plasma acceleration and MHD momentum equation.

The reconstructed (*) coordinate system developed in this study allows us to represent the steady state, average configuration of the Venus magnetotail. As such, the effects of time-varying upstream conditions have been removed, and the resultant variations determined with our analysis can be treated as though they were derived for constant (average) upstream interplanetary conditions. In this coordinate system the consistent steady state plasma properties of the Venus magnetotail can be calculated, approximately, from our average magnetic field data. The MHD momentum equation in the two-dimensional X-Y* plane of the field draping is

$$(\underset{\sim}{J}\times\underset{\sim}{B})_X = -J_Z B_Y = \rho(v_X \frac{\partial}{\partial X} v_X + v_Y \frac{\partial}{\partial Y} v_X) \qquad (3.1a)$$

$$(\underset{\sim}{J}\times\underset{\sim}{B})_Y = J_Z B_X = \rho(v_X \frac{\partial}{\partial X} v_Y + v_Y \frac{\partial}{\partial Y} v_Y) + \frac{\partial P}{\partial Y} \qquad (3.1b)$$

The pressure gradient term has been dropped in equation 3.1a because there is no boundary confining the plasma in the -X-direction, as there are in the ±Y-directions, and the plasma is therefore free to flow downtail. For simplicity, we have dropped the (*) from all Y terms in equation 3.1 and throughout this section; however, it should be understood that all equations and discussions in this section refer to the average, steady state configuration described by the statistical X-Y* coordinate system.

If 1) the plasma pressure in the current sheet greatly dominates the magnetic field pressure ($\beta >> 1$), 2) the opposite condition holds in the lobes ($\beta << 1$), and 3) Y-directed accelerations are not too large, then the Y-directed $\underset{\sim}{J}\times\underset{\sim}{B}$ force in equation 3.1b will be primarily balanced by the gradient in the plasma pressure alone rather than the inertial forces. In this case virtually all plasma flow will be directed downtail and $V_Y(X,Y) \approx 0$. Therefore equation 3.1a simplifies to include only the first of the two spatial derivative terms. This sort of tail configuration is expected if ion pick-up (e.g., O^+) is an important physical process in the extended dayside ionosphere, or if solar wind plasma flowing near to the stagnation point on the dayside of Venus flows around

the obstacle and into the magnetotail. This limit of the equation will be explored quantitatively in this section.

Unfortunately, even the large statistical data set used in this study is insufficient to accurately determine the full two-dimensional magnetic field variations. Instead, we have derived the average variations of the tail field in directions perpendicular to these averages. For example, we derive the variations of the field with Y in an average sense in X. The task at hand now is to use these average variations to derive the average tail plasma properties. In general, the average value of a product of two functions does not equal the product of the average values of these functions. However, when one or both of the functions is approximately constant over the direction of averaging, these two types of averages are approximately equal.

The Y-averaged variation of the downtail velocity, $\langle v_X(X) \rangle_Y$, is derived from the continuity of the tangential electric field, or equivalently, the conservation of magnetic flux. The tangential electric field is

$$E_Z = -v_X B_Y + v_Y B_X \tag{3.2}$$

and is constant and perpendicular to the two-dimensional plane of the magnetic field draping. E_Z is roughly equal to the product of the X-component of the magnetosheath plasma velocity and the magnetosheath magnetic field Y-component. The average magnetic field crossing the flanks of the tail is, from Figure 3.11, 3.5 nT.

The average flow speed in the magnetosheath along the flanks of the magnetopause, tailward of ~4 R_V, is >90% of the upstream solar wind speed, and is directed along streamlines which are very nearly pointing in the -X-direction [Spreiter and Stahara, 1980]. For this study we will assume the tailward magnetosheath velocity near to the magnetopause from -8 to -12 R_V to be 440 km/sec. E_Z, therefore, is simply 440 × 3.5 = 1.54 [mV/m].

In the limit studied here, $v_Y \approx 0$ and equation 3.2 becomes simply $-v_X B_Y = 1.54$ [mV/m]. B_Y is approximately constant as a function of the Y location, varying by only ~±15%. Therefore, to within the accuracy of this derivation, the v_X and B_Y terms of this equation can be averaged separately over Y. This procedure yields the equation for the average tailward velocity

$$\langle v_X(X) \rangle_Y = \frac{-1540}{\langle B_Y(X) \rangle_Y} = \frac{-1540}{11.53 + .68X} \qquad (3.3)$$

where the velocity is given in km/sec, and X is in R_V. This function is plotted in Figure 3.16 from -8 to -12 R_V which is the range over which it is reasonably reliably determined.

Extrapolation of equation 3.3 outside the range over which our data set extends is problematic. The qualitative result, however, that tailward plasma motion near Venus is quite slow compared to the solar wind speed, is well determined. The deep tail region from -8 to -12 R_V is shown in this study to be an interesting transition region. Tailward of -8 R_V the average plasma velocity increases

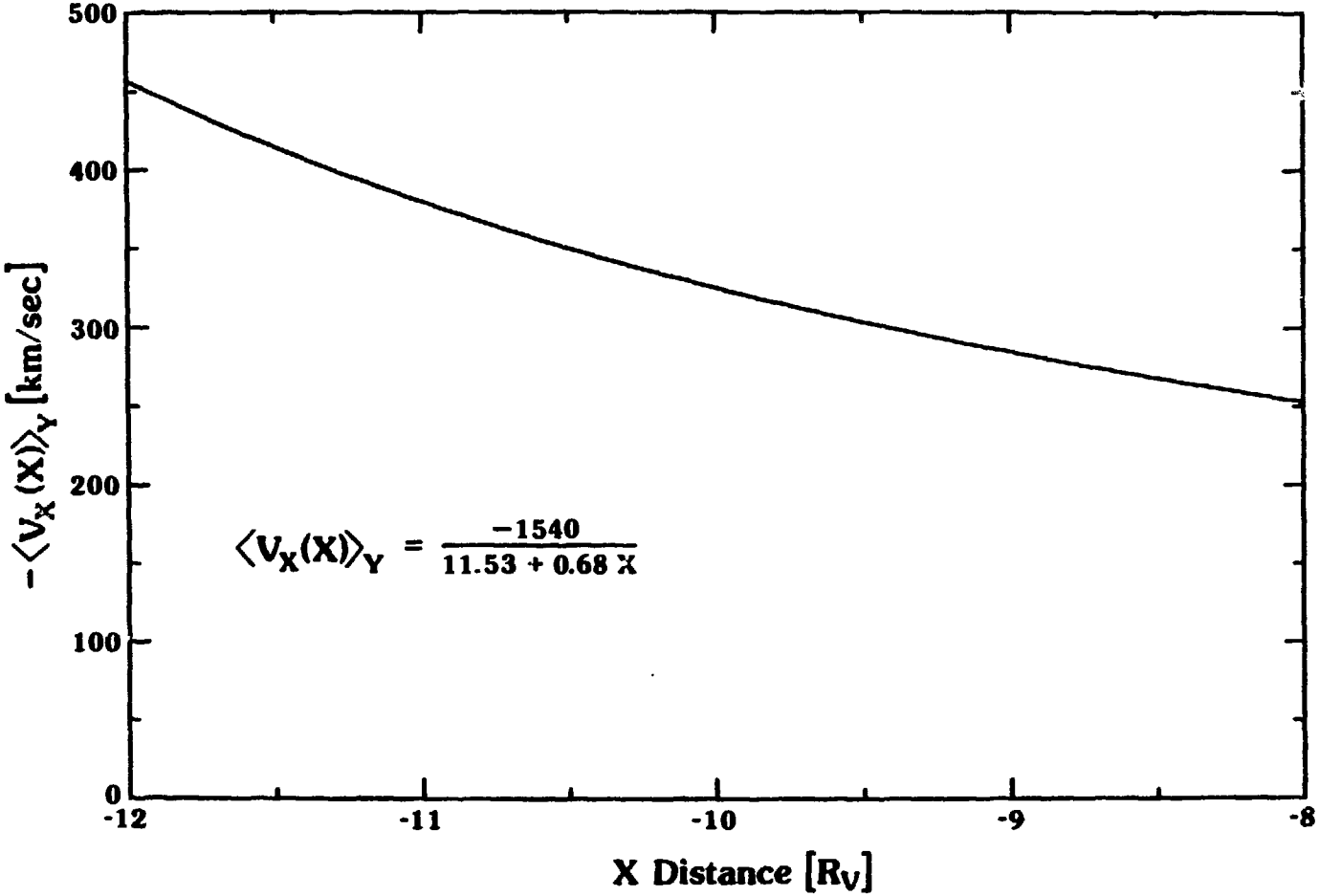

Fig. 3.16. The Y-averaged tailward plasma velocity, $\langle v_X(X)\rangle_Y$, as a function of downtail distance. Equation 3.3 describes this variation quantitatively. Venusward of -11.8 R_V, the flow is slower than the nominal solar wind speed, while beyond this distance the field lines are catching up with the nominally straight IMF configuration.

from about -250 km/sec to the solar wind speed of -440 km/sec at ~-11.8 R_V, and therefore the draped field throughout this portion of the tail continues to fall further behind the IMF. At -12 R_V the average plasma velocity is greater than the solar wind speed, and the field in this portion of the tail is in the process of catching up with the comparatively straight IMF configuration.

The steady state plasma acceleration is simply the spatial derivative $v_X \partial v_X/\partial X$. The Y-averaged spatial acceleration, $\langle v_X \partial v_X/\partial X\rangle_Y$, cannot be uniquely determined from equation 3.3; however, the product of the average terms in the acceleration gives

$$\langle v_X\rangle_Y \, \partial \langle v_X\rangle_Y/\partial X = \frac{-267}{(11.53 + .68X)^3} \tag{3.4}$$

in km/sec^2, where X is in R_V. This spatial acceleration is shown in Figure 3.17 from -8 to -12 R_V.

The precise plasma density distribution and temperature cannot be uniquely calculated from the average velocity and acceleration derived above. The approximate values of these quantities, however, can be calculated from the variations and the momentum equation. In the limit described in this study, equation 3.1 becomes

$$-J_Z B_Y = \rho (v_X \partial v_X/\partial X) \tag{3.5a}$$

$$J_Z B_X = \partial P/\partial Y \tag{3.5b}$$

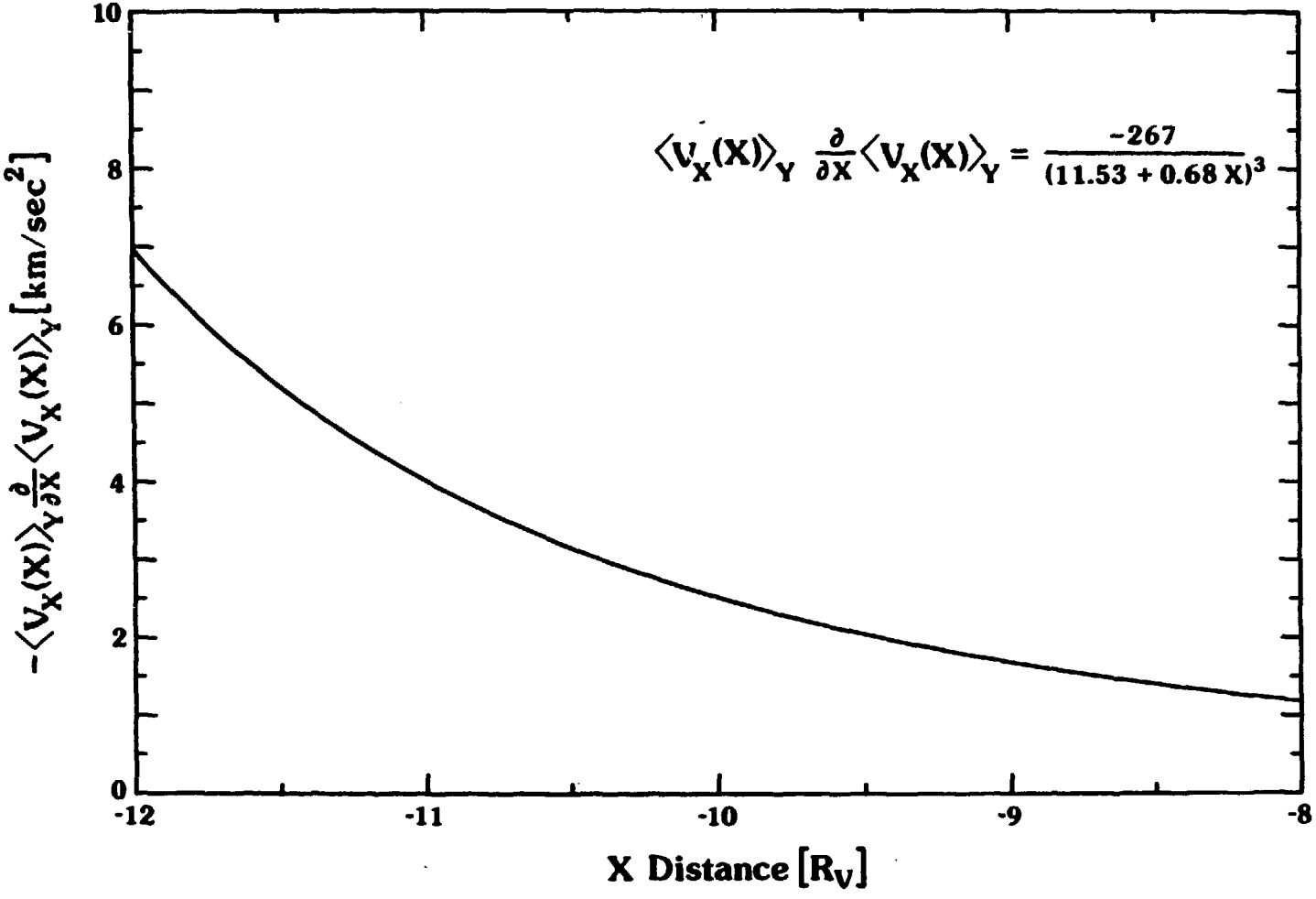

Fig. 3.17. The Y-averaged plasma acceleration $\langle v_X \rangle_Y \partial \langle v_X \rangle_Y / \partial X$ as a function of downtail distance. Equation 3.4 describes this variation quantitatively.

Insertion of the average field, currents, and plasma acceleration into equation 3.5a yields

$$\rho \simeq \frac{\langle -J_Z \rangle_X \langle B_Y \rangle_X}{\langle v_X \rangle_Y \partial \langle v_X \rangle_Y / \partial X} \tag{3.6}$$

By averaging the denominator of equation 3.6 over X, the remaining Y variation of the numerator then determines the gross Y variation of the density. Of course the plasma acceleration also varies as a function of Y; but, since the average plasma velocity is similar to the sheath velocity in this portion of the tail, the acceleration is probably not a strong function of Y. In addition, it must be remembered that these are only rough calculations, and that all terms cannot be fully treated with the average variation information gathered in this study. In the draped lobes the derived mass density is then $\sim 1.2 \times 10^{-22}$ kg/m^3 while the average derived mass density in the current sheet is $\sim 1.6 \times 10^{-21}$ kg/m^3. These values are equivalent to densities of approximately .07 and .9 protons/cm^3, respectively. If the plasma in the Venus tail is comprised of O^+, then the equivalent densities are .005 and .06 cm^{-3}.

These average values of the plasma density are in good agreement with the lack of observations of plasma in the Venus magnetotail by the PVO plasma analyzer [Intriligator et al., 1980]. This instrument was principally designed for solar wind observations and does not have the sensitivity to measure plasmas with densities of $\lesssim 1$/cm^3 [Saunders et al., 1985]. Since our derived average plasma

densities are lower than this cutoff, we would predict that the Venus tail would generally be indicated by a "plasma dropout" of the plasma analyzer. This is actually observed to be the case [Mihalov and Barnes, 1982]. When present, these observations usually show both O^+ and proton peaks in the spectra, but the spectra are almost never well enough formed to actually derive moments from. Even where it is possible to derive moments, these would represent unusual plasma conditions in the tail (perhaps high density and low flow speed) while our derived plasma properties are consistent with the average, steady state configuration of the tail.

The typical plasma temperature in the Venus tail can be derived from equation 3.5b by using the variation in the density which was just determined. We derive only the approximate plasma temperature averaged over this entire portion of the tail since the variations derived in this study are insufficient to determine gradients in the temperature. Averaging all terms in equation 3.5b and replacing $\partial P/\partial Y$ with $kT\ \Delta n/\Delta Y$, we solve for the temperature which gives

$$T \simeq \frac{\langle\langle J_Z\rangle_X\rangle_Y\langle\langle B_X\rangle_X\rangle_Y}{k}\frac{\Delta Y}{\Delta n} \qquad (3.7)$$

where k is Boltzmann's constant and Δn and ΔY are typical variations in density and Y location between the lobes and current sheet. equation 3.7 was numerically evaluated using $\langle\langle B_X\rangle_X\rangle_Y \simeq 10$ nT and the derived variation in the density between the draped lobes and the current sheet. If the tail is assumed to consist entirely of

hydrogen, then the proton temperature is of the order of 6×10^6K. If, on the other hand, the plasma is principally formed by O^+, then the ion temperature is of the order of 9×10^7K. These values represent upper bounds only since we have assumed that the electron pressure is negligible in this final portion of the derivation. If the electron temperature is comparable to or greater than the ion temperature, these values would be much reduced. In addition, successive steps in this derivation have required successively greater assumptions, and therefore these derived temperatures are the least well determined of our plasma parameters. We principally intend that they be used only as rough estimates. These values, however, are not so high as to be impossible to achieve in an induced magnetotail where ion pick-up may be important. O^+ picked-up by the unimpeded solar wind can have temperatures as high as $\sim 2 \times 10^8$K when they are picked-up with an initial perpendicular (thermal) velocity of the typical solar wind speed (440 km/sec).

Using the approximate plasma parameters derived above, the lobe and current sheet βs can be calculated. The plasma β in the lobe is $\sim .08$ which is consistent with the difference in the magnetic flux in the two lobes moving the current sheet from side to side, and with our assumption of low β lobes in the above derivation. The β in the current sheet, on the other hand, is ~ 12 which is consistent with our assumption of a high β current sheet in the derivation of these plasma parameters. The calculated gyroradii of protons and O^+ ions, calculated from these plasma moments, are $\sim .1$ and ~ 1.5 R_V in the current sheet, respectively, and only $\sim 30\%$ of that in the lobes.

Since these size scales are appreciably smaller than the width of the tail, our use of the fluid momentum equation in this derivation is vindicated.

The average plasma properties derived in this study can be used to determine the approximate average mass flux down the Venus tail which also represents an upper bound on the mass loss rate of Venus. For this rough calculation we assume that the current sheet and lobes each take up 1/3 of the cross-sectional area of the tail, which we assume to be circular and 5 R_V in diameter. At the average downtail distance of data in our data set (-10.8 R_V), equation 3.3 gives $\langle v_X \rangle_Y$ = -368 km/s. Multiplying this velocity by the sum of the current sheet and lobe densities times their respective cross-sectional areas, we calculate a downtail mass flux of $\sim 1 \times 10^{26}$ amu/s or $\sim 6 \times 10^{24}$ O^+/s. If all of the material in the Venus magnetotail is of planetary origin, then this value represents the approximate Venus mass loss rate. In any case, $\sim 1 \times 10^{26}$ amu/s represents an upper bound for the mass loss rate of the Venus atmosphere through tail formation.

3.5 Summary

This study began with the schematic diagram of the solar wind/IMF interaction with Venus displayed in Figure 3.1. We postulated that the IMF X-component could have an important effect on the internal structure of the draped magnetotail. In particular, variations of the X-component could cause the flapping of the current sheet from side to side within the tail consistent with the

magnetic pressure of the varying quantities of magnetic flux in the two lobes. We developed this chapter in three sections.

In Section 3.2 we demonstrated that magnetometer data ordered by spatial location is extremely variable. Both lobes and the current sheet can be found at all spatial locations within the tail, although there is a preference for the tailward pointing lobe on the +Y side and the Venusward pointing lobe on the -Y side. The average separation between the two lobes was shown to be offset toward the lobe which contains less magnetic flux. This observation, along with the high variability observed, confirmed our postulated importance of the IMF X-component. Clearly, what was needed to further advance the quantitative study of the Venus tail was to find a coordinate system which measures locations with respect to the internal tail structures themselves.

In Section 3.2 we also showed that magnetic reconnection is a small effect in the central Venus tail, and that the magnetic field strength in the tail, referenced to the average magnetosheath value immediately adjacent to the tail, at the points in each orbit where the PVO pierces the magnetopause, is strongly correlated with the magnetic field draping angle. In the lobes the field points roughly tailward and Venusward, and the relative field strength is large. In the lobe separating current sheet, on the other hand, the field points roughly across the tail and the relative field strength is comparatively small. We used this correlation to construct a coordinate system which statistically locates data with respect to the tail current sheet itself.

In Section 3.3 we actually constructed this coordinate system and measured the average variations of the field components for the first time. The B_X-component was demonstrated to smoothly vary from strongly Venusward on the far -Y side of the tail, through zero in the center of the current sheet, to strongly tailward on the far +Y side of the tail. The B_{Y*}-component, on the other hand, showed a two-humped distribution across the tail and decreased fairly linearly with distance from the planet. From these variations we drew the average draping pattern in the deep Venus tail in Figure 3.12 and derived the average cross tail current density distribution. Knowledge of the average magnetic fields and self-consistent currents made it possible to calculate the electromagnetic $\underset{\sim}{J}\times\underset{\sim}{B}$ forces and examine the average consistent plasma properties of the tail.

In Section 3.4 we used the continuity of the tangential electric field and found field variations to derive the average tailward velocity and acceleration as functions of downtail distance. The tailward velocity was shown to vary from ~-250 km/sec at -8 R_V to ~-470 km/sec at -12 R_V. From the derived accelerations, the calculated $\underset{\sim}{J}\times\underset{\sim}{B}$ forces, and the MHD momentum equation, we calculated the approximate plasma densities in the current sheet and lobes, and very approximate average plasma temperature. The current sheet density was shown to be ~.9 p^+/cm^3 (.06 O^+/cm^3) while the lobe density was approximately 15% of that. These densities were shown to be consistent with the general lack of PVO plasma observations in the tail. If the tail plasma is composed purely of hydrogen, then

we calculate an average, approximate, maximum ion temperature is $\sim 6 \times 10^6$ K; while if it is composed essentially of oxygen, this temperature is $\sim 9 \times 10^7$ K. Finally, we calculated the mass flux in the tail which is $\sim 1 \times 10^{26}$ amu/s. This value represents an upper bound for the mass loss rate of the Venus atmosphere through tail formation.

While this study derives many previously unknown average quantities of the deep Venus magnetotail, and sets, for the first time, the average magnetic field draping pattern, self-consistent currents and forces, and approximate inferred plasma properties of this region, it should not be thought of as an end to the study of the deep Venus magnetotail. Rather, a powerful analysis tool has been developed for examining the detailed physics of this region by referencing the location of not just magnetic field data, but all PVO data, with respect to the internal tail structures themselves. Finally, our method may be very valuable in examining the magnetotails of other mass loading obstacles in the solar wind, such as comets, and the deep (reconnected) terrestrial magnetotail, since the orientation of the upstream IMF should also have a strong influences on these regions.

3.6 Chapter Acknowledgments

We gratefully acknowledge valuable discussions with D. N. Baker, R. C. Elphic, J. G. Luhmann, W. I. Newman, J. L. Phillips, G. L. Siscoe, and D. T. Young. We also gratefully acknowledge valuable constructive critiques from J. R. Spreiter and

another (anonymous) referee. The magnetic field data used in this study and work done at the IGPP, UCLA were supported under NASA contract NAS2-9491. One of the authors (H.E.S.) was supported by the Office of Naval Research, while another (M.A.S.) was supported by an ESA Research Fellowship. The principal author and work done at Los Alamos were supported by Los Alamos National Laboratory under the auspices of the United States Department of Energy.

CHAPTER 4

The Giacobini-Zinner Magnetotail

Tail Configuration and Current Sheet

4.0 Chapter Overview

The high resolution plasma electron and magnetic field data sets from the ICE tail traversal of Comet Giacobini-Zinner have been combined to make a detailed study of the draped G-Z magnetotail in general, and its field reversing current sheet in particular. The geometry of the magnetotail at the time of the ICE crossing is determined, and is shown to be consistent with a circular tail cross-section rotated 10.5^{o} in the normal sense of aberration and 9.9^{o} above the ecliptic plane, bisected by a cross tail current sheet which is rotated 43^{o} out of the ecliptic about the solar wind velocity vector. MHD continuity, momentum, and energy equations are combined with the plasma and field observations to determine unmeasured plasma properties at ICE and upstream at the average point along each streamline where the cometary ions are picked-up. The ion temperature, beta, and flow speed at ICE range from 1-1.5 $\times$ 10^{6} K, 1-4, and -20 to -30 km/sec, respectively, in the draped lobes to ~1.2 $\times$ 10^{5} K, up to ~40, and ~-20km/sec in the current sheet. Upstream at the average pick-up locations, the flow velocity, ion temperature, density, and ion source rates range from ~-75 km/sec, ~4 $\times$ 10^{6} K, ~20/cm^{3}, and ~1.5/cm^{3}/sec in the regions

upstream from the lobes to ~-12 km/sec, ~1 × 10^5 K, 200 - 600 /cm^3, and ~3.6 /cm^3/sec in the prime mass loading region upstream from the current sheet. Gradients in the plasma properties at the edges of this region are quite strong, and the diameter of the region is ~1500 km, in good agreement with the expected size scale of the cometary ionopause; implications of our inferred plasma properties in this region are examined. The derived and measured flow velocity and measured plasma density at ICE are combined to calculate the transport rate of ions past the plane of the ICE encounter, and we calculate that ~2.5-5 × 10^{28} ions/sec (neutrals/sec in the steady state) are produced by the comet with only ~1% of these traveling down the magnetotail.

4.1 Introduction

Man has observed apparitions of comets and visible comet tails over many millennia and wondered about their origin. Three and one half decades ago Biermann [1951] postulated the first modern scientific explanation of visible cometary tails, namely that they are caused by the interaction of an ionized gas of solar origin (the then unknown solar wind) with the comet. Alfvén [1957] then introduced the concept of magnetic field draping as an important aspect of the physical process for comet magnetotail formation. Since that time much work has been done on refining the understanding of the solar wind interaction with comets in general, and the formation of cometary tails in particular, and insights into the nature of the solar wind interaction with comets have become

highly refined (see reviews by Brandt [1982], Ip and Axford [1982], and Mendis and Houpis [1982], and references therein).

During the past year the first in situ observations of comets have been made so that actual measurements are finally available for detailed analysis. On September 11, 1985 the International Cometary Explorer (ICE) spacecraft traversed Comet Giacobini-Zinner (G-Z) 7800 km downstream from the nucleus. More recently, observations have been made at Comet Halley by the Giotto, Sakigake, Suisei, and two Vega spacecraft. However, all of the Halley encounters occurred along trajectories upstream from the cometary nucleus. While these various Halley encounter data sets are already proving to be invaluable in further unravelling many of the mysteries of the detailed interaction of the solar wind with cometary bodies, none can directly address the most noticeable element of cometary apparitions: the visible ion tail. The ICE data, therefore, provides a unique opportunity for the detailed in situ examination of a cometary magnetotail.

A number of recent studies have discussed various aspects of the ICE magnetotail data. Papers in the special issue of Science by Bame et al. [1986], Smith et al. [1986], and Meyer-Vernet [1986a] describe the global variations observed throughout the ICE encounter interval by the plasma electron, magnetometer, and radio wave experiments, respectively. More detailed analyses of these three data sets have been carried out by Zwickl et al. [1986], Slavin et al. [1986a], and Meyer-Vernet [1986b], respectively. Finally, Siscoe et al. [1986] combine approximate field and plasma values for

four locations across the tail in order to derive approximate values for certain unmeasured plasma properties such as the ion pick-up speed. In the present paper we combine all three data sets at their highest time resolutions in order to make detailed analyses of the Giacobini-Zinner magnetotail.

Magnetic field data on ICE were obtained by the Jet Propulsion Laboratory magnetometer [Frandsen et al. 1978], which provided three orthogonal vector measurements every 1/3 second during the ICE encounter. Plasma electron measurements on ICE are supplied by the Los Alamos plasma analyzer [Bame et al. 1978] and certain electron moments can be derived from the radio noise spectrum measurements of the Observatoire de Paris/GSFC radio wave experiment [Knoll et al. 1978]. At the ICE encounter telemetry rate, the Los Alamos electron spectrometer measures the full two-dimensional electron distribution function (integrated over $\pm 65^{o}$ about the equatorial plane) in one spacecraft rotation (3 seconds) once every 24 seconds. The derivation of electron density and temperature from the radio wave experiment data stems from plasma noise spectroscopy, and has been described in detail by Meyer-Vernet [1986a]. This experiment provides measurements at intervals which vary from 3 to 18 seconds and such measurements are aliased in time over variable intervals, ranging from 1.5 to 18 seconds. In addition, the electron spectrometer, which was designed to measure the solar wind from a halo orbit at the earth's L1 point, has a minimum energy level of $\sim$10 eV except when taking data in a special photoelectron mode. This means that the distribution functions of the highest density

and lowest temperature plasma in the center of the magnetotail current sheet cannot be fully determined. The radio experiment, on the other hand, is most accurate for these colder, more dense plasmas. Since 1) the density ranges from about $50/cm^3$ to over $650/cm^3$ and electron energies range from ~1 eV to ~ 10 eV, 2) variations in the field and plasma properties occur on time scales which range from a fraction of a second to a few minutes, and 3) the electron and field properties are inexorably linked, the three data sets combined in this study are highly complementary.

In this study these complementary data sets are combined to make detailed analyses of the configuration and properties of the Giacobini-Zinner magnetotail. We develop this study in sections. In the next section (4.2) the global interaction of the solar wind and embedded interplanetary magnetic field (IMF) with the comet is described as it pertains to magnetotail formation. The extrapolated solar wind flow direction and magnetotail entry, exit, and current sheet crossing times are used to determine the location and dimensions of the tail, and these results are combined with the average magnetic field draping direction to infer the internal tail structure. In Section 4.3 the pressure balance and plasma acceleration conditions are derived from the MHD equations, and their implications for the plasma properties further upstream in the region near to the comet nucleus are discussed. In Section 4.4 the particle flux is integrated over the magnetotail for the entire cometary encounter, and these results are used to determine the importance of comet tail formation for the removal of the ionized

cometary efflux. Finally, in Section 4.5, the implications of the various properties derived in this study are examined, particularly with regards to the upstream near- nucleus region where the tail formation process occurs.

4.2 Tail Formation and Topology

The basic physical processes responsible for cometary magnetotail formation are slowing of the solar wind flow by mass addition from the extended cometary atmosphere and the consequent draping of the interplanetary magnetic field about the cometary obstacle. The solar wind essentially flows radially outward from the sun carrying with it an embedded interplanetary magnetic field (IMF). As the flow nears the comet nucleus it becomes slowed and significantly mass loaded. This mass loading process is an integrated effect in that the density of cometary ions at any location is a function of the total mass addition along the streamline sunward from the observation location. Conductivity of the ionopause boundary itself at least partially excludes the magnetic field from the region immediately surrounding the nucleus, and thereby serves to divert the flow around the obstacle. Less mass is added to the flow along streamlines which pass progressively farther from the comet nucleus since the neutral cometary material available for ionization drops off as a function of radial distance.

Since the magnetic field links the regions of greater and lesser slowing, the field becomes draped about the cometary obstacle. The magnetic field in the region of greatest integrated

mass addition, and therefore slowest flow, becomes highly bent and forms the field reversing, cross tail current sheet in the cometary magnetotail. The field in regions of progressively less mass addition, and therefore greater flow speed, immediately adjacent to the current sheet becomes highly draped into the sunward and antisunward directions, forming the tail lobes on either side of the current sheet. The narrow, high density current sheet within the cometary magnetotail is also probably the region observed from earth as the visible ion tail. Slavin et al. [1986b] have compared the ICE data and ground based observations and show that there is good agreement between the highest density region measured at ICE and the brightest region observed from the earth.

The top panel of Figure 4.1 shows a schematic representation of the draped magnetic field configuration about G-Z projected into the plane defined by the average upstream magnetic field and solar wind flow vectors. For simplicity this figure is drawn for an IMF which has no X-component. While the X-component modifies the relative sizes of the two draped tail lobes in the deep Venus magnetotail [McComas et al. 1986a], and also probably at comets, the fundamental draping process only involves the component of the field perpendicular to the plasma flow direction.

In the magnetotail formation process just described, the orientations of the solar wind velocity vector and upstream magnetic field clearly play important roles in ordering the magnetotail location and internal configuration. The most reasonable coordinate system for studying the G-Z magnetotail is, therefore, based on

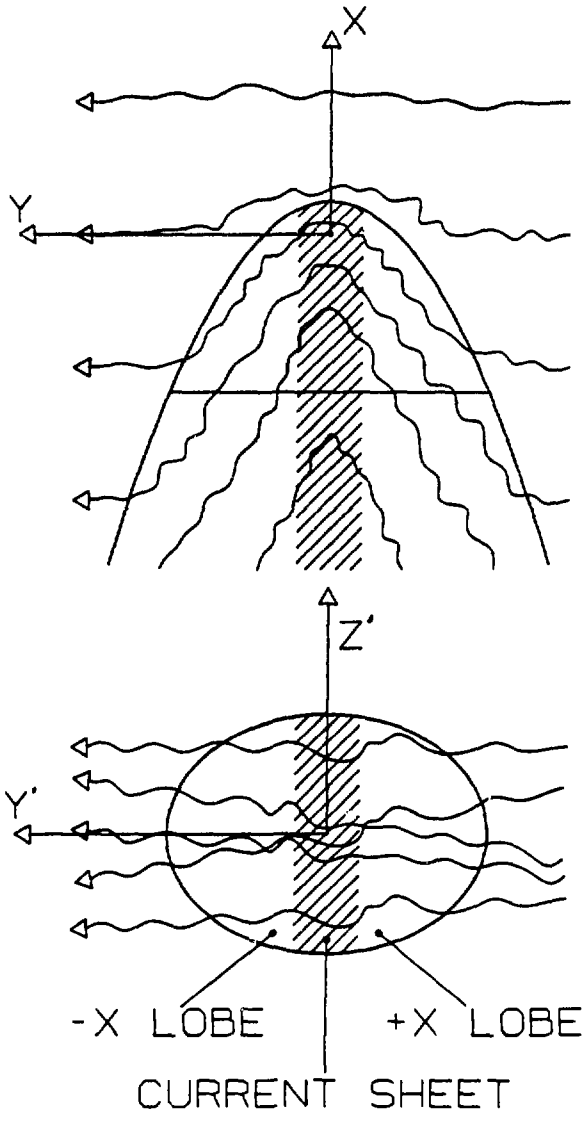

Fig. 4.1. Schematic diagram of the draped magnetic field configuration in the Giacobini-Zinner magnetotail projected into the Y'-X and Y'-Z' planes. The X axis is defined to be antiparallel to the average solar wind flow direction for the crossing while the Y' axis is defined to be parallel to the average magnetic field direction in the plane perpendicular to the flow. Waves associated with pick-up instabilities cause the accreted field in the tail to be highly kinked and the field orientation in the tail to be quite variable as a function of location and time. Nonetheless, these variations do not stop the formation of the global tail structures such as the current sheet (cross hatched), two tail lobes, and magnetotail boundary (solid smooth curves). The horizontal line in the top panel indicates the location of the cut through the tail represented by the elliptical tail cross section (see text) drawn in the bottom panel.

these directions. In the coordinate system used in this study (denoted the X-Y′-Z′ system) the solar wind velocity vector is aligned antiparallel to the X-axis. The Y′-axis is aligned with the average magnetic field vector crossing the tail in the plane perpendicular to the X-axis. Finally, the Z′-axis completes the right-handed coordinate system, and lies in the plane of the current sheet since this plane is perpendicular to the primary curl of the field lines (in the X-Y′ plane). The lower panel of Figure 4.1 is a schematic representation of the magnetic field projected into the Y′-Z′ plane. Portions of the instantaneous field in this plane may point in directions very different from the average, Y′, direction. These variations are caused both by fluctuations in the field in space and time due to upstream waves and instabilities associated with the cometary ion pick-up process, and actual rotations of the upstream IMF. It is still, however, the global, average magnetic orientation which dominates the essential tail structure.

One of the important new results from the G-Z encounter is the large amount of plasma [Bame et al., 1986; Gosling et al., 1986] and field [Smith et al., 1986, Tsurutani and Smith, 1986a and b] turbulence associated with the extended cometary ion pick-up region. These fluctuations cause intense kinking of the field and large spatial variations of the plasma properties. In Figure 4.1 we attempt to show the effect of these variations on the magnetotail. Since the flow is substantially slowed and compressed within the magnetotail, upstream variations along streamlines passing near the stagnation region also become compressed and incorporated into the

magnetotail fine structure. This process probably accounts for much of the variability observed within the tail, particularly in the high time resolution measurements.

There was no spacecraft upstream from G-Z to monitor the solar wind and IMF conditions during the ICE encounter. In this study, therefore, we use extrapolated solar wind observations from the inbound and outbound portions of the ICE encounter to infer the solar wind conditions at the time of the ICE crossing. Nine point running averages of the plasma flow speed and flow angle (as measured from the GSE -X-axis toward the GSE -Y-axis) are plotted in Figure 4.2 for the entire ICE encounter interval. No data are shown in the central portion of the crossing were the flow speed dropped below 30 km/s, the minimum bulk flow speed which can be reliably determined by the Los Alamos plasma electron spectrometer. The dashed lines indicate the inferred variations of the two solar wind parameters in the absence of the cometary interaction. The best extrapolated values for the solar wind speed, v_{SW}, and flow angle, ϕ, during the tail traversal, at approximately 1100 UT, are $v_{SW} = 460$ km/s and $\phi = -10.5^{o}$. The X-axis used in this study is, therefore, first rotated through an angle of 10.5^{o} from the GSE X-axis so as to be antiparallel to the projection of the solar wind velocity vector in this plane.

If the tail cross-section is circular at the downstream distance of the ICE traversal, then the average orientation of the tail at the time of the ICE crossing can be determined. Figure 4.3 shows the geometry under the simplifying assumption of a circular

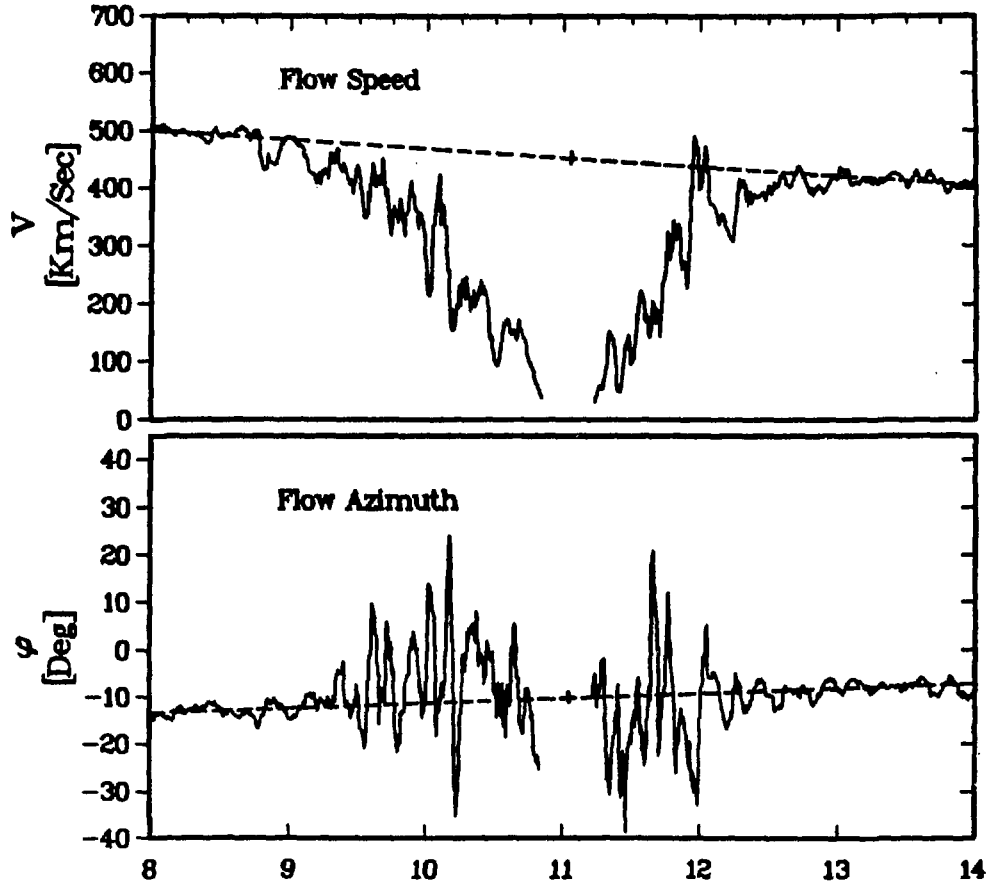

Fig. 4.2. Nine point running averaged flow speed and flow angle for the entire ICE traversal of Comet Giacobini-Zinner. No data are shown in the central portion of the tail where the determination of these parameters from the electron distribution functions is unreliable (flow speeds <30 km/s). The flow azimuth is measured positive from the solar ecliptic (SE) -X direction toward the SE -Y direction, and therefore a value of -4° is consistent with the nominal aberration angle. The dashed lines show interpolations of the upstream solar wind flow values across the tail. Since there was no upstream monitor for the ICE traversal, these extrapolations are used to provide approximate upstream conditions. Vertical tics at ~11:03 indicate the center of the tail crossing.

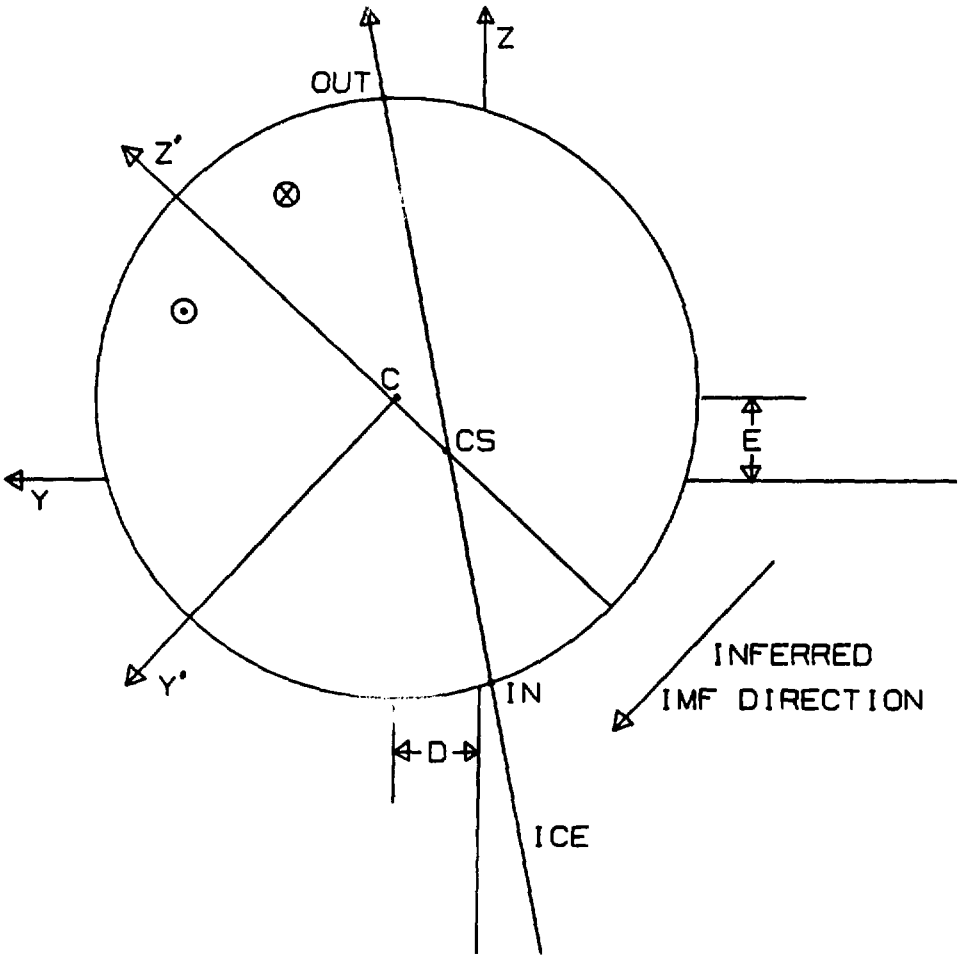

Fig. 4.3. Schematic representation of the ICE tail crossing geometry. The points labeled IN, CS, and OUT are the inbound lobe, current sheet center, and outbound lobe crossings along the ICE trajectory. Point C indicates the inferred center of the tail assuming that the tail is aberrated a distance D which corresponds to an angle of 10.5° at 7800 km, and that the tail cross section is circular. The orientation of the Z' axis (the current sheet) is independently inferred from the average field orientation through the tail (see text); interestingly, the inferred tail center, C, lies very close to the Z' axis.

cross-section. Points "IN" and "OUT" are the tail entry (10:59:40 UT) and tail exit (11:07:40) as given by Slavin et al. [1986a] while "CS" is the current sheet center (11:02:50 UT) as determined in this study. The GSE Y offset distance of the center of the tail, D, is simply the downtail distance of the crossing, 7800 km, multiplied by the tangent of 10.5^{o}, or 1450 km. Given points IN and OUT on the circle, and that the center must lie at a GSE Y value of 1450 km, the GSE Z offset of the tail, E, can be found. This offset is 1360 km, which corresponds to a solar wind flow directed 9.9^{o} above the ecliptic. Flow angles of $\sim 10^{o}$ are unusual for the solar wind both within and out of the ecliptic plane. For this crossing, however, they may be attributable to the stream/stream interaction observed by ICE between 04:00 and 06:00, just prior to the comet encounter. The ICE spacecraft traverses the tail slightly off-center in this geometry, and the tail diameter is, therefore, slightly larger than the crossing interval would indicate. The tail diameter derived by this technique is 10,100 km. If the cross tail current sheet bisects the tail, then it must pass not only through point CS, but also through the tail center. This gives a current sheet orientation which is rotated 47^{o} out of the ecliptic plane.

This current sheet orientation compares quite favorably with the results derived from other more direct methods. Minimum variance analysis of the field rotation through the current sheet yields an angle between the ecliptic and the current sheet of 43^{o} [Slavin et al., 1986a], which is in good agreement with the

direction expected from the average upstream orientation extrapolated from the ICE observations. Remote sensing of energetic ion gyromotions by Daly et al. [1986] independently determines the average field orientation, and gives a current sheet inclination of 46^{o}. All of these average results are in excellent agreement given the large amount of variability of the local field measurements, as indicated schematically in Figure 4.1. For the remainder of this study we assume that the angle between the current sheet and the ecliptic plane is 43^{o}. The angle between the ICE trajectory and the current sheet, in the Y-Z plane, is then 35^{o}.

It is interesting that the geometry derived under the circular cross-section assumption independently yields a current sheet inclination within only 4^{o} of that derived directly from the field observations. The assumption of a circular tail cross-section, however, is rather ad hoc since the physical process responsible for determining the tail width is different for directions parallel and perpendicular to the current sheet. In the parallel (Z') direction, the width should be a direct measure of the effective size of the prime mass loading region. The width in the perpendicular (Y') direction, on the other hand, is governed by the draping configuration and flaring angle of the tail lobes as well as the downtail distance of the observations. These considerations assume that the external pressure surrounding the tail is isotropic, as suggested by Siscoe et al. [1986]. If there is sufficient flow so that the ram pressure component is still important along the tail boundary, then this force acts to circularize the tail since it is a

strong function of the flaring angle. For this study we will assume that the crossing geometry is correctly described by Figure 4.3. We have also examined the data under other reasonable geometry assumptions, and find that the results described here are not particularly sensitive to the exact configuration.

The basic combined data set used in this study is shown in Figure 4.4, and contains data from 10:59 to 11:09 UT. The high resolution magnetic field data (light lines) have been averaged (heavy lines) over 3 and 18 seconds centered on the Los Alamos and Observatoire de Paris plasma observations, respectively. In this manner the field and plasma measurements correspond to the same averaging intervals and can be directly compared. Los Alamos plasma data have not been used for the seven points near the center of the tail where the plasma moments are unreliably determined due to observational limitations. Obvious fluctuations between plasma values derived with the two techniques have been intentionally included elsewhere since both are presumed to be accurate in those regions, and the variations therefore give some indication of the reliability of the values.

4.3 MHD Equilibrium

In this section we combine the ICE plasma and magnetic field observations with the MHD continuity, momentum, and energy equations to calculate certain unmeasured plasma ion properties at the ICE location and infer some of the conditions upstream along streamlines where substantial mass is being added to the flow. Neglecting terms

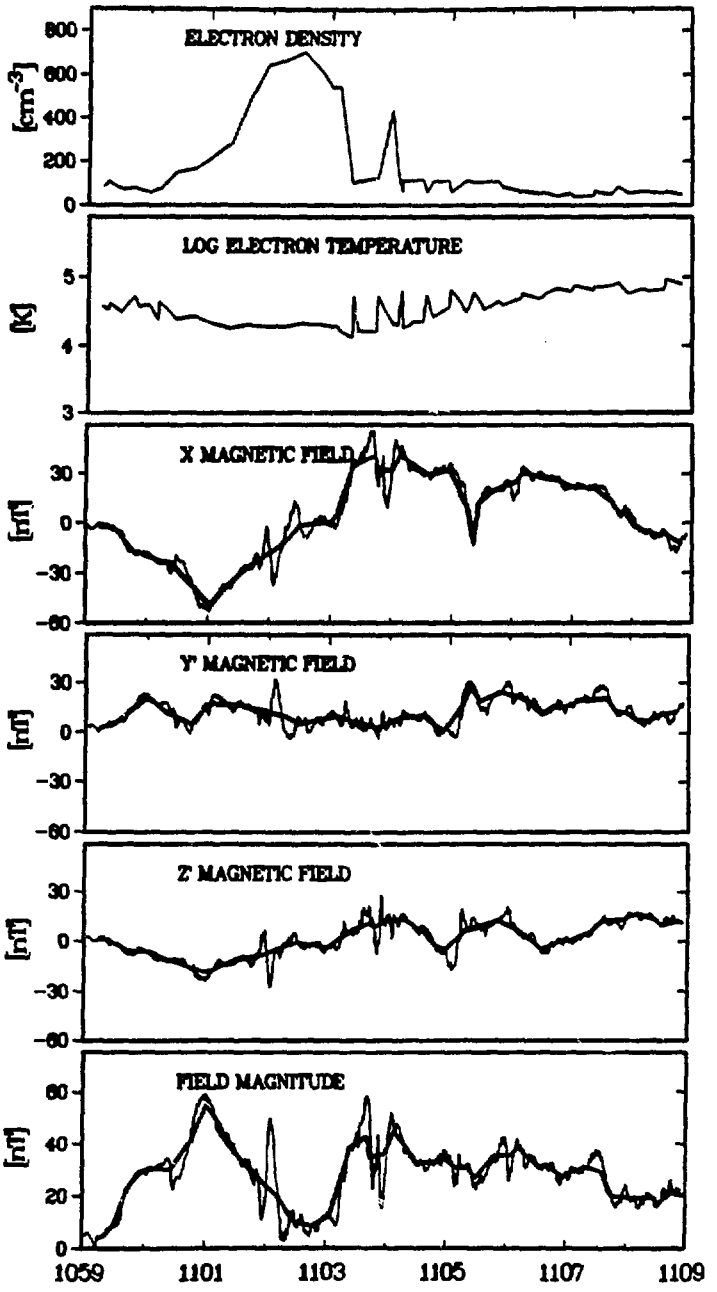

Fig. 4.4. Combined data set used in this study. Electron density and temperature are independently derived from the Los Alamos plasma electron and Observatoire de Paris radio wave data sets. Jet Propulsion Laboratory magnetometer data are shown in the bottom 4 panels in high time resolution (light lines) and averaged over the corresponding plasma measurement intervals (heavy lines).

due to gravity and following the development of Siscoe [1982], the MHD continuity, momentum, and energy equations are written in conservation form

$$\frac{\partial \rho}{\partial t} + \nabla \cdot (\rho \vec{v}) = S^* \tag{4.1}$$

$$\frac{\partial}{\partial t} (\rho \vec{v} + \varepsilon_o \mu_o \vec{I}) + \nabla \cdot (\tilde{\tilde{P}} + \rho \vec{v}\vec{v} - \tilde{\tilde{T}}) = 0 \tag{4.2}$$

$$\frac{\partial}{\partial t} (\frac{1}{2} \rho v^2 + U + \frac{\varepsilon_o}{2} E^2 + \frac{1}{2\mu_o} B^2) +$$

$$\nabla \cdot [(\frac{1}{2} \rho v^2 + U + \tilde{\tilde{P}}) \cdot \vec{v} + \vec{q} + \vec{I}] = 0 \tag{4.3}$$

where ρ is the plasma mass density, $\vec{v}$ is the plasma velocity, U is the internal energy, $\tilde{\tilde{P}}$ is the plasma pressure tensor, $\vec{q}$ is the heat flux, $\vec{I}$ is the Poynting vector, $\tilde{\tilde{T}}$ is the Maxwell stress tensor, $\vec{E}$ and $\vec{B}$ are the electric and magnetic fields, and ε_o and μ_o are the permitivity and permeability of free space. The mass density source term, S^*, in the continuity equation (4.1) represents the addition of pick-up ions to the plasma by processes such as photoionization

and charge exchange, and may be a very complicated and largely unknown function of both location and time.

The right-hand sides of equations 4.2 and 4.3 are identically zero only if particles are picked-up from being initially at rest. Otherwise, the momentum and energy source terms (right-hand sides of equations 4.2 and 4.3) are $S^*\tilde{w}$ and $\frac{1}{2}S^*w^2$, where $\tilde{w}$ is velocity of the neutral flow which is being ionized or charge exchanged, and picked-up by the flowing plasma. Typically, $|\tilde{w}| \lesssim 1$ km/sec; therefore, ignoring the neutral flow's contributions to the momentum and energy densities is justifiable if pick-up velocities are appreciably greater than 1km/sec and charge exchange is ignored. The flow velocities at the time of pick-up calculated later in this section will be shown to be consistent with this condition across the tail.

The divergence of the Maxwell stress tensor and Poynting vector terms from equations 4.2 and 4.3 can be rewritten

$$\nabla \cdot \tilde{\tilde{T}} = \varepsilon_o \mu_o \frac{\partial \tilde{I}}{\partial t} + \rho_c \tilde{E} + \tilde{J} \times \tilde{B} \tag{4.4}$$

and

$$\nabla \cdot \tilde{I} = -\tilde{E} \cdot \tilde{J} - \frac{\partial}{\partial t}\left(\frac{\varepsilon_o}{2} E^2 + \frac{1}{2\mu_o} B^2\right) \tag{4.5}$$

where ρ_c is the charge density. For the draped magnetotail field geometry described in the previous section, the Y'- and Z'-axes were

defined such that the average magnetic field vector lies in the X-Y′ plane. In such a coordinate system the average Z′-directed magnetic field is zero, and variations of the field and plasma properties should be principally functions of X and Y′. Consequently it is justifiable to make the approximations: $\partial/\partial Z' = 0$ and $B_{Z'} = 0$. Another characteristic of an X-aligned magnetotail configuration is that $\partial B_X/\partial Y' \gg \partial B_{Y'}/\partial X$ throughout most of the tail. McComas et al. [1986a] demonstrate this point, for example, for the Venus magnetotail, which is also formed by mass loading and magnetic field draping of the solar wind and IMF. Including these simplifications, the cross tail current density, $\tilde{J}$, can be rewritten

$$\tilde{J} \approx J_{Z'}\,\hat{Z}' \approx \frac{-1}{\mu_o}\frac{\partial B_x}{\partial Y'}\,\hat{Z}' \qquad (4.6)$$

which is expressed purely in terms of measured quantities.

The plasma electron and field data available from the single ICE tail traversal are clearly insufficient to determine fully all terms in equations 4.1-4.3. Fortunately, these equations can be simplified substantially by making suitable approximations, and the approximate force balances within the tail can be determined. In the pressure term, we assume that the picked-up electrons and ions have had sufficient time to isotropize. For the electrons, at least, this assumption is consistent with observations (e.g., Bame et al. [1986]). Using this assumption, the divergence of the pressure tensor can be replaced with the gradient of a scalar

pressure, which is simply the sum of the electron and ion pressures, $P = n_e kT_e + n_i kT_i$ where k is Boltzman's constant. The internal energy of an isotropic plasma is, then, $U = (3/2)P$. We further assume that the plasma remains electrically neutral, $\rho_c = 0$, and that the heat flux is negligible within the tail, $\vec{q} = 0$. Finally, we assume that the plasma flows everywhere antiparallel to the X-axis, $\vec{v} = v_X \hat{X}$, in accordance with global MHD simulations by Fedder et al. [1986] which show that there is only very slight deflection of the plasma flow throughout the global cometary interaction. This assumption cannot be precisely true for streamlines which are diverted about the conductive ionosphere, however, such diversion only slightly increases the streamlines' path lengths compared to the distance back to ICE, and some such assumption is required to make the equations tractable with the limited ICE data available. In the MHD hydromagnetic limit $\tilde{E} = -\tilde{v} \times \tilde{B}$, which under the above assumptions becomes $\tilde{E} = -v_X B_Y \hat{Z}$. Combining equations 4.4-4.6 with equations 4.1-4.3, inserting these simplifications, and solving for the steady state solutions yields the greatly simplified MHD equations

$$\frac{\partial}{\partial X} (\rho v_X) = S^* \tag{4.7}$$

$$\frac{\partial}{\partial X} (\rho v_X^2 + P) = -B_Y J_Z \tag{4.8a}$$

$$\frac{\partial}{\partial Y'}(P) = B_X J_{Z'} \tag{4.8b}$$

$$\frac{\partial}{\partial X}\left(\frac{1}{2}\rho v_X^3 + \frac{5}{2}Pv_X\right) = -v_X B_{Y'} J_{Z'} \tag{4.9}$$

where equation 4.7 explicitly describes the addition of mass to the plasma flow, equations 4.8a and 4.9 describe the tailward acceleration of the plasma, and equation 4.8b describes the pressure balance across the tail.

Since $J_{Z'}$ is simply the derivative of B_X with respect to Y', as given in equation 4.6, equation 4.8b can be rewritten in the more common pressure balance form

$$nk(T_i + T_e) + \frac{B_x^2}{2\mu_o} = P_T \tag{4.10}$$

for singly ionized ions where P_T is the total pressure across the tail, a constant at any given X distance downtail. In the pressure balance condition described by equation 4.10, all quantities on the left-hand side are measured throughout the ICE tail traversal except the average ion temperature, T_i. In order to calculate T_i as a function of location across the tail, we must first determine P_T at the downtail distance of the ICE traversal. Siscoe et al. [1986] argued that the tail pressure is approximately the stagnation

pressure of the solar wind since the plasma pressure at the comet essentially stands off the solar wind flow. Here, we improve this argument to include the effects of the residual plasma flow within the near comet environs.

At any near comet location the local plasma and field pressures must stand off the difference between the upstream and the local dynamic pressures in order to be in equilibrium. Since the electromagnetic term in equation 4.8a is the X derivative of some (possibly unknown) function, it can thereby be absorbed into the X derivative, along with the plasma pressure, on the left-hand side of the equation. Integrating this equation along a streamline (fixed Y' and Z' values) yields

$$P_c = \rho_{sw} v_{sw}^2 - \rho_c v_c^2 \qquad (4.11)$$

where P_c represents an isotropic pressure due to both the plasma and field, and ρ_c and v_c are the mass density and velocity assuming that all three quantities are taken at a single location within the comet. The upstream solar wind plasma and field pressures are only a few percent of the solar wind ram pressure ($\rho_{sw} v_{sw}^2$), and are ignored in this equation.

Equation 4.11 holds for the pressure on the external surface of the magnetotail so that $P_c = P_T$ and all quantities in equations 4.10 and 4.11 are measured except for T_i. The solar wind electron density just prior to the ICE fly-through was ~5 /cm^3, and just after was ~7 /cm^3 so that we use $n_{sw} = 6 \pm 1 \times 10^6$ /m^3. The

electron density at the magnetotail boundary, at the location of the ICE entry and exit, is $n_c = 75 \pm 25 \times 10^6/m^3$, and we assume that the typical pick-up ion has a mass of 18 amu (water group) as indicated by the results of Ogilvie et al. [1986], and Zwickl et al. [1986]. The solar wind velocity extrapolated from the top panel of Figure 4.2 is $v_{sw} = 460 \pm 25$ km/s. The plasma velocity at the tail boundary is less than the Los Alamos measurable minimum value of 30 km/s, and for the purposes of this calculation we use $v_c = 20 \pm 10$ km/s which will be shown to be a reasonable value later in this section. Inserting all these values into equation 4.11, the most probable total tail pressure at the ICE crossing is $P_T = 1.2 \times 10^{-9}$ N/m^2 with an upper bound of 2.6×10^{-9}, and a negative (unphysical) lower bound. The value used by Siscoe et al. [1986] was $\sim 2.5 \times 10^{-9}$, a factor of two greater than the most probable value calculated here.

The measured plasma electron pressure is displayed in the top panel of Figure 4.5. The pressure maximizes in the central region of the current sheet, and is relatively constant throughout the two tail lobes. The cross tail component of the magnetic field pressure, $B_X^2/2\,\mu_o$, is displayed in the third panel of the figure. The field pressure varies in a manner generally opposite to the plasma electron pressure minimizing in the cross tail current sheet and maximizing in the portions of the lobes immediately adjacent to this sheet. Inserting $P_T = 1.2 \times 10^{-9}$ N/m^2 into equation 4.10, and using these two measured pressure variations, we calculate the variation of T_i across the tail traversal. The second panel of

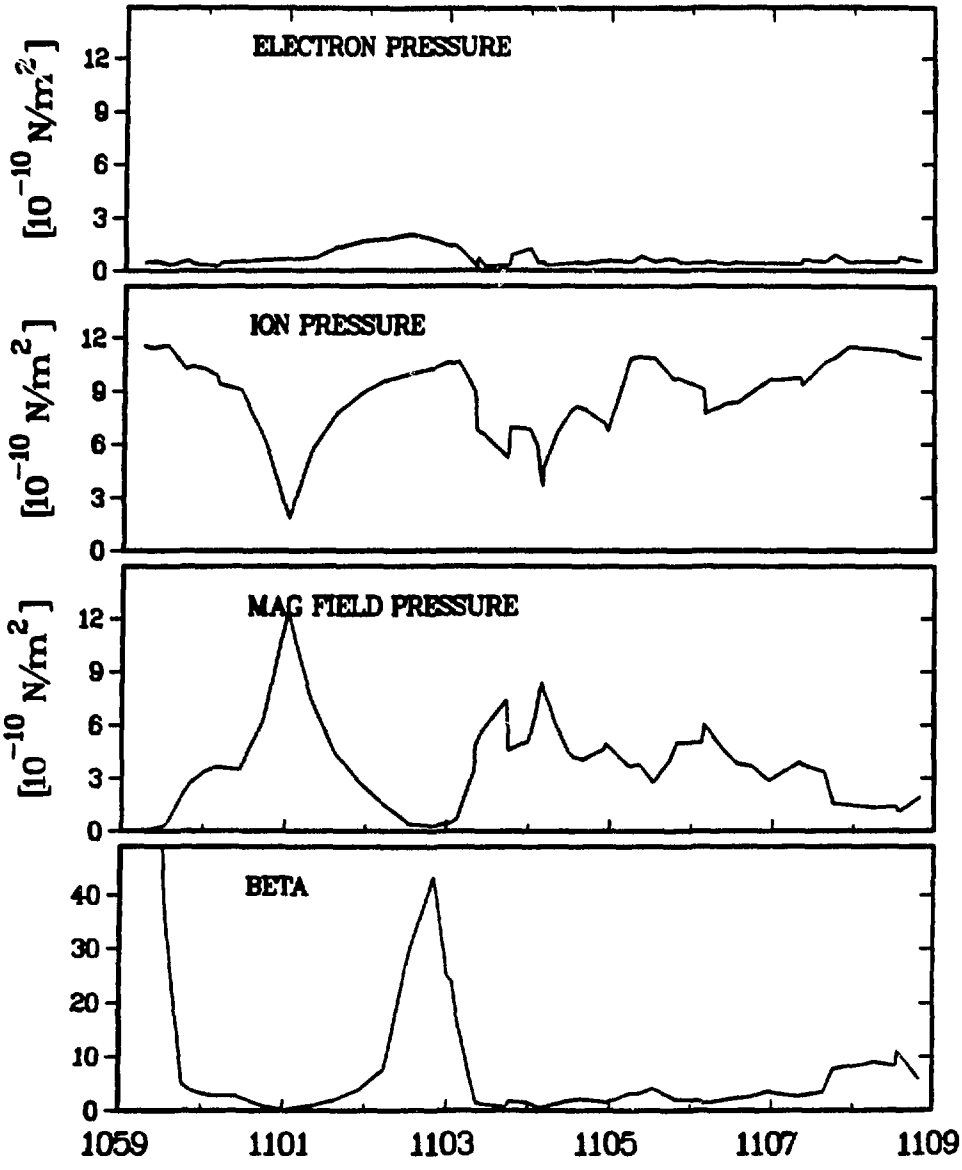

Fig. 4.5. Pressure variations across the magnetotail. The first and third panels show the plasma electron and magnetic field pressures while the second panel displays the plasma ion pressure profile inferred from equation 4.10. The total plasma beta is shown in the bottom panel. Note that the lobes (low beta regions) and current sheet (central high beta region) are easily discernible, as are inbound and outbound tail crossings at ~10:59:40 and ~11:07:40.

Figure 4.5 displays this calculated ion pressure on the same scale as the electron plasma and magnetic field pressures. Note that the ion pressure is appreciably larger than the electron pressure throughout the entire tail traversal, and accounts for the majority of the plasma pressure in the balance condition.

The bottom panel of Figure 4.5 shows the calculated beta of the plasma. In this panel the tail lobe entry at ~10:59:40 and exit at ~11:07:40 are easily discernible, as is the crossing of the center of the current sheet at ~11:02:50. The plasma beta varies rather smoothly through the current sheet traversal maximizing at the center, while sheet entry and exit times can be somewhat arbitrarily defined at ~11:01:20 and ~11:03:20, respectively. The beta in the G-Z tail lobes is generally in the range from 1-4 throughout the entire magnetotail traversal at 7800 km downtail, and rises to ~40 in the center of the current sheet. This situation is quite different from the deep Venus magnetotail where the lobe and current sheet betas are $\sim 10^{-1}$ and $\sim 10^{1}$ respectively [McComas et al., 1986a]; however, it seems likely that farther downstream in the G-Z magnetotail the beta may be reduced due to reacceleration of the plasma and the consequent decrease in the plasma density.

The derived ion pressure profile in the second panel of Figure 4.5 is converted into an equivalent temperature profile assuming the equation of state $P = nkT$ as above, and is plotted in the top panel of Figure 4.6. The ion temperature is quite constant in the current sheet, with a value of $\sim 1.2 \times 10^{5}$K. Just outside the boundaries of the tail it is also relatively constant with a value of 1-1.5 ×

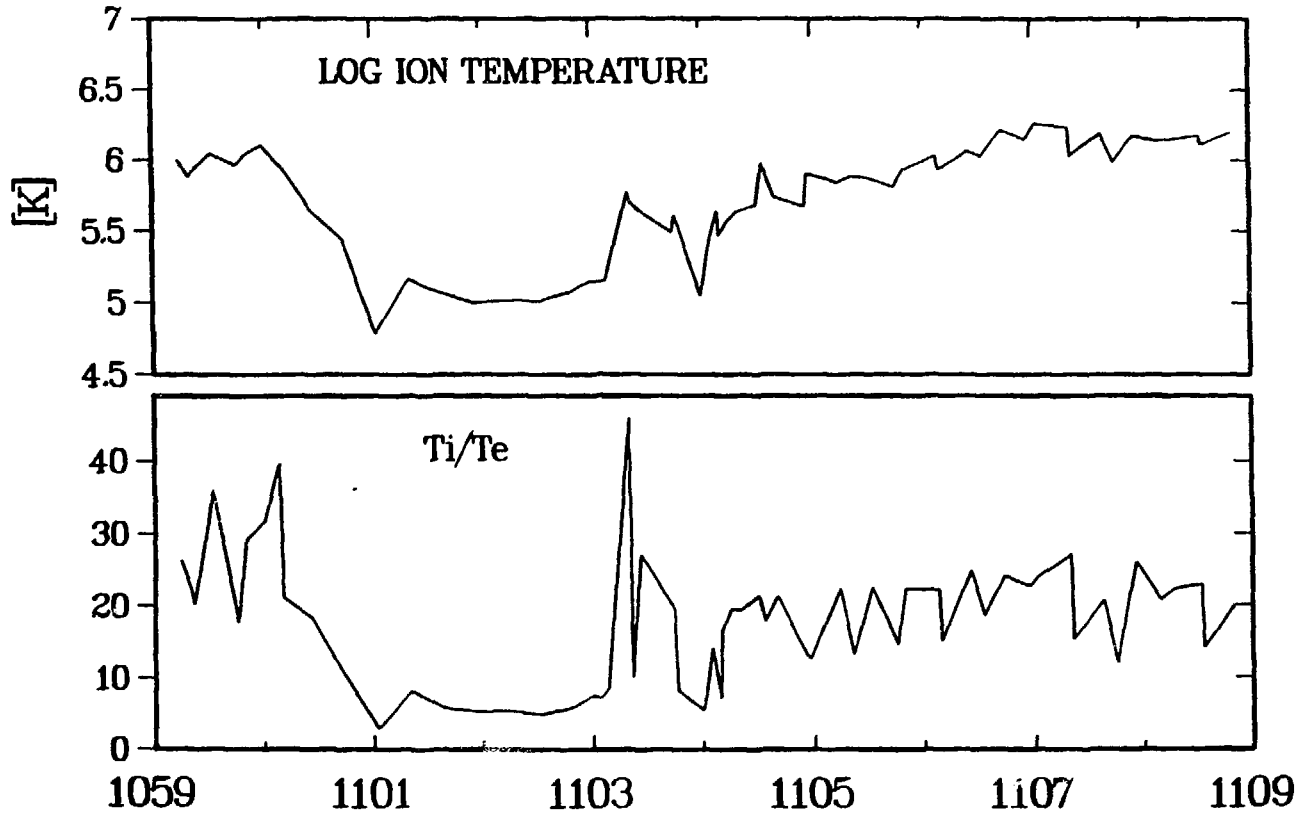

Fig. 4.6. Ion temperature derived from the ion pressure profile displayed in the previous figure. The bottom panel shows the ratio of this dervied temperature to the measured electron temperature. This ratio is relatively constant in the lobes and current sheet with values of approximately 20 and 6.5, respectively.

10^6K. Across the lobes, the ion temperature varies relatively smoothly between these two values. The bottom panel of Figure 4.6 shows the ratio of T_i/T_e across the tail. This ratio is also relatively constant within the current sheet with a value of ~6.5, indicating that neglecting the electron pressure term in the current sheet would have caused about a 15% error in the calculation of the current sheet ion properties. The temperature ratio is also relatively constant, with a value of ~20, throughout most of the rest of the ten minute tail traversal. Such a constant ratio is rather surprising since the electron temperature is presumably determined by cooling rates from the typical photoionization energy of H_2O [Zwickl et al., 1986], while the ion temperature is a function of the flow speed in the average ion pick-up region, as we now describe.

The pick-up ion temperature is not just interesting in its own right, but also contains significant information about the plasma properties at the average location where the cometary ions are picked-up. As pointed out by McComas et al. [1986b] and Siscoe et al. [1986], the average ion temperature in an induced magnetotail is indicative of the velocity of the bulk plasma flow at the average pick-up location. When a molecule is ionized, either by photoionization or charge exchange, the newly formed ion is picked-up by the motional electric field of the flowing, magnetized plasma. The relative motion of the new ion and the flow is essentially the plasma flow speed itself and, therefore, the ion is picked-up with an initial energy equal to the translational energy of the ion in

the plasma rest frame. Eventually, one degree of freedom of translational energy, which has been picked-up into some combination of parallel and perpendicular energies, is isotropized into three degrees of freedom of isotropic thermal energy

$$\frac{1}{2} m_i v_{pu}^2 = \frac{3}{2} kT_{pu} \tag{4.12}$$

where m_i is the mass of a pick-up ion (18 amu) and v_{pu} is the plasma flow velocity at the pick-up location.

In the previous study of MHD equilibrium within the G-Z magnetotail [Siscoe et al., 1986] the ion temperature was assumed to be independent of the downtail, X, distance. Using this assumption, an inferred ion temperature profile (such as is displayed in the top panel of Figure 4.6) can be directly converted into an inferred upstream pick-up velocity profile. In this study we improve the derivation of the relationship between the upstream conditions along each streamline, at the average location upstream from ICE where an ion is picked-up, and at the ICE traversal, by retaining independent variations of the ion plasma temperature and density with X.

Since v_{pu} is a measure of the plasma velocity at the average location where an ion is picked-up, half of the mass picked-up along each streamline is picked-up sunward of the average location and half tailward of this location. Thus, for constant cross-section stream tubes ($\vec{v} = v_X \hat{X}$), the number flux of picked-up ions, nv, at

the average pick-up location is only one half of that measured at ICE,

$$n_{pu}v_{pu} = \frac{1}{2}\, n_{ICE}v_{ICE} \tag{4.13}$$

where all four quantities are defined along a streamline, and n_{ICE} and v_{ICE} are additionally defined along the ICE traversal. The average pick-up properties defined in this way are representative of averages over locations sunward from ICE, but are probably very close to the actual average locations along each streamline since the vast majority of the tail mass loading must occur sunward of ICE. The addition of mass tailward from these average pick-up locations acts to slow the plasma flow further and increase the plasma density beyond the values at the average pick-up location.

The X-components of the momentum equation (4.8a) and the energy equation (4.9) can be integrated along each streamline between the average pick-up locations upstream, X_{pu}, and the ICE traversal crossing distance, X_{ICE}, to yield

$$n_{ICE}\,[m_i v_{ICE}^2 + kT_{ICE}] - n_{pu}\,[m_i v_{pu}^2 + kT_{pu}] = \int_{X_{pu}}^{X_{ICE}} -B_{Y'} J_{Z'}\, dX \tag{4.14}$$

and

$$n_{ICE}v_{ICE}\,[m_i v_{ICE}^2 + 5kT_{ICE}] - n_{pu}v_{pu}\,[m_i v_{pu}^2 + 5kT_{pu}] =$$

$$2 \int_{X_{pu}}^{X_{ICE}} -v_X B_{Y'} J_{Z'} \, dX \qquad (4.15)$$

where the electron component of the pressure has been neglected since it is much smaller than the ion component as demonstrated in Figure 4.5. Combining these equations with the relation between the pick-up velocity and temperature (equation 4.12), and the relation between the average pick-up location and ICE traversal number fluxes (equation 4.13) provides a set of four independent equations which relate the plasma and field properties upstream at the average pick-up location, and at the ICE traversal. The plasma density, n_{ICE}, is measured at each location along the ICE trajectory, $X=X_{ICE}$, while the ion temperature T_{ICE} has been inferred at each location. The remaining unknowns in this set of equations are: v_{ICE}, v_{pu}, T_{pu}, n_{pu}, X_{pu}, and the electromagnetic $(\tilde{J}\tilde{X}\tilde{B})_X$ force and plasma velocity, v_X, as functions of X.

In order to close this set of equations and derive the condition for the X-directed force balance, the electromagnetic term, $B_{Y'} J_{Z'}$, as a function of X must first be determined. The cross tail current density, $J_{Z'}$, is defined in equation 4.6 while the field variations across the tail along the ICE trajectory are displayed in Figure 4.4. The spatial derivative of $\partial B_X/\partial Y'$ is extremely sensitive to the fine scale B_X variations shown in the third panel of this figure. Such variations are not indicative of the global, average configuration of field draping within the tail, but rather probably represent smaller scale structures embedded within the tail, as discussed in the first section, and time

dependent phenomena, such as waves and instabilities. In order to determine the more global, average configuration it is first necessary to smooth the high resolution B_X data. We have examined the results of a number of smoothing intervals, and found that a 60 second running average best removes the high frequency fluctuations without suppressing large scale variations across the tail. From this smoothed field data the cross tail current density, $J_{Z'}$, has been calculated.

Figure 4.7 displays the X-component of the electromagnetic $\tilde{J}x\tilde{B}$ force, $B_{Y'}J_{Z'}$. Throughout the current sheet this force is negative (directed tailward), and acts to accelerate the picked-up plasma and restraighten the kinked field configuration. In the lobes, the X-component of $\tilde{J}x\tilde{B}$ is generally positive due to the fact that the field is still being stretched and draped into a tail configuration through this region. Clearly there is also still a substantial amount of fine structure in Figure 4.7, and plasma properties derived from it will contain substantial fluctuations superimposed on the average variations across the tail. In particular, the negative $(\tilde{J}x\tilde{B})_X$ region at ~11:06 may be indicative of a re-encounter with the current sheet, or may be due to an embedded structure or dynamic effects. This variation is left in since it is large scale; however, the meaningfulness of derived results from this short interval for the general tail structure is questionable.

The variation shown in Figure 4.7 describes the $\tilde{J}x\tilde{B}$ force as measured along the ICE traversal which is the only location where it is known. In equations 4.14 and 4.15, however, the right-hand sides

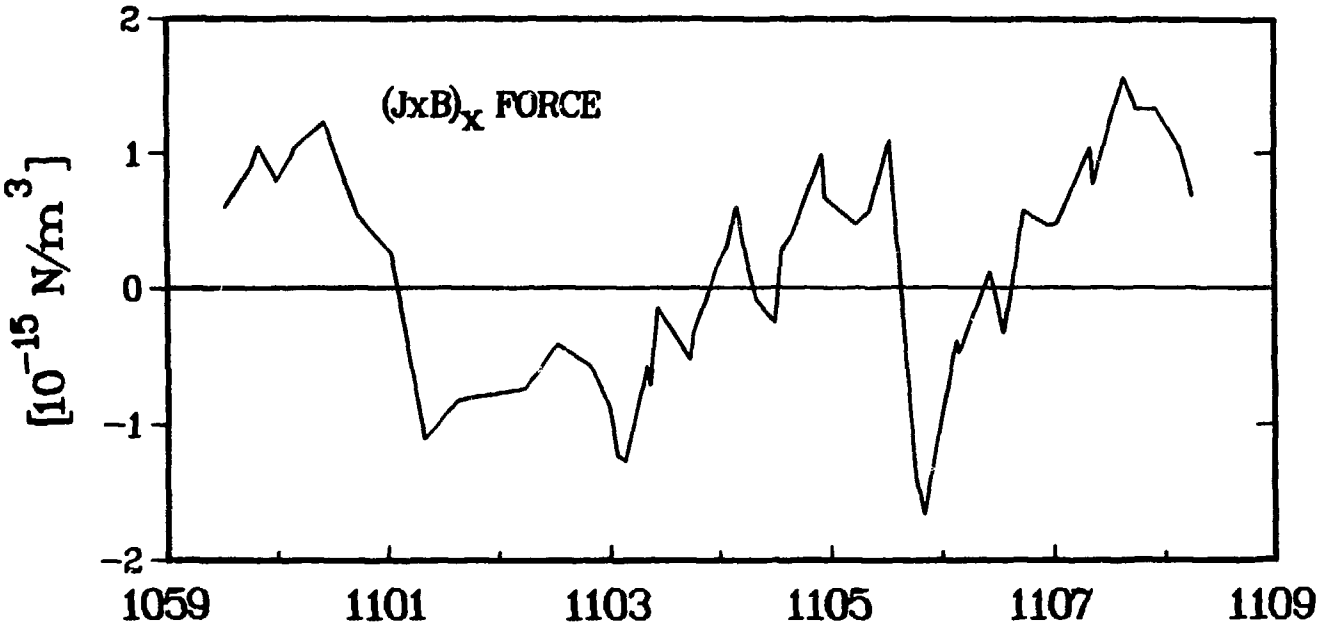

Fig. 4.7. X-component of the electromagnetic J×B force across the tail. The force is negative (tailward) throughout the current sheet, serving to reaccelerate the most highly mass loaded portion of the flow. In the lobes the force is generally positive (sunward) indicating that the field in these regions is still being stretched into a tail-like configuration.

are integrals over X between X_{pu} and X_{ICE}. In order to make these equations tractable with the limited ICE data set we make two simplifying approximations. First, we assume that $B_{Y'}J_{Z'}$ can be approximated with a single value over the limited range from X_{pu} to X_{ICE}. Upstream in the center of the current sheet the $\tilde{J}x\tilde{B}$ force is probably similar to its value at ICE since the effects of field line tension and mass addition are competing in the current sheet, and since the field configuration is draped all the way up to the nucleus; so the field configuration and forces should be only slowly varying functions of distance. In the lobes, on the other hand, both the mass addition and the $\tilde{J}x\tilde{B}$ force act to slow the plasma substantially and increase its density over that upstream while the field continues to stretch about the obstacle and fold into the tail. The $\tilde{J}x\tilde{B}$ force should, therefore, decrease with distance upstream, and be approximately zero sunward of the flaring tail boundary. In order to model this complicated variation as a function of location across the tail as a function of a simple varying value of $B_{Y'}J_{Z'}$, we assume that this value follows the variation measured by ICE, as shown in Figure 4.7, scaled by a factor which varies from one in the center of the current sheet to zero at the edges of the tail. This is by far the most suspect assumption in this derivation, however, its appropriateness will be further supported by independent measurements of the derived plasma velocity at ICE.

The other assumption needed to close the set of equations deals with the integral of the plasma velocity with downtail distance. We

assume that the integral of v_X over X is approximately its average value times the X distance: $\frac{1}{2}(v_{pu} + v_{ICE})(X_{ICE} - X_{pu})$. In the upstream region of the current sheet the average pick-up location is probably very close to the nucleus since the neutral density is largest there and drops off rapidly with distance. Upstream from the lobes the situation is somewhat less clear, but the average pick-up location is still probably near the location of maximum neutral density, X = 0. Therefore, we use $(X_{ICE} - X_{pu}) = -7800$ km across the tail.

Including these approximations, equations 4.14 and 4.15 can be combined with equations 4.12 and 4.13 to solve for the four unknowns: v_{ICE}, v_{pu}, T_{pu}, and n_{pu} at each data point along the ICE trajectory. This set of equations is somewhat complicated, being quadratic in both v_{pu} and v_{ICE}. Therefore, instead of solving them analytically, we choose to solve the set of equations with an iterative computer technique.

The results of this calculation are displayed in Figure 4.8. The top panel shows the derived plasma velocity variation across the tail along the ICE trajectory. Through the current sheet the tailward velocity is somewhat variable with an average value ~-20 km/sec. In the lobes the velocity is more variable, having an average value somewhere from -20 to -30 km/sec, which increases slightly toward the sides of the tail. The large fluctuations across the plot are probably not indicative of the average, global structure, but rather embedded fine structures and time dependent effects. Still, the general result that the velocity profile at the

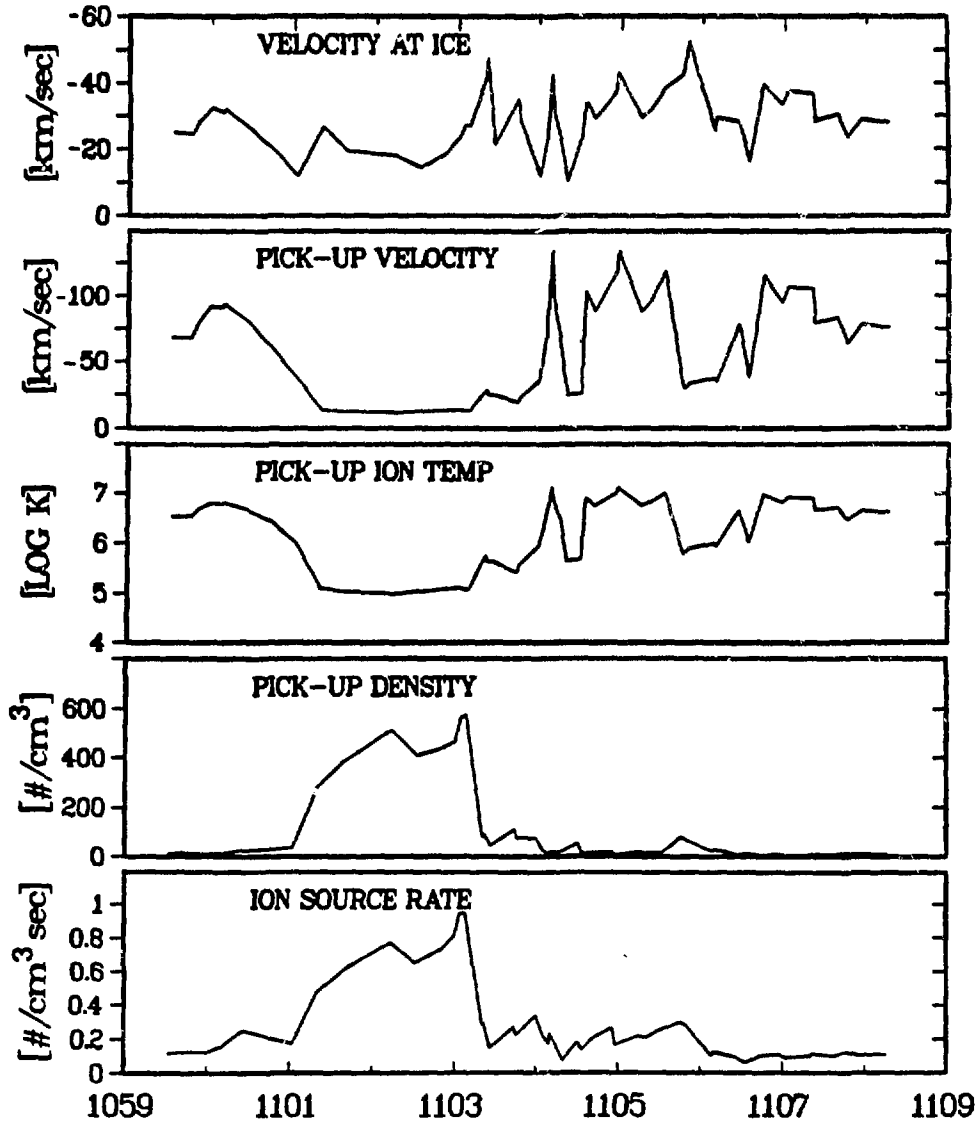

Fig. 4.8. Results of the observation based MHD calculation of the flow velocity at ICE and plasma properties upstream at the average pick-up location. The top two panels display the velocity profiles at ICE and the average pick-up location, and indicate that the velocity shear responsible for creating the draped tail configuration occurs upstream from the ICE tail traversal. The third and fourth panels show the average pick-up temperature and density, while the fifth panel displays the calculated ion source rate averaged over 7800 km from the average upstream pick-up location back to ICE. Sharp gradients between the current sheet and tail lobes in these various parameters indicate that the current sheet is downstream from a "prime mass loading region" which has a substantially enhanced source rate.

ICE traversal distance is nearly flat is well resolved by our calculation.

The result that the plasma velocity along the ICE tail traversal is nearly constant can be independently verified with the ICE magnetic field measurements. In a steady state solution of Faraday's Induction Law, $\nabla \times \tilde{E} = 0$. In the MHD hydromagnetic limit with $B_{Z'} = 0$, this corresponds to the statement that $v_X B_{Y'} =$ constant. The fourth panel of Figure 4.4 shows that $B_{Y'}$, is on average quite constant across the ten minute interval. The plasma velocity must also, therefore, be reasonably constant as derived here.

As a further check, the observational lower limit for bulk velocity determinations at G-Z with the Los Alamos electron analyzer is ~30 km/s. Plasma electron data for the crossing indicate that a velocity in excess of this value was not consistently achieved for ~9 and ~6 minutes beyond the inbound and outbound edges of the magnetotail, respectively. The calculated plasma velocity displayed in the top panel of Figure 4.8 is, therefore, generally in excellent agreement with the lack of direct velocity observations through the tail region. The variation of velocity across the tail is sensitive to the assumptions made above in general, and the treatment of the electromagnetic force term in particular. The good agreement between the derived velocity and the ICE field and plasma observations supports the general validity of those assumptions.

The plasma parameters derived for the average upstream pick-up location, $X \approx 0$, are displayed in panels 2-4 of Figure 4.8. Panels

2 and 3 show the calculated average ion pick-up velocity and equivalent ion temperature, which are related by equation 4.12. The velocity and temperature are extremely constant through the current sheet with values of ~-12 km/sec and ~$1x10^5$ K, respectively. These values become highly variable and rise outside the current sheet, in the lobes, to average values of ~-75 km/sec and ~$4x10^6$K near the edges of the tail. The difference between the velocities upstream from the lobes and current sheet is fundamentally responsible for forming the magnetotail configuration observed at ICE since the large velocity shear drapes the solar wind's embedded magnetic field. In the Discussion section we will examine the implications of the derived velocity shear upstream and the nearly constant velocity across the tail at ICE, and discuss some of the more detailed aspects of the tail formation process.

The derived ion density at the average upstream pick-up locations is plotted in panel 4. The region upstream from the current sheet has a density of ~200 - 600 ions/cm^3 while the regions upstream from the lobes have decreasing densities away from the current sheet, and an average value across the lobes of only ~20 /cm^3. Comparing this panel with the measured density along the ICE trajectory (top panel of Figure 4.4) indicates that the gradient in number density across the tail is much larger near the comet nucleus than it is back in the tail, and that the region of enhanced density also has sharper boundaries upstream near the nucleus.

From the derived density and velocity profiles at ICE and upstream, the average ion source rate, S^*/m_i, between these two

locations, can be readily found. The time independent continuity equation (4.7) evaluated between ICE and the average pick-up location is

$$\frac{n_{ICE}\, v_{ICE} - n_{pu}\, v_{pu}}{X_{ICE} - X_{pu}} = S^*/m_i \qquad (4.16)$$

and the results of this calculation are displayed in the bottom panel of Figure 4.8. It must be remembered that this is an average over 7800 km and, therefore, the source rate is probably much greater within the range close to the nucleus, $0 \gtrsim X \gtrsim -1000$ km. Still, the ion source rate is clearly much greater in the region upstream from the current sheet than from the lobes. The "prime mass loading" region discovered in this study is only ~1500 km across in Y', and implications of this small region of high density, slowly flowing plasma where a substantial portion of the mass loading occurs, are examined in more detail in the Discussion section.

4.4 Cometary Mass Transport

The mere existence of comet tails, and earthbound observations which often show tailward propagating features, indicate that substantial numbers of cometary ions are transported down the high density ion tail or magnetotail current sheet. At Venus, the majority of the lost planetary ions are apparently transported down the magnetotail (see calculations by McComas et al. [1986a], and

reference therein). At comets, the mass loading region is much more extended than at Venus since the cometary neutral atmosphere is not gravitationally bound, and a far smaller fraction of the picked-up ions may be involved in draping the magnetic field into a magnetotail.

Calculations by Mendis et al. [1986], which combine the model of Schmidt and Wegmann [1982] and typical plasma and field values observed during the ICE encounter, yield a cometary loss rate of 4.0×10^{28} molecules/s. Direct measurements of the bow wave crossing locations by Jones et al. [1986] and indirect measurements by Fuselier et al. [1986] yield loss rates of 2.3-2.5 and 3×10^{28}, respectively. Within the errors of the various techniques, these three values are all consistent.

In this study we make a more detailed examination of where these cometary ions are picked-up by the solar wind flow by examining the ion transport rate (number flux) from the direct ICE observations. The ion number flux, nv, is a direct measure of the number of ions passing downtail per unit area and time. Of course neutrals are not measured in the number flux, but all neutrals which are ionized sunward of the ICE traversal plane are carried tailward through the plane as ions, and are counted in the number flux. These include all neutrals with an initial sunward velocity and those with an initial tailward velocity that are ionized sunward from the ICE traversal. Therefore, more than half of the neutral cometary efflux will pass through this plane as ions added to the flow.

The rate at which ions are lost down the Giacobini-Zinner magnetotail can be calculated by integrating the particle number flux over the tail cross-section. The cross-sectional tail geometry at the downtail distance of the ICE traversal is shown in Figure 4.3. For this calculation we use the measured density distribution shown in the top panel of Figure 4.4 and a constant downtail velocity of -20 km/s, as discussed in the previous section. Combining these data, and integrating in 10^4 km long strips parallel to the Z'-axis we find that the total number of particles flowing down the magnetotail is $\sim 2.6 \times 10^{26}$ molecules/s.

A number flux of $\sim 2.6 \times 10^{26}$/s lost down the magnetotail represents only ~1% of the total cometary loss rate quoted above. Such a result is not unreasonable in light of the extremely extended nature of the neutral atmosphere and, therefore, mass addition region. It does, however, bring to light the question of where the major mass pick-up and transport occurs.

To address this question we calculate the particle loss through a cylinder which encompasses the extended mass loading region, as drawn in Figure 4.9 The axis of the cylinder is parallel to the X-axis and the unperturbed solar wind approaches the comet along the -X-direction. The cylinder has a radius of $\sim 2.4 \times 10^5$ km which extends out to the region along the flanks of the comet where no significant slowing associated with ion pick-up could be detected. The upper surface of the cylinder lies well upstream of the comet. We assume that the external solar wind flow was constant during the inbound (outbound) portion of the ICE traversal with a number flux

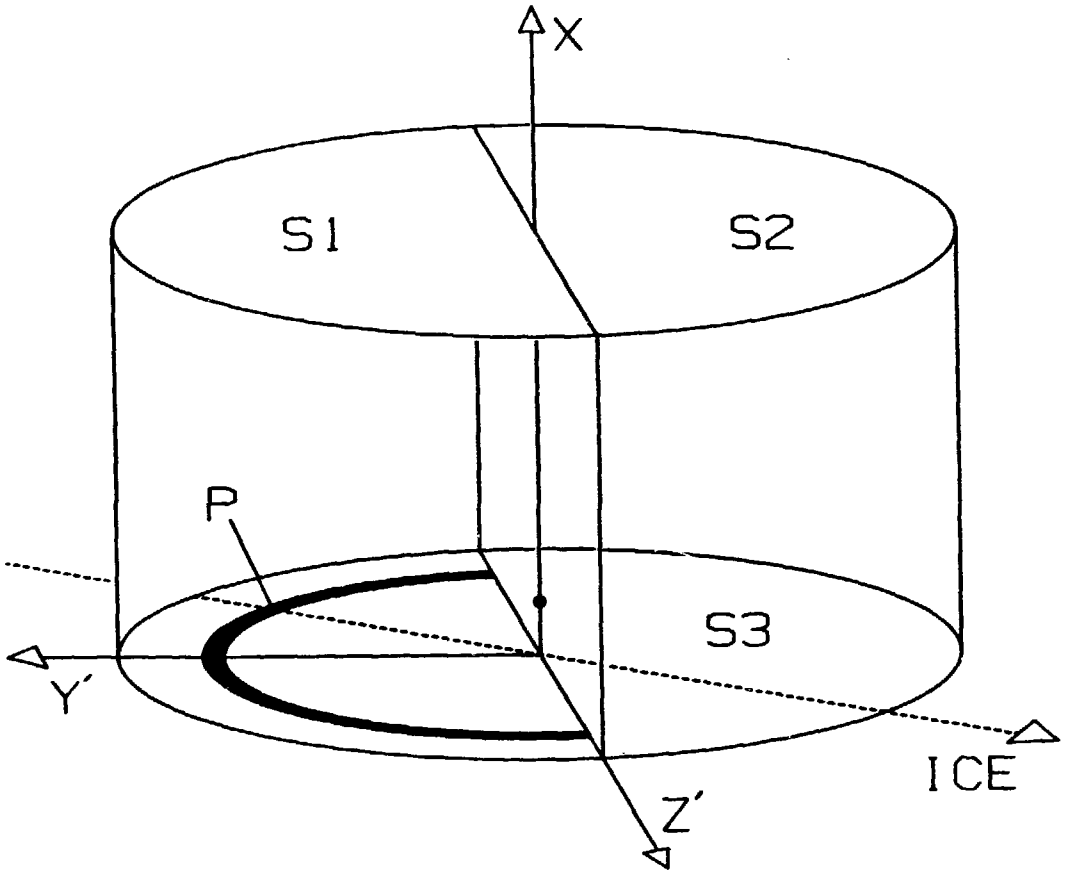

Fig. 4.9. Schematic diagram of the geometry used for calculating the cometary neutral gas efflux. The axis of the cylinder is aligned with the solar wind flow, and is wide enough to encompass the entire cometary mass loading region back to the plane of the ICE traversal. The difference in the number of particles crossing the top surface, S1+S2, and the bottom surface, S3, must have been added to the flow within the cylinder. The number of particles crossing S3 is calculated by assuming uniformity within half circular annuli along the ICE trajectory.

n_1v_1 (n_2v_2) passing through the surface S1 (S2), and equal to that measured just outside the cylinder along the ICE trajectory. The ICE spacecraft traverses the comet in the plane of the bottom surface, S3, of the cylinder. We assume that the plasma conditions are approximately cylindrically symmetric, as indicated by MHD models of G-Z at this downtail distance [Fedder et al., 1986], and in particular, that the observed properties constitute average values for half circular annuli at each point, P, along the trajectory. By integrating the plasma properties over these annuli, the total number of particles crossing surface S3 is determined. If the comet is ejecting molecules at an approximately steady rate, Q, then the number of cometary particles picked-up by the flow, sunward of the ICE traversal, is

$$Q = \sum_a n(t)\, v(t) A_a - (n_1 v_1 S1 + n_2 v_2 S2) \qquad (4.17)$$

where n(t) and v(t) are the observed density and tailward velocity of the plasma, and A_a is the annulus area at each point P along the trajectory.

The smoothed electron density profile for the entire G-Z crossing is shown on a logarithmic scale in the top panel of Figure 4.10. Ground based observations of comets integrate such density profiles along a line of sight, and it is not surprising that only the magnetotail and visible coma stand out in such observations. The fact that the density is large, however, does not

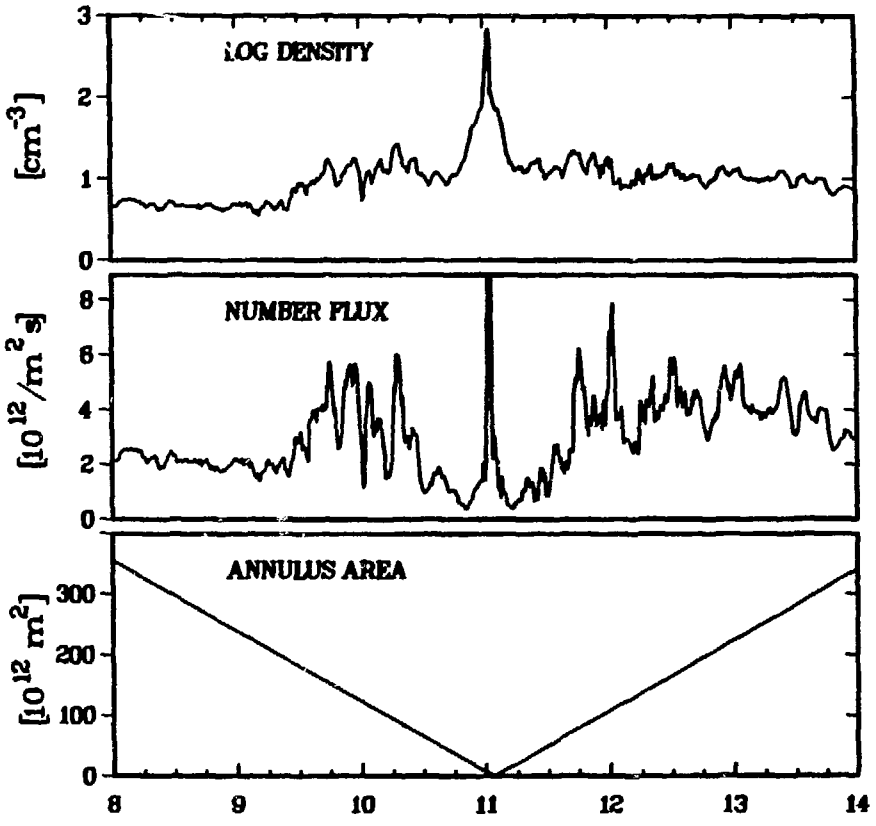

Fig. 4.10. Parameters used in the calculation of the cometary efflux. The plasma density is clearly maximized in the magnetotail (narrow feature at ~11:00) and surrounding coma, which accounts for the high visibility of these regions. The middle panel displays the number flux, n, which also maximizes in the magnetotail current sheet, rising off the top of the plot to a value of $14 \times 10^{12}/m^2s$. Data in both of the top two panels have been smoothed with a nine point running average except in the narrow tail region. The majority of the cometary particles are apparently lost in regions far from the comet nucleus, largely due to the increase in effective transport area with distance as depicted in the bottom panel.

imply that the particle flux in these regions is large since the flow is also slow there.

The calculated number flux of particles is shown in the middle panel of Figure 4.10. The flux is clearly highly variable but generally maximizes in the transition region and outer magnetosheath, far from the magnetotail itself. In fact, other than within the narrow tail current sheet, the flux was smaller in the magnetotail than in the surrounding solar wind. The portions of the profile from 8:00 to ~8:45 and ~13:00 to 14:00 are essentially unperturbed solar wind, as evidenced by the velocity profiles displayed in Figure 4.2, and are used to fix the upstream values for the inbound and outbound portions of the crossing. These values are ~2 and ~4 x $10^{12}/m^2s$, respectively, and are used to determine the flow through surfaces S1 and S2 in Figure 4.9 and equation 4.17.

Velocity variations provide a much more sensitive indicator of ion pick-up than number density variations because cometary pick-up ions are much heavier than the average solar wind ions (protons). The number density reflects only increases in the total number of added ions, and for example, a 1% addition of pick-up ions of average mass 20 increases the number density by about the relative instrumental resolution of the Los Alamos plasma analyzer, 1%. However, the mass density is increased by ~20%, and the flow speed should be reduced to about 80% of its unperturbed value, providing an easily resolvable signature.

The bottom panel of Figure 4.10 displays the annulus area per 24 second plasma data sample. This value was simply calculated from

the location of the spacecraft as a function of time and the constant crossing velocity in the Y'-Z' plane. Since it is the product of the bottom two panels which gives the rate of particle loss, the outer portions of the crossing are clearly the dominant regions for particle transport.

Using the values of 2 and 4 x $10^{12}/m^2s$ for the upstream solar wind, as given above, we find a solar wind particle flux of 2.11 x $10^{29}/s$ entering the top of the cylinder. Integrating the loss rate of particles through surface S3, we find a flux of 2.36 x $10^{29}/s$ exiting the bottom surface of the cylinder. Finally, using equation 17 to take the difference of these two large numbers, we find that the number of cometary ions picked-up by the solar wind flow, sunward of the ICE traversal, is 2.5 ± 1.5 x $10^{28}/s$. The upper and lower bounds are arrived at by assuming number fluxes of 1.8 and 3.8 x $10^{12}/m^2s$ and 2.2 and 4.2 x $10^{12}/m^2s$ for the inbound and outbound legs.

Some cometary material is undoubtedly picked-up tailward of the ICE fly through distance as discussed above. This effect should account for an increase in the actual loss rate of the comet as compared to the numbers calculated here. The numbers derived with this method, therefore, represent lower bounds on the total cometary loss rate. The amount of material picked-up tailward of the ICE traversal should be less than or equal to that picked-up sunward and, therefore, we find a total cometary particle loss rate of ~2.5-5 x 10^{28} molecules/s, in excellent agreement with the various independently derived values quoted above.

4.5 Summary and Discussion

In this study we have used the combined plasma and magnetic field data sets from the ICE traversal of Comet Giacobini-Zinner to make a detailed examination of the configuration and properties of the draped G-Z magnetotail in general, and its field reversing current sheet in particular. The general interaction of the solar wind and embedded IMF with cometary bodies is well understood in terms of mass loading and, consequently, slowing of the flow, and draping of the magnetic field due to the velocity shear between regions at varying transverse distances from the obstacle. The details of the global interaction and magnetotail formation process, however, are at present not well understood and are of considerable interest to the space physics community.

At the time of the ICE crossing the G-Z magnetotail was rotated $\sim 10.5^{o}$ in the normal aberration sense, and $\sim 9.9^{o}$ above the ecliptic plane. The large difference in inbound and outbound tail lobe sizes can then be explained as a purely geometric effect due to the fact that ICE traversed the tail slightly off-center. The angle of the cross tail current sheet from the ecliptic plane ($\sim 43^{o}$) derived purely from magnetic field measurements is in excellent agreement with that derived with spacecraft timing under a circular tail cross-section assumption ($\sim 47^{o}$), and this agreement suggests that the tail may be quite circular. A circular geometry is not expected from the near-nucleus ion pick-up process, and suggests that some circularization of the tail has occurred downstream from there. The

residual ram pressure within the cometary environs could supply just such a circularizing effect.

The cross tail (Y') component of the MHD momentum equation was used in the MHD Equilibrium section to derive the unmeasured ion properties required to supply pressure balance across the tail. The calculated ion pressure is much greater than the electron contribution across the entire tail. The plasma beta varies across the tail from ~1-4 in the lobes to ~40 in the central current sheet. The beta calculations can be used to denote the location of the inbound and outbound edges of the tail where beta rises sharply.

Combining the electron plasma and magnetic field measurements with the X-components of the MHD equations made it possible to infer the plasma properties of the near-nucleus region where the average ion is picked-up. These inferred properties, displayed in Figure 4.8, indicate that the strongest mass loading is confined to a region only ~1500 km across. In this narrow region the plasma flow velocity drops to ~-12 km/sec, a factor of 6-7 slower than the flow about 1000 km farther on either side of the obstacle. At the same time, the plasma density is ~200-600/cm^3 in this region, a factor of 10-30 times that of the adjacent region. Similarly, the inferred ion source function, displayed in the bottom panel of Figure 4.8, shows sharp rises at the edges of this region even though the function has been integrated over 7800 km from the average pick-up location back to ICE. If the primary mass loading region has an X extent of 1500 km, similar to its Y' extent, then the approximate ratio of ion source rates is (7800/1500) times the ratio of values

displayed in this panel (0.7/0.15). This calculation yields a ratio of ion source rates inside/outside of the prime mass loading region of ~24.

Such a sharp gradient in the ion source rate and related plasma parameters is perhaps somewhat unexpected. MHD cometary simulations such as those by Schmidt and Wegmann [1980, 1982] and Fedder et al. [1986] assume that the source term is a spherically symmetric function of distance, R, from the comet's nucleus and is proportional to $R^{-2}\exp(-R/R_o)$. Therefore, such simulations should do a much poorer job of modeling cometary magnetotails than the more global cometary interaction. Other models (e.g., Huebner [1985] and Boice et al. [1986]) allow for detailed chemistry interactions in the cometary coma, and often show very strong gradients in total ion density (see for example Figure 3 in Huebner [1985]), but do not model the full MHD interaction with the inflowing solar wind. In the classical cometary picture, and most of both types of models an impenetrable boundary or contact surface serves to separate the solar wind from the majority of the ionized cometary material. Mendis et al. [1986] calculate a boundary or ionopause radius of ~600 km for Comet Giacobini-Zinner at the time of the ICE crossing, which is very similar to our inferred radius of ~750 km for the prime mass loading region.

In the classic picture of cometary magnetotail formation the magnetotail plasma sheet is simply a tailward extension of the near-nucleus ionospheric region, and is comprised of cold ($T_i \lesssim 1000^o$ K) and totally unmagnetized ions. This is expected to

occur because the near-nucleus ionization rate is substantially larger than the recombination or loss rate and, therefore, tailward ion flow is required to maintain a steady state configuration. In this study we find no evidence for such an extended region of purely cold, ionospheric plasma back at the ICE traversal distance of -7800 km. The magnetotail plasma sheet or current sheet data from G-Z indicate that the region is magnetized throughout, and is comprised of ions about 100 times hotter ($\sim 10^5$ K) than typical expected ionospheric temperatures. For the tail to maintain its form ~8000 km downstream from the comet nucleus at least a rough pressure balance must exist and, therefore, relatively hot ion temperatures within the current sheet are unavoidable since the electron pressure is so small.

While no evidence exists for an extended region of purely cold ionospheric plasma at the ICE downstream traversal distance a well formed ionospheric obstacle upstream, near the nucleus, may be present. Initial results from the Comet Halley encounters at varying distances upstream from the nucleus (see the special Nature issue [Vol. 321]) demonstrate the existence of the cold ionospheric region which is, at most, only slightly magnetized ($|B| \lesssim 2$ nT). Furthermore, the similarity of the calculated ionopause radius and the inferred radius of the prime mass loading region suggests that the two may be closely related.

One possible explanation for both the observed current sheet properties and the comparatively large source rate inferred in the prime mass loading region upstream is based on the penetration of

the solar wind through the cometary ionopause and into the cometary ionosphere. While most models assume the cometary ionopause to be perfectly impenetrable, this seems rather unlikely. Stagnation streamlines may have sufficiently slow flow that the magnetic field has time to diffuse inward as is observed at Venus, although the convective flow is outward from the nucleus rather than inward toward the planet. Alternately, other processes such as the Kelvin-Helmholtz instability may act at the cometary ionopause allowing penetration of the field and flow as suggested by Ershkovich and Mendis [1983]. The solar wind flow and field which partially penetrates the ionopause would have access to the much larger ionospheric ion densities, and consequently larger source rates. The ICE observation that the magnetic field has a substantial component across the tail and the large ion temperature inferred from a pressure balance condition indicate that at least 7800 km back in the tail, no extension of an ionopause boundary which delineates a region of cometary ions that have never been picked-up by the solar wind was encountered. Rather, unless this region is very narrow, and was simply missed by ICE, the observations indicate that current sheet ions, which pass the ICE traversal distance, may all have been picked-up within the higher density region at the cometary ionosphere.

Another possibility is that the large source rate inferred in the prime mass loading region could be caused by physical variations in the neutral source structure at the nucleus. Observations by the Vega and Giotto spacecraft show clear evidence for gas/dust jets

emanating from the sunlit side of the nucleus, and fissuring of the nucleus surface. Such jets could have the effect of forming very strong gradients in the neutral, and therefore ion, densities. Such an enhanced region could account for the large source rate in the prime mass loading region as demonstrated by our analysis.

Finally, the coma chemistry models could account for the large ion source rate. Complicated cometary chemistry processes extend out to some thousands of km from the cometary nucleus, and provide strong gradients in certain ionic abundances. It could simply be that the prime mass loading region is demarked by particularly strong gradients in the ion density.

For whatever reason the plasma flow is preferentially mass loaded within a small region upstream the implications of this region for the formation, density, and length of the cometary magnetotail, and visible ion tail (magnetotail current sheet) are fundamental. At the distance of the ICE traversal the tailward plasma velocity is relatively constant at ~-20 km/sec across the entire tail. Upstream, at the average pick-up location along each streamline, the flow in the prime mass loading region is much slower than that upstream from the lobes and immediately adjacent portions of the ionized coma. Therefore, the velocity shear, which causes the draped magnetic configuration, and thereby the magnetotail itself, must occur upstream from the ICE encounter where current sheet velocities are appreciably smaller and lobe and ionized coma velocities appreciably larger.

The ICE downtail traversal distance turns out to be a

fortuitous area for the spacecraft to have passed through for magnetotail studies, in that the flow velocity is relatively constant across the tail. The plane that ICE crossed the tail in, therefore, essentially separates the regions of tail formation and dissipation. Beyond this distance the still accelerating plasma in the current sheet should be overtaking the surrounding plasma and the field configuration should be reapproaching a straight (nondraped) configuration.

The inferred approximate flow speeds in the current sheet (near the edges of the lobes) in the prime mass loading region and at ICE are -12 km/sec (-75 km/sec) and -20 km/sec (-25 km/sec), respectively. The average flow velocities between these two locations are, therefore, ~-16 km/sec and ~-50 km/sec. Using these average speeds, the times for an average pick-up ion to reach the ICE crossing plane are ~8.1 and ~2.5 minutes for the current sheet and lobes, respectively. This indicates that the plasma in the current sheet is lagging the plasma in the lobes by ~5.6 minutes.

If the current sheet plasma continues to accelerate at ~-8 km/sec in ~8 minutes, and the ionized coma velocity beyond the major mass loading region stays fixed at ~-25 km/sec, the draped magnetotail configuration would be entirely dissipated (i.e., the field would be completely straightened out) within some tens of thousands of kilometers downstream from the nucleus. Of course, as the field restraightens the $\tilde{J}x\tilde{B}$ force acting to accelerate the plasma is reduced so that a slightly draped configuration should be expected to extend out to somewhat greater distances.

As the current sheet plasma accelerates, its density decreases in order to conserve the number flux. In addition, as the field configuration straightens, the current sheet plasma becomes less confined in the Y'-direction, and plasma pressure gradients and particle parallel velocities tend to spread out the plasma in the current sheet and further decrease its density. As the current sheet density decreases with distance, the tail becomes less visible. The tail scale length given above is in basic agreement with the fact that a visible ion tail was observed in CCD images from earth in the H_2O^+ 619.8 nm line some 9600 km tailward from the nucleus at the time of the ICE encounter [Strauss et al., 1986], as discussed in greater detail by Slavin et al. [1986b] and Meyer-Vernet et al. [1986c]. Our calculated tail scale length is also in agreement with the general lack of observations of a tailward ionic extension from G-Z greater than a few tens of thousands of km.

At more active comets such as Halley, which has a neutral gas production rate ~20-40 times that of G-Z, the solar wind must become even more slowed in the prime mass loading region, and the field configuration must become more highly kinked. Without knowing the details of how an enhanced gas production rate would affect the prime mass loading region versus the immediately surrounding region, it is difficult to ascertain exactly how the comet's tail would be affected. However, it is clear that such a comet should have substantially slower current sheet flows. Since the density is proportional to the gas production rate, and inversely proportional to the flow velocity, ion densities in such ion tails should be

substantially enhanced over G-Z's, and these tails should be much more visible. The length of more active comets' tails should also be appreciably greater since any further slowing near the nucleus would cause the current sheet plasma to fall even further behind the lobe flow throughout the near portions of the magnetotail. For any reasonable $\tilde{J}x\tilde{B}$ reacceleration rate this difference should take appreciably longer to be made up.

Smaller comets such as G-Z may also go through active phases due to surface effects such as cracking and large variations in the gas production rate. Evidence described above for observations of surface fissures and large scale gas/dust jets at comet Halley indicate that the cometary source function can be far from constant or symmetric. In addition, variations in the upstream solar wind parameters undoubtedly have an effect on tail formation, and one might expect that higher speed flows would enhance the tail formation and field draping process by increasing the plasma flow outside of the prime mass loading region. Such variations might account for the difference between this apparition of G-Z and the last, in 1959, which regularly exhibited a long visible ion tail.

While the very small prime mass loading region has an ion source rate $\gtrsim 24$ times that anywhere else in the extended cometary environs, and is apparently responsible for producing the narrow, well-defined comet tail, the total, integrated mass addition in this small area is $\lesssim 1\%$ of the steady state mass added to the flow throughout the extended cometary region. Consequently, the most visible aspect of cometary apparitions, the ion tail, or magnetotail

current sheet, is relatively unimportant in the global cometary process of mass loading the solar wind, and removing the large cometary efflux.

The generally good agreement between global cometary models and the results from the ICE Giacobini-Zinner encounter indicate that the detailed physics of the comet nucleus and near-nucleus region are not of fundamental importance to the large scale cometary interaction and the majority of the cometary mass pick-up. This study, however, indicates that a detailed knowledge of the nucleus and near-nucleus region are of fundamental importance to the understanding of the magnetotail formation process and the large variations in visible ion tails which have intrigued mankind for millenia. We look forward to the many valuable and detailed studies which will undoubtedly spring from the Halley armada data sets upstream from the comet nucleus, and hope that a truly fundamental knowledge of comets and cometary nuclei will be made attainable soon through the realization of the Comet Rendezvous Asteroid Flyby (CRAF) mission.

4.6 Chapter Acknowledgments

We gratefully acknowledge comments and suggestions on this paper from C. T. Russell, J. G. Luhmann, M. F. Thomsen, and R. D. Zwickl and are particularly grateful to G. L. Siscoe for his many valuable suggestions. The research performed at the Jet Propulsion Laboratory of the California Institute of Technology was carried out under contract to NASA, while work done at Los Alamos

was performed under the auspices of the United States Department of Energy with support from NASA under S-04039-D.

Chapter 5

Summary and Discussion

5.0 Summary

Planetary and cometary magnetotails are some of the largest, most interesting, and most often observed manifestations of the solar wind's interaction with solar system bodies. Generally, magnetotails are formed out of the flowing solar wind's interaction with various relatively stationary MHD obstacles.

Although there are a number of general similarities between the manifestations of magnetotails and their field reversing current sheets at the earth, Venus, and Comet Giacobini-Zinner, many important differences also exist. These are based on fundamental differences in the nature of the planetary/cometary bodies and, therefore, the obstacles they present to the solar wind. The numerous new results of this dissertation, highlighted in the three sections below, represent a wealth of new information about the detailed manifestations of the magnetotails and field reversing magnetotail current sheets at these three planetary/cometary bodies. Through the detailed examination of the various magnetotail and current sheet configurations and properties, it is hoped that this dissertation has served to convey some of the richness of variety which magnetotails and their field reversing current sheets display throughout the solar system.

5.0.1 Earth

The section on the terrestrial magnetotail (Chapter 2) examines the detailed geometries and current density distributions in the near earth cross tail current sheet during an interval of relative geomagnetic quiet. In this way a typical, time independent configuration of the tail is studied, and the details of how the currents flow within the current sheet are determined. The major new accomplishments and results of this section are summarized here.

1) Combined magnetic field and three-dimensional plasma data from the co-orbiting satellites ISEE-1 and -2 were used to examine the current sheet geometries at the times of three sheet crossings. From the measured field orientations, the inclinations of the field lines within the current sheet were inferred. This analysis yielded inclinations of 15^{o}, 59^{o}, and 72^{o} and indicates that large field inclinations within the current sheet may be commonplace, even at relatively geomagnetically inactive times. Further, this work stimulated an equilibrium analysis of the magnetotail [Voigt and Hilmer, 1986] which theoretically explains the large observed inclinations.

2) A new data analysis technique was developed in this section to calculate the variable current sheet crossing velocities from the co-orbiting, dual satellite, magnetometer data sets, and the inferred field inclinations. This technique allows the spatial variations in the field to be separated from temporal fluctuation, and thereby resolves them.

3) Integrating the variable velocity profiles over the intervals of the current sheet crossings yields current sheet thicknesses which are determined independent of sheet motions for the first time. For the relatively quiet cases studied here the total sheet thicknesses are in the range from ~1-5 × 10^4 km (tens to hundreds of ion gyroradii), where the thinner sheets are associated with cases of larger field inclinations.

4) While the current sheet is thick on the size scale of an ion gyroradius, this chapter demonstrated that it is appreciably thinner than the plasma sheet as defined by the plasma data. The cross tail current sheet and plasma sheet are, therefore, separate entities, with the current sheet being embedded in the thicker plasma sheet.

5) Separation of the spatial and temporal variations of the magnetic field through the current sheet crossings made it possible to calculate the detailed current density distributions in the cross tail current sheet for the first time. These distributions are displayed in Figures 2.6, 2.9, and 2.10, and the peak current densities range from ~5-50 nA/m^2.

6) Current density distributions calculated in this section appear to be characterized by two distinct regions. The central ~1/3 of the distributions contain relatively large current densities which peak very near to the center of the current sheet. Outside this region the distributions generally display shoulders of lesser current densities which decay with outward distance.

7) Superimposed on the general shapes of the distributions there is considerable fine scale structure which produces large amplitude variations in the current density with scale sizes ~2-6 x 10^3 km (a few to tens of ion gyroradii). These peaks may indicate that the cross tail current sheet consists of numerous fine scale current filaments, possibly caused by ion kinetic effects.

5.0.2 Venus

The Venus section (Chapter 3) concentrates on determining the average configuration and properties of the Venus magnetotail. This goal had not been previously achieved due to the extremely large variability of the tail location and magnetic configuration. In this dissertation the variability is used to provide the statistical sampling needed to reconstruct the average, global, tail and current sheet configurations. The major new accomplishments and results of this section are summarized here.

1) Pioneer Venus Orbiter observations within the Venus magnetotail routinely show a great deal of variability and, for example, the magnetic field data indicate that the spacecraft traverses between oppositely directed lobes many times in a single orbital pass. Some of this variability in apparent location within the magnetotail can undoubtedly be attributed to variations in the upstream solar wind flow direction. A large portion of the variability, however, must be attributed to another source. In this chapter the effects of draping a highly variable upstream magnetic configuration into the tail were proposed to account

for the variability. As the upstream cone angle of the IMF fluctuates, the relative amounts of magnetic flux within the two tail lobes at any given downtail distance are highly variable (see Figure 3.1). Therefore, the current sheet is forced to flap from side to side within the Venus magnetotail in an effort to maintain a pressure balance condition across the tail. This large scale flapping occurs on the rapid timescale of upstream IMF fluctuations and has confused the results of previous studies of the Venus magnetotail, which order the observations by their locations in spacecraft coordinates.

2) The 9423 one-minute averaged magnetic field measurements used in this statistical study were examined for evidence of reverse draping within the Venus magnetotail. Seventy-nine percent of the observed data were shown to be in the sense of a normal, draped magnetotail while twenty-one percent pointed in a reversed draped sense. The same procedure was repeated on 2701 one-minute data samples of purely magnetosheath field, and reverse draping was observed in sixteen percent of those data indicating that that fraction of apparent reverse draping was probably due to simple field rotations and normal field draping. It was therefore concluded that only a very small fraction of the data was indicative of actual reverse draping of the field ($\lesssim$5%) and that magnetic reconnection is probably not an important physical process in the Venus magnetotail.

3) A good statistical correlation was found between the magnetic field draping angle and the relative magnitude of the field,

compared to the field strength in the immediately adjacent portions of the magnetosheath. The cross tail current sheet was identified with the region of low relative field strength and with field vectors which point nearly across the tail (perpendicular to X) while the lobes were identified with regions of large relative field strength and field vectors which point nearly parallel and antiparallel to the tail (X) axis.

4) The Venus magnetotail configuration was statistically confirmed to consist of only two draped magnetic lobes separated by a single, field reversing current sheet. The average field draping angles in the outer regions of the lobes were determined to be -78.4^{o} and 73.4^{o} measured from the cross-flow direction toward the +X-direction. The 5^{o} difference between these two values is attributable to the effect of the average solar wind spiral angle draping into the tail.

5) Based on the large variability of the magnetic field data, a new statistical data analysis technique was developed. This technique uses uniform sampling supplied by the large fluctuations in the location of the cross tail current sheet to determine the relative frequency of various field draping angles within the tail. From these relative frequencies, and knowing the full width of the tail, a coordinate system was constructed which statistically determines the cross tail location (Y*) of each data point. In essence, these derived coordinates measure distances from the center of the cross tail current sheet rather than in spacecraft coordinates and thereby allow for a good

determination of the average magnetic topology of the Venus magnetotail for the first time.

6) In the new, derived coordinates a number of magnetic field properties as functions of cross tail location were determined for the first time. In particular, the tailward/sunward magnetic field, B_X, and the cross tail magnetic field, B_{Y*}, were both determined as functions of Y*. B_X was shown to vary smoothly from one lobe orientation to the other through the current sheet while B_{Y*} was found to be a double humped function, similar in appearance to cometary simulation results.

7) The extensive data set used in this study was also ordered according to downtail distance in order to find the average variation of B_{Y*} with X. The best linear fit to this variation was derived to be $B_{Y*}(X)$, averaged over Y*, = 11.53 + 0.68X, where the field is measured in nT and X is in R_V.

8) From the derived variations of B_{Y*} as a function of X, and B_X as a function of Y*, both components of the cross tail current density, J_Z, as a function Y* are calculated. J_Z was found to vary from $\sim$1.5 nA/m^2 in the center of the current sheet to $\sim$0.1 nA/m^2 at the edges of the current sheet.

9) Combining B_X, B_{Y*}, and J_Z, all as functions of Y*, gave the distribution of JxB forces across the tail. This electromagnetic force points tailward and inward toward the tail center at all locations across the tail as displayed in Figure 3.15.

10) From the derived, average magnetic field variations down the

tail, and the condition of continuity of the tangential electric field, the variation of the bulk downtail plasma velocity and plasma acceleration were then determined. The plasma velocity and acceleration vary from ~-250 km/sec and ~-1 km/sec^2 at -8 R_V to ~-470 km/sec and ~-7 km/sec^2 at -12 R_V, respectively.

11) This derived plasma acceleration profile, JxB force distribution, and the MHD momentum equation were then combined to determine the average current sheet and lobe plasma densities (~0.9 amu/cm^3 and ~0.07 amu/cm^3) and the approximate average ion temperature for the tail (~9 x 10^7 K for a purely O^+ tail). The typical plasma parameters derived in this chapter represent the only available data on the average plasma properties of the Venus magnetotail since none of the PVO plasma analyzers has a sufficient sensitivity and energy range to resolve the plasma properties. The average properties derived here were shown to be unobservable by the PVO plasma instrumentation, and therefore to be consistent with their general lack of observations.

12) The plasma betas calculated from the derived plasma properties are ~10 for the current sheet and ~0.1 for the lobes. These results are consistent with the expectation that varying quantities of magnetic flux at a given downtail distance will cause the cross tail current sheet to move within the tail and account for the large observed variability of the magnetic field data.

13) From the derived tailward plasma velocity and lobe and current sheet plasma densities, the mass flux down the Venus magnetotail

was calculated. This flux, integrated over the whole tail, is $\sim 1 \times 10^{26}$ amu/sec, and sets a reasonable bound on the neutral gas loss rate of the Venus atmosphere.

5.0.3 Comet Giacobini-Zinner

The Comet Giacobini-Zinner section (Chapter 4) combines the high resolution magnetic field and plasma electron data from the ICE tail traversal, for the first time. With the combined data and using the MHD equations, the details of the G-Z magnetotail are examined, and its configuration and properties are derived. The major new accomplishments and results of this chapter are summarized here.

1) Plasma electron moments from the immediately adjacent regions of solar wind, inbound and outbound along the ICE trajectory, were interpolated across the cometary encounter interval. This procedure yielded best upstream values for the plasma moments at the time of the ICE tail encounter (~11:00) of $n_{SW} = 6/cm^3$, $v_{SW} = 460$ km/sec, and $\sim -10.5^{o}$ solar wind flow angle (in the sense of normal aberration). These values set the upstream conditions for the tail crossing interval.

2) Using the interpolated flow angle and the inbound and outbound tail boundary crossings, the orientation of the magnetotail at the time of the ICE traversal was determined under a circular tail cross-section assumption. The orientation of the current sheet within the tail was then calculated using the additional assumption that the current sheet bisects the tail, and the

result was an angle of rotation of the current sheet within only 4^{o} of the 43^{o} angle derived from the field data. This agreement indicates that the two assumptions made about the tail configuration were quite good. The large difference between the inbound and outbound lobe crossing intervals was then simply explained in our derived tail/ICE crossing geometry by the slightly off-center trajectory of the spacecraft through the tail.

3) The total pressure on the external surface of the tail was derived from Bernoulli's equation and the upstream plasma conditions. This derived pressure is $\sim 1.2 \times 10^{9}$ N/m^{2} and supplied the boundary condition on the pressure balance within the tail.

4) The pressure balance condition within the tail was derived from the cross tail component of the MHD momentum equation and applied to the magnetic field and plasma electron measurements across the tail. This analysis gave the required ion pressure (and therefore temperature) profile for a balanced, steady state condition to exist across the tail. The derived ion pressure is much greater than the electron pressure and varies in an inverse sense from the magnetic field pressure.

5) The tailward/sunward component of the electromagnetic JxB force was calculated across the tail from smoothed magnetic field data, and the distribution was shown to consist of two distinct regions. In the current sheet the force is tailward, reaccelerating the most heavily mass loaded portions of the

field, while in the outer lobes the force is sunward, indicating that the lobe field is still being stretched and laminated into the draped tail configuration.

6) The number flux of particles passing the ICE location along any streamline was shown to be twice that of upstream at the average pick-up location on that streamline. This relation has important implications for the properties upstream, near to the comet nucleus. Beyond the average pick-up location along each streamline mass addition continues to slow the plasma flow.

7) The measured field and electron properties and derived ion properties and JxB force across the tail were combined with the axial component of the MHD momentum equation, the relation between the upstream and local number fluxes, the relation between pick-up velocity and temperature, and the MHD energy equation. This analysis yielded four equations in four unknowns which were solved with an iterative computer technique. Outputs from this analysis provided the first determinations of 1) the flow velocity profile at ICE, 2) the velocity profile upstream at the average pick-up location, 3) the ion temperature profile upstream at the average pick-up location, and 4) the density profile upstream at the average pick-up location.

8) The flow velocity at ICE was shown to be quite constant (~-20 to -30 km/sec) across the entire tail. This indicates that the ICE traversal distance was a special region for the spacecraft to have flown through, in that tail formation is occurring sunward

of this distance while tail dissipation must be occurring tailward from it.

9) The plasma properties in the average upstream region where ions are picked-up along each streamline are very different in regions upstream from the current sheet versus upstream from the lobes. Upstream from the current sheet our analysis finds a region of prime mass loading where the ion density rises to ~400 to 500/cm^3 while the plasma flow speed drops to only ~-12 km/sec. Upstream from the lobes, at the average pick-up locations, the density is low (~20/cm^3) and the flow speed high (~-75 km/sec).

10) The difference between the prime mass loading region upstream from the current sheet and the regions upstream from the lobes is further accentuated by the calculation of the source term in the MHD continuity equation from the divergence of the mass flux with downtail distance. This calculation yielded a region where the ion source rate is ~24 times that of the regions only ~1000 km to either side of it. Some possible causes of such a region were discussed and, in particular, the possibility of it being due to diffusion into the cometary ionosphere was examined. This model was also substantiated by the lack of an extended region of purely cold, unmagnetized ionospheric ions back at the ICE traversal distance.

11) The approximate acceleration rates of the lobe and current sheet plasmas between the average pick-up locations and ICE were used to examine the approximate scale length of the G-Z magnetotail.

The result of a few tens of thousands of kilometers is in good agreement with earth-based optical observations. In addition, the implications of the prime mass loading region and calculated acceleration rates were examined to attempt to describe why some comets have extensive visible ion tails and others do not.

12) The total number flux of particles traveling down the G-Z tail was calculated from the observed density and calculated velocity distributions. This integrated flux is $\sim 2.6 \times 10^{26}$ H_2O^+/sec, and represents only ~1% of the total mass loss rate of the comet. Consequently, the highly visible ion tail is relatively inconsequential in the global process of the solar wind's removal of material form the comet.

13) In order to find which locations are important in the more global mass pick-up and removal process, the number flux of particles for the entire ICE encounter was analyzed. The total derived ion loss rate for the entire encounter was found to be $\sim 2.5\text{-}5 \times 10^{28}$ H_2O^+/sec in excellent agreement with values derived by other, independent techniques. The dominant mass loading appears to occur in the large fluctuations of the transition region and outer magnetosheath.

5.1 General Discussion

Despite the very large differences between the three bodies which form the magnetotails studied in this dissertation, there are a number of common aspects which merit further discussion. This final section compares the general configurations, use of data, and

a number of specific results from the three chapters with the intent of elucidating their commonality. Each of the three main chapters in this dissertation was written in such a way that it can stand alone as a separate Journal of Geophysical Research paper. Consequently, each of the three also contains separate discussions of how the results fit into the broader picture of space plasma physics.

All three magnetotails examined in this dissertation consist of high beta current sheets which serve to separate two lower beta lobes of essentially oppositely directed magnetic fields. In all cases this general topology is traceable to the flow of the solar wind past the obstacle. The upstream solar wind (or magnetosheath flow if a shock is formed) can interact with the obstacle in a number of ways: magnetic interconnection between the IMF and planetary field (earth); viscous drag along the magnetopause (earth) or ionopause (Venus and comets) boundaries; mass loading of the flow (Venus and comets). In all of these cases, however, momentum and energy are transferred from the solar wind flow to the bodies with the effect of stretching out magnetic fields roughly parallel and anti-parallel to the solar wind flow vector.

This roughly antiparallel field configuration requires the formation of a self-consistent field reversing magnetotail current sheet where cross tail currents flow in accordance with Ampere's Law. Within the current sheets, plasma densities and betas are relatively large, and the field undergoes a rotation from one lobe's orientation to the other. Electromagnetic JxB forces in

magnetotails in general, and within their current sheets in particular, act to reduce the kinking of the field configuration either to a dipole (near earth) or straight IMF (distant earth, Venus, and comets) configuration, and thereby dissipate the tail. Only the continued input of energy and momentum from the solar wind flow can act to sustain the tail configurations as the long lived MHD structures which populate the solar system.

The earth, Venus, and G-Z data sets each provided quite different opportunities for examining the structure and properties of the three magnetotails and their field reversing current sheets. At Venus the data set contained $\sim 10^4$ one minute averaged magnetic field data samples, and allowed for the reconstruction of the average magnetic configuration of the Venus magnetotail. At earth and Comet G-Z, case studies and a single encounter traversal were used to examine the detailed tail structures on a crossing by crossing basis. In the earth study, magnetic field data from two co-orbiting satellites were combined to separate the spatial and temporal variations of the plasma sheet, while in the G-Z study, two plasma electron data sets were combined with the field data to derive the properties of the average pick-up location upstream. In all three studies, multiple measurements, either statistically with a single instrument or individually with multiple instruments, were employed to determine the magnetotail structures in far more detail than would be possible with any of the single data sets alone.

the importance of these various dynamic effects, and determine the approximate time independent configuration of the tails.

The magnetic field orientations in all three magnetotails were found to be strongly affected by the angle of the upstream IMF in the plane perpendicular to the solar wind (clock angle). Field lines in the terrestrial current sheet crossings studied were inclined with respect to the nominal current sheet orientations, and were found to generally point in the sense of the upstream IMF. Evidently the partial magnetic interconnection between the earth's field and the IMF allows the orientation of the upstream configuration to affect the internal magnetic field orientation (probably by setting up convection cells in the lobes). At Venus and Comet Giacobini-Zinner, the situation is even much more clear cut. Draping of the upstream field forms the field reversing current sheets, and, consequently, current sheet axes at these bodies are necessarily oriented normal to the IMF directions.

Current sheets in the three magnetotails studied here were all found to be thick compared to the asymptotic thermal ion gyroradii for those tails. The typical thicknesses range from ~5 O^+ gyroradii at Venus to ~19 H_2O^+ gyroradii at G-Z and ~30-100 proton gyroradii for the central terrestrial current sheet. All of these values are larger than might be expected from the simple minded picture of ions gyrating back and forth across a Harris type neutral sheet. Other physical processes such as gradient drifts of the particles, and the effects of a normal component of the field are undoubtedly also important in these current sheets.

Normal field components are observed at all three current sheets. These components range from ~4 nT at Venus to ~10 nT and G-Z and ~10-20 nT for the current sheet crossings studied at the earth. Compared to the typical lobe field values in the tails, these normal components are ~1/3, ~1/4, and ~1/2, respectively. Such strong normal components are indicative of tail configurations which are relatively stable locally against reconnection.

In the case of G-Z, very few of the high resolution field vectors (1/3 second) observed along the ICE trajectory were pointed in the opposite sense to the average field direction, while at Venus, only ~5% of the field vectors were pointed in such a manner. These results indicate that at least at the time and location that ICE crossed the G-Z current sheet, and generally in the -8 to-12 R_V range of the Venus tail, reconnection is not a dominant physical process. Beyond the ICE intercept distance at G-Z and the range of tail coverage at Venus, the two draped field configurations in these magnetotails should be restraightening, and conditions for reconnection should be becoming even poorer. In contrast, while the near earth regions of the terrestrial tail are not conducive to reconnection at the geomagnetically quiet times studied here, a more tail-like configuration (with decreasing normal component) occurs with distance down the tail. At some distance, reconnection must occur, on average, in order to maintain a steady state interconnection between the earth's field and the IMF which is constantly being convected past. This deep tail reconnection may have important implications for energization of current sheet

particles at earth, while at induced magnetotails ions are energized primarily by the pick-up process.

Peak cross tail current densities determined for the three current sheets vary over a range of about 100. The typical earth, Venus, and G-Z peak cross tail current densities are ~5-50 nA/m^2, ~1.5 nA/m^2, and ~100 nA/m^2, respectively. At Venus and G-Z these cross tail currents give rise to peak tailward JxB forces of ~$1x10^{-17}$ N/m^3 and ~$1x10^{-15}$ N/m^3. Not surprisingly, the derived mass flux, or mass loss rate down the G-Z tail is ~50 times that at Venus (~$5x10^{27}$ amu/sec versus ~$1x10^{26}$ amu/sec), indicating that a much more mass loaded plasma exists in the G-Z tail, consistent with the much larger JxB force. Even though the G-Z magnetotail conducts away only ~1% of the total cometary efflux, the near nucleus mass loading which accounts for the tail is still far more effective than the mass loading of the gravitationally bound Venus atmosphere and ionosphere. The near-nucleus mass loading environment at G-Z, while not gravitationally bound, exhibits a region of concentrated mass loading which in some ways mimics the Venus obstacle. This region evidently accounts for the narrow, well-defined nature of the tail, and greatly enhances the similarities between the solar wind interactions with Venus and Comet Giacobini-Zinner.

Field reversing current sheets comprise a fascinating class of space plasma physics structures within the solar system, and quite possibly in many astrophysical applications. In the magnetotails of the earth, Venus, and Comet Giacobini-Zinner, these structures present numerous interesting properties which have been examined in

detail in the work of this dissertation. Knowledge gained from these examinations paves the way to a lifetime of research to better understnad the vast and still little known realms of current sheets and other plasma structures throughout the solar system and beyond.

The dissertation of David John McComas is approved.

Paul J. Coleman

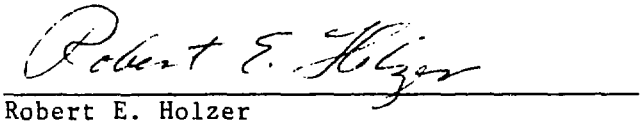

Robert E. Holzer

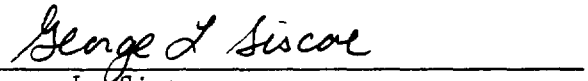

George L. Siscoe

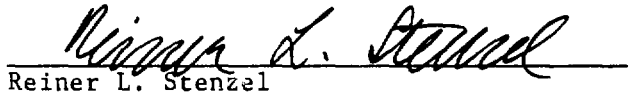

Reiner L. Stenzel

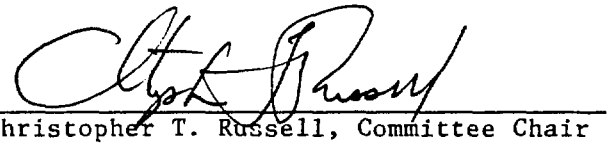

Christopher T. Russell, Committee Chair

University of California, Los Angeles

1986

ACKNOWLEDGMENTS

The American Geophysical Union is gratefully acknowledged for granting permission to reproduce material in Chapters 2 and 3. ("The Near Earth Cross Tail Current Sheet: Detailed ISEE-1 and -2 Case Studies," McComas, D. J., C. T. Russell, R. C. Elphic, S. J. Bame; J. Geophys. Res., 91, 4287-4301, 1986, copyright by the American Geophysical Union; and "The Average Magnetic Field Draping and Consistent Plasma Properties of the Venus Magnetotail," McComas, D. J., H. E. Spence, C. T. Russell, M. A. Saunders; J. Geophys. Res., 91, 7939-7953, 1986, copyright by the American Geophysical Union.) I am sincerely thankful to my co-authors on these papers, and to J. T. Gosling, S. J. Bame, J. A. Slavin, E. J. Smith, and J.-L. Steinberg, co-authors of "The Giacobini-Zinner Magnetotail: Tail Configuration and Current Sheet," submitted for publication. To C. T. Russell, W. I. Newman, and G. L. Siscoe, who provided invaluable graduate instruction and guidance on all aspects of this dissertation, and to my wife, Richelle Wolff McComas, who provided tireless clerical and editorial support, I wish to give special thanks. Finally, I gratefully acknowledge Los Alamos National Laboratory, operated under the auspices of the United States Department of Energy, and my supervisors, D. N. Baker and W. D. Evans, and P.J. Coleman, head of the Los Alamos Branch of the Institute for Geophysics and Planetary Physics, for providing financial and administrative support throughout my graduate education.

References

Alexander, C. J. and C. T. Russell, Solar cycle dependence of the location of the Venus bow shock, Geophys. Res. Lett., 12, 369, 1985.

Alfvén, H., On the theory of comet tails, Tellus, 9, 92, 1957.

Baker, D. N., E. W. Hones, Jr., J. B. Payne, and W. C. Feldman, A high-time resolution study of interplanetary parameter correlations with AE, Geophys. Res. Lett., 8, 179, 1981.

Bame, S. J., J. R. Asbridge, H. E. Felthauser, R. A. Olson, I. B. Strong, Electrons in the plasma sheet of the Earth's magnetic tail, Phys. Rev. Letters, 16, 138, 1966.

Bame, S. J., J. R. Asbridge, H. E. Felthauser, E. W. Hones, Jr., I. B. Strong, Characteristics of the plasma sheet in the Earth's magnetotail, J. Geophys. Res., 72, 113, 1967.

Bame, S. J., J. R. Asbridge, H. E. Felthauser, J. P. Glore, H. L. Hawk, and J. Chavez, ISEE-C solar wind plasma experiment, IEEE Trans. Geosci. Electr., GE-16, 160, 1978.

Bame, S. J., R. C. Anderson, J. R. Asbridge, D. N. Baker, W. C. Feldman, J. T. Gosling, E. W. Hones, Jr., D. J. McComas, and R. D. Zwickl, Plasma regimes in the deep geomagnetic tail: ISEE-3, Geophys. Res. Lett., 10, 912, 1983.

Bame, S. J., R. C. Anderson, J. R. Asbridge, D. N. Baker, W. C. Feldman, S. A. Fuselier, J. T. Gosling, D.J. McComas, M. F. Thomsen, D. T. Young, and R. D. Zwickl, Comet Giacobini-Zinner: A plasma description, Science, 232, 356, 1986.

Bargatze, L. F., D. N. Baker, R. L. McPherron, and E. W. Hones, Jr., Magnetospheric impulse response for many levels of geomagnetic activity, J. Geophys. Res., 90, 6387, 1985.

Bieber, J. W. and E. C. Stone, Energetic electron bursts in the magnetopause electron layer and in interplanetary space, in Magnetospheric Boundary Layers edited by B. Battrick pp. 131-135, ESA, Paris, 1979.

Biermann, L., Kometenschweife und solare korpuskularstrahlung, Z. Astrophys, 29, 274, 1951.

Boice, D. C., W. F. Huebuer, and J. J. Keady, A model of Comet P/Giacobini-Zinner, Geophys. Res. Lett., 13, 381, 1986.

Brandt, J. C., Observations and dynamics of plasma tails, in Comets, edited by L. L. Wilkening, University of Arizona Press, Tucson, 1982.

Cloutier, P. A., R. E. Daniell, and D. M. Butler, Atmospheric ion wakes of Venus and Mars in the solar wind, Planet. Space Sci., 22, 967-990, 1974.

Cloutier, P. A., Solar wind interaction with planetary ionospheres, in Solar Wind Interactions with Planets Mercury, Venus and Mars, edited by N. F. Ness, NASA SP-397, pp. 111-119, 1976.

Cowley, S. W. H., The adiabatic flow model of a neutral sheet, Cosmic Electrodynamics, 2, 91, 1971.

Cowley, S. W. H., A self-consistent model of a simple magnetic neutral sheet system surrounded by a cold, collisionless plasma, Cosmic Electrodynamics, 3, 449, 1972.

Daly, P. W., T. R. Sanderson, K. -P. Wenzel, S. W. H. Cowley, R. J. Hynds, and E. J. Smith, Gyroradius effects on the energetic ions in the tail lobes of Comet P/Giacobini-Zinner, Geophys. Res. Lett., 13, 419, 1986.

Dolginov, Sh. Sh., L. N. Zhuzgov, V. A. Sharova, and V. B. Buzin, Magnetic field and magnetosphere of the planet Venus, Cosmic Res., 16, 657, 1978.

Ershkovich, A. I., and D. A. Mendis, On the penetration of the solar wind into the cometary ionosphere, The Astrophys. J., 269, 743, 1983.

Fairfield, D. H., On the average configuration of the geomagnetic tail, J. Geophys. Res., 84, 1950, 1979.

Fairfield, D. H., A statistical determination of the shape and position of the geomagnetic neutral sheet, J. Geophys. Res., 85, 775, 1980.

Fairfield, D. H., R. P. Lepping, E. W. Hones, Jr., S. J. Bame, and J. R. Asbridge, Simultaneous measurements of magnetotail dynamics by IMP spacecraft, J. Geophys. Res., 86, 1396, 1981.

Fedder, J. A., J. G. Lyon, and J. L. Giuliani, Jr., Numerical simulations of comets: predictions for Comet Giacobini-Zinner, EOS, 67, 17, 1986.

Forbes, T. G., E. W. Hones, Jr., S. J. Bame, J. R. Asbridge, G. Paschmann, N. Sckopke, and C. T. Russell, Substorm-related plasma sheet motions as determined from differential timing of plasma changes at the ISEE satellites, J. Geophys. Res., 86, 3459, 1981.

Foster, J. L., D. H. Fairfield, K. W. Ogilvie, and T. J. Rosenberg, Relationship of interplanetary parameters and occurrence of magnetospheric substorms, J. Geophys. Res., 76, 6967, 1971.

Frandsen, A. M. A., B. V. Connor, J. van Amersfoort, and E. J. Smith, The ISEE-C vector helium magnetometer, IEEE Trans. Geosci. Electr., GE-16, 195, 1978.

Fuselier, S. A., W. C. Feldman, S. J. Bame, E.J. Smith,and F. L.Scarf, Heat flux observations and the location of the transition region boundary of Giacobini-Zinner, Geophys. Res. Lett., 13, 247, 1986.

Gosling, J. T., J. R. Asbridge, S. J.Bame, M. F. Thomsen, and R. D. Zwickl, Large amplitude, low frequency plasma fluctuations at Comet Giacobini-Zinner, Geophys. Res. Lett., 13, 267, 1986.

Hones, E. W. Jr., Transient phenomena in the magnetotail and their relation to substorms, Space Science Reviews, 23 393, 1979.

Hones, E. W., Jr., J. Birn, S. J. Bame, G. Paschmann, and C. T. Russell, On the three-dimensional magnetic structure of the plasmoid created in the magnetotail at substorm onset, Geophys. Res. Lett., 9, 203, 1982.

Hones, E. W., Jr., J. Birn, D. N. Baker, S. J. Bame, W. C. Feldman, D. J. McComas, and R. D. Zwickl, Detailed examination of a plasmoid in the distant magnetotail with ISEE-3 Geophys. Res. Lett., 11, 1046, 1984.

Huebner, W. F., Cometary coma, G. H. F. Dickerson et al. editors, Molecular Astrophysics, D. Reidel Pub. Co., 311, 1985.

Intriligator, D. S., J. H. Wolfe, and J. D. Mihalov, The Pioneer Venus Orbiter plasma analyzer experiment, IEEE Trans. on Geoscience and Remote Sensing, GE-19, 1, 39, 1980.

Intriligator, D. S., and F. L. Scarf, Wave-particle interactions in the Venus wake and tail, J. Geophys. Res., 89, 47, 1984.

Ip, W. H., and W. I. Axford, Theories of physical processes in the cometary comae and ion tails, in Comets, edited by L. L. Wilkening, University of Arizona Pres. Tucson, 1982.

Jones, D. E., E. J. Smith, J. A. Slavin, B. T. Tsurutani, G. L. Siscoe, and D. A. Mendis, The bow wave of Comet Giacobini-Zinner: ICE magnetic field observations, Geophys. Res. Lett., 13, 243, 1986.

Knoll, R., G. Epstein, S. Hoang, G. Huntzinger, J. L. Steinberg, J. Fainberg, F. Grena, S. R. Mosier, and R. G. Stone, The

3-dimensional radio mapping experiment (SBH) on ISEE-C, IEEE Trans. Geosci. Electr., GE-16, 199, 1978.

Luhmann, J. G., C. T. Russell, J. R. Spreiter and S. S. Stahara, Evidence for mass-loading of the Venus magnetosheath Adv. Space Res., 5(4), 307, 1985.

Lui, A. T. Y., C. I. Meng, and S. I. Akasofu, Wavy nature of the magnetotail neutral sheet, Geophys. Res. Lett., 5, 279, 1978.

Lui, A. T. Y., Characteristics of the cross-tail current in the Earth's magnetotail, Magnetospheric Currents, Geophysical Monograph, Vol. 28, 158, 1983.

McComas, D. J. and C. T. Russell, The near Earth current sheet: ISEE-1 and -2 case studies, Proc. Conf. Achievements of the IMS, ESA, SP-217, 205, 1984.

McComas, D.J., H. E. Spence, C. T. Russell, and M. A. Saunders, The average magnetic field draping and consistent plasma properties of the Venus magnetotail, J. Geophys. Res., 91, 7939, 1986a.

McComas, D. J., H. E. Spence,and C. T. Russell, The average configuration of the induced Venus magnetotail, accepted to Chapman Conference Proceedings on Magnetotail Physics, 1986b.

McPherron, R. L., C. T. Russell, and M. P. Aubry, Satellite studies of magnetospheric substorms on August 15, 1969, 9. Phenomenological model for substorms, J. Geophys. Res., 78, 3131, 1973.

Mendis, D. A., and H. L. F. Houpis, The cometary atmosphere and its interaction with the solar wind, Rev. Geophys., 20, 885, 1982.

Mendis, D. A., E. J. Smith, B. T. Tsurutani, J. A. Slavin, D. E. Jones, and G. L. Siscoe, Comet-solar wind interaction: Dynamical length scales and models, Geophys. Res. Lett., 13, 239, 1986.

Meyer-Vernet, N., P. Couturier, S. Hoang, C. Perche, J. L. Steinberg, J. Fainberg, and C. Meetre, Plasma diagnosis from thermal noise and limits on dust flux or mass in comet P/Giacobini-Zinner, Science, 232, 370, 1986a.

Meyer-Vernet, N., P. Couturier, S. Hoang, C. Perche, and J. L. Steinberg, Physical parameters for hot and cold electron populations in Comet Giacobini-Zinner with the ICE radio experiment, Geophys. Res. Lett., 13, 279, 1986b.

Meyer-Vernet, N., M. A. Strauss, J. L. Steinberg, H. Spinrad, and P. J. McCarthy, Comet P/Giacobini-Zinner electron and H_2O^+

column densities from ICE and ground-based observations, submitted to Astronomical Journal, 1986c.

Mihalov, J. D. and A. Barnes, Evidence for the acceleration of ionospheric O^+ in the magnetosheath of Venus, Geophys. Res. Lett., 8, 1277, 1981.

Mihalov, J. D., and A. Barnes, The distant interplanetary wake of Venus: plasma observations of Pioneer Venus, J. Geophys. Res., 87, 9045, 1982.

Moses, J. J., N. U. Crooker, D. J. Gorney, and G. L. Siscoe, High-latitude convection on open and closed field lines for large IMF B_y, submitted to the Journal of Geophyical Research, 1985.

Ogilvie, K. W., M. A. Coplan, P. Bochsler, and J. Geiss, Ion composition results during the International Cometary Explorer encounter with Giacobini-Zinner, Science, 232, 374, 1986.

Russell, C. T., The solar wind and magnetospheric dynamics, correlated interplanetary and magnetospheric observations, edited by D. E. Page, 3, D. Riedel, Hingham, Mass., 1974.

Russell, C. T., The magnetosphere of Venus: evidence for a boundary layer and a magnetotail, Geophys. Res. Lett., 3, 589, 1976.

Russell, C. T., R. C. Elphic, J. G. Luhmann, and J. A. Slavin, On the search for an intrinsic magnetic field at Venus, Proc. Lunar Planet Conf. 11th, 1896, 1980a.

Russell, C. T., R. C. Snare, J. D. Means, and R. C. Elphic, Pioneer Venus Orbiter Fluxgate Magnetometer, IEEE Trans. GE-18, 32, 1980b.

Russell, C. T., J. G. Luhmann, R. C. Elphic, and F. L. Scarf, The distant bow shock and magnetotail of Venus: magnetic field and plasma wave observations, Geophys. Res. Lett., 8, 843, 1981.

Russell, C. T., M. A. Saunders, and J. G. Luhmann, Mass-loading and the formation of the Venus tail, Adv. Space Res., 5, 177-184, 1985.

Saunders, M. A., and C. T. Russell, Average dimension and magnetic structure of the distant Venus magnetotail, in press J. Geophys. Res., 1986.

Saunders, M. A., C. T. Russell, J. G. Luhmann, Interactions with planetary ionospheres and atmospheres: a review, submitted to Proc. of Comparative Study of Magnetospheric Systems, 1985.

Schmidt, H. U. and R. Wegmann, MHD-calculations for cometary plasmas, Computer Physics Communications, 19, 309, 1980.

Schmidt, H. U., and R. Wegmann, Plasma flow and magnetic fields in comets, in Comets, (ed. L. L. Wilkening), University of Arizona Press; Tucson, Arizona; p. 538, 1982.

Sibeck, D. G., G. L. Siscoe, J. A. Slavin, E. J. Smith, B. T. Tsurutani, and R. P. Lepping, The distant magnetotail's response to a strong interplanetary magnetic field by: twisting, flattening, and field line bending, J. Geophys. Res., 90, 4011, 1985.

Siscoe, G. L., Solar system magnetohydrodynamics, Proceedings of the 1982 Boston College Theory Institute in Solar-Terrestrial Physics, R. L. Carovillano and J. M. Forbes, Editors, D. Reidel Pub. Co., Dordrecht-Holland, 1982.

Siscoe, G. L., J. A. Slavin, E. J. Smith, B. T. Tsurutani, D. E. Jones, and D. A. Mendis, Statics and dynamics of Giacobini-Zinner magnetic tail, Geophys. Res. Lett., 13, 287, 1986.

Slavin, J. A., E. J. Smith, B. T. Tsurutani, G. L. Siscoe, D. E. Jones, and D. A. Mendis, Giacobini-Zinner magnetotail: ICE magnetic field observations, Geophys. Res. Lett., 13, 283, 1986a.

Slavin, J. A., B. A. Goldberg, E. J. Smith, D. J. McComas, S. J. Bame, M A. Strauss, and H. Spinrad, The structure of a cometary type I tail: ground-based and ICE observations of P/Giacobini-Zinner, submitted to Geophys. Res. Lett., 1986b.

Slavin, J. A., E. J. Smith, D. S. Intriligator, A comparative study of distant magnetotail structure at Venus and Earth, Geophys. Res. Lett., 11, 1074, 1984.

Slavin, J. A., D. S. Intriligator, and E. J. Smith, Initial PVO Observations of Magnetic Field Draping at Venus Due to Mass Loading: Implications for Magnetotail Formation at Venus and Comets, Submitted to J. Geophys. Res., 1985.

Smith, E. J., B. T. Tsurutani, J. A. Slavin, D. E. Jones, G. L. Siscoe, and D. A. Mendis, ICE encounter with Giacobini-Zinner: Magnetic field observations, Science, 232, 382, 1986.

Speiser, T. W., Particle trajectories in model current sheets 1. Analytic solutions, J. Geophys. Res., 70, 4219, 1965.

Spreiter, J. R. and S. S. Stahara, Solar wind flow past Venus: Theory and comparisons, J. Geophys. Res., 85, 7715, 1980.

Strauss, M. A., P. J. McCarthy, and H. Spinrad, Optical spectrophotometry of Comet P/Giacobini-Zinner and emission profiles of H_2O^+, Geophys. Res. Lett., 13, 389, 1986.

Tsurutani, B. T., and E. J. Smith, Strong hydromagnetic turbulence associated with Comet Giacobini-Zinner, Geophys. Res. Lett., 13, 259, 1986a.

Tsurutani, B. T., and E. J. Smith, Hydromagnetic waves and instabilities associated with cometary ion pick-up: ICE observations, Geophys. Res. Lett., 13, 263, 1986b.

Voigt, G. -H. and R. Hilmer, The influence of the IMF B_Y component on the earth's magneto-hydrostatic magnetotail, Accepted to Chapman Conference Proceedings on Magnetotail Physics, 1986.

Zwickl, R. D., D. N. Baker, S. J. Bame, W. C. Feldman, S. A. Fuselier, W. F. Huebner, D. J. McComas, and D. T. Young, Three component plasma electron distributions in the intermediate ionized coma of Comet Giacobini-Zinner, Geophys. Res. Lett., 13, 401, 1986.

*U.S. GOVERNMENT PRINTING OFFICE: 1986-0-676-034/40040